

Dynamic Light Scattering and Rheological
Studies of some Micellar Copolymer Solutions,
Biopolymer Gels and Concentrated Colloidal
Suspensions

BY

RAJIB BASAK

A THESIS SUBMITTED TO THE JAWAHARLAL NEHRU UNIVERSITY

FOR THE DEGREE OF DOCTOR OF PHILOSOPHY

DEPARTMENT OF SOFT CONDENSED MATTER

RAMAN RESEARCH INSTITUTE

BANGALORE 560 080

JUNE 2014



© Rajib Basak, 2014.

Typeset in $\text{\LaTeX}2_{\epsilon}$.

Certificate:

This is to certify that the thesis entitled “**Dynamic Light Scattering and Rheological Studies of some Micellar Copolymer Solutions, Biopolymer Gels and Concentrated Colloidal Suspensions**” submitted by Rajib Basak for the award of the degree of Doctor of Philosophy of Jawaharlal Nehru University is his original work. This has not been published or submitted to any other University for any other Degree or Diploma.

Prof. Ravi Subrahmanyam
(Director)
Raman Research Institute
Bangalore 560 080
India

Dr. Ranjini Bandyopadhyay
(Thesis Supervisor)

Declaration:

I hereby declare that the work reported in this thesis is entirely original. This thesis is composed independently by me at Raman Research Institute under the supervision of Dr. Ranjini Bandyopadhyay. I further declare that the subject matter presented in this thesis has not previously formed the basis for the award of any degree, diploma, membership, associateship, fellowship or any other similar title of any university or institution.

Dr. Ranjini Bandyopadhyay

Rajib Basak

Soft Condensed Matter Group
Raman Research Institute
Bangalore 560 080
India

Acknowledgements

I am grateful to my thesis supervisor Dr. Ranjini Bandyopadhyay for her encouragement, guidance and support to complete my thesis work. I am thankful to her for giving me the independence to work which helped me to become a better researcher. I would like to thank Prof. V. A. Raghunathan, Prof. Pramod Pullarkat and other faculties in the Soft Condensed Matter Group for their helpful discussions, encouragements and advices.

I would like to convey my sincere gratitude to my seniors, Dr. Antara Pal and Dr. Md. Arif Kamal for their help with the X-ray experiments and constant encouragement. I would like to thank Prof. Reji Philip and Dr. Priya Rose for caring out the experiments in their laboratory and offering a helping hand whenever needed.

My sincerest thanks to my lab mates, Mr. Debasish Saha, Mr. Samim Ali, Ms. Nabaneeta Mukhopadhyay and Dr. Harsha Mohan Paroor for helping me in daily basis and giving me company in ups and downs of my life in last few years. I wish them best of luck with their future. I express my gratitude to visiting project student to our laboratory, Mr. Rajsekhar Das for his help with the calculation of Lyapunov exponents with TISEAN package. I am deeply indebted to Mr. Tridib Ray for his help with the experiments and invaluable advices at various stages of my thesis work. I express my gratitude to Mrs. K.

N. Vasudha for her help with the Differential Scanning Calorimetry measurements. I am thankful to Mr. A. Dhasan, Mr. Duraichelvan for their help and guidance with the Cryo-SEM experiments. I am deeply grateful to Prof. V. Lakshminarayanan for giving me opportunity to do Cryo-SEM at the first place.

I am thankful to every student at RRI for their friendship, encouraging discussions in various topics, giving me company in various events and adding fun to my life at RRI. My special thanks to my football team mates for helping me to rejuvenate after the days ordeal and giving me many unforgettable pleasant memories through fun activities. In particular, I would like to thank Arif, Arijit, Anirban, Tridib, Arnab, Anjan, Prasad, Debasish, Samim, Shafi, Rahul, Raj, Santanu, Deepak, Varun and many more for giving me company in these fun activities. I am thankful to my friends at RMV hostel for being amazing companions during my stay and doing many fun activities like watching movie, pure gossip, celebrating my birthday etc. Additional thanks to Arnab, Anjan and Debasish for putting up with my cooking in the initial days and helping me to be an excellent cook.

I am thankful to the RRI Workshop for their invaluable contribution in fabricating essential parts for the experimental set-up. A very special note of thanks is to our group secretary Mr. Radhakrishna for his assistance with purchase, travel claim and many more things. I would like to express my gratitude to Raja and Murali for extending their helpful hand in countless occasions. I would like to thank Mr. Y. M. Patil, Dr. Meera B. M. and all the staff members of the library for their assistance. I am thankful to Mr. Ramamurthy and all other staffs in the purchase and account departments for their help to procure things for experiments at proper time. I would like to thank the computer section for their assistance, especially Mr. Krishnamurthy for his help with the installation of DLS autocorrelator card, Mr. Sridhar B. and Mr. Jacob Rajan for sorting out countless computer and internet connection issues. I acknowledge sincerely

the help I received from the director, Prof. Ravi Subrahmanyam and administrative officer Mr. Krishnama Raju. I express my gratitude to Mrs. Shailaga, Mrs. Marisa, Mrs. Radha and all other staff members of administration for their help with various academic and administrative issues. I am grateful to all the canteen staff members, hostel staff members, and everyone at RRI for their cooperation.

Lastly, I express my deepest gratitude and love for my parents, my brother and other family members for their constant support. My special thanks goes to my brother, Probal for sharing major part of the responsibilities and letting me focus on my thesis work.

Synopsis

Soft matter, characterized by complexity and flexibility, refers to the broad range of condensed matter systems. Due to weak interactions between the constituents of soft materials, they show viscoelastic behavior. The different properties of these soft matter systems are very sensitive to the concentration, temperature, presence of additives and other physical properties. In this thesis, we perform dynamic light scattering and rheological experiments to investigate the structure, dynamics and the mechanical properties of some aqueous soft matter systems including micellar copolymer solutions, biopolymer gels and concentrated colloidal suspensions.

The background material necessary to understand the thesis work is described in Chapter 1. The chapter starts with a brief discussion of some soft matter systems including amphiphilic molecules, colloidal suspensions and biopolymer hydrogels. Intermolecular interactions between the constituents of soft matter are next described. This is followed by the description of different materials that are used in this thesis work. The chapter concludes with a brief introduction of the techniques of rheometry, dynamic light scattering and nonlinear time-series analysis that have been employed in this thesis work.

The detailed descriptions of the experimental methods used in this thesis are given in Chapter 2. This section describes, in detail, the rheological and dynamic light scattering techniques used in our studies. Other experimental techniques such as cryogenic scanning electron microscopy (Cryo-SEM) imaging, fluorescence spectroscopy and small angle X-ray scattering (SAXS), which have been used to investigate the different systems probed here, are also described in this chapter.

Chapter 3 describes the jamming behavior of Pluronic F127 micelles and the jamming-unjamming transition of these micellar systems in the presence of the anionic surfactant SDS. Pluronic F127 is a triblock PEO-PPO-PEO copolymer which exhibits amphiphilic nature at high temperatures. Above a critical concentration and temperature, Pluronic molecules self-aggregate to form spherical micelles in aqueous solution with a hydrophobic PPO core, surrounded by a hydrophilic PEO corona. This micellization process is very sensitive to the presence of additives and temperature. Increasing the concentration of triblock copolymers results in a sharp increase in the magnitude of the complex moduli characterising the samples. This is understood in terms of the changes in the aggregation and packing behaviours of the copolymers and the constraints imposed upon their dynamics due to increased close packing. The addition of suitable quantities of an anionic surfactant to a strongly elastic copolymer solution results in a decrease in the complex moduli of the samples by several decades. It is argued that the shape anisotropy and size polydispersity of the micelles comprising mixtures cause dramatic changes in the packing behaviour, resulting in sample unjamming and the observed decrease in complex moduli. Finally, a phase diagram is constructed in the temperature-surfactant concentration plane to summarise the jamming-unjamming behaviour of aggregates constituting triblock copolymer-anionic surfactant mixtures.

Pluronic micelles have emerged as a potential agent for targeted drug delivery. Chapter 4 discusses the encapsulation of different drug molecules (Ibuprofen, Aspirin, Erythromycin) in the Pluronic micelles and their dependence on temperature, pH and drug hydrophobicity. The shapes and the size distributions of the micelles in dilute, aqueous solutions, with and without drugs, are ascertained using cryo- Scanning Electron Microscopy and Dynamic Light Scattering experiments, respectively. Uptake of drugs above a threshold concentration is seen to reduce the critical micellization temperature of the solution. The mean hydrodynamic radii and polydispersities are found to increase with decrease in temperature and in the presence of drug molecules. The hydration of the micellar core at lower temperatures is verified using fluorescence measurements. Increasing solution pH leads to the ionization of the drugs incorporated in the micellar cores. This leads to rupture of the micelles and release of the drugs into the solution at the higher solution pH.

Chapter 5 describes the formation and rupture of Ca^{2+} induced pectin biopolymer pectin gels. When calcium salts are added to an aqueous solution of polysaccharide pectin, ionic cross-links form between pectin chains, giving rise to a gel network in dilute solution. Pectin is an important ingredient of plant cell walls, where ion-mediated pectin gels are known to contribute to the cell wall rigidity. Pectin is also often used in gel form in the areas of food science and pharmaceuticals. In this work, dynamic light scattering (DLS) is employed to study the microscopic dynamics of the fractal aggregates (flocs) that constitute the gels, while rheological measurements are performed to study the process of gel rupture. As calcium salt concentration is increased, DLS experiments reveal that the polydispersities of the flocs increase simultaneously with the characteristic relaxation times of the gel network. Above a critical salt concentration, the flocs become interlinked to form a reaction-limited fractal

gel network. Rheological studies demonstrate that the limits of the linear rheological response and the critical stresses required to rupture these networks both decrease with increase in salt concentration. These features indicate that the ion-mediated pectin gels studied here lie in a ‘strong link’ regime that is characterised by inter-floc links that are stronger than intra-floc links. A scaling analysis of the experimental data presented here demonstrates that the elasticities of the individual fractal flocs exhibit power-law dependences on the added salt concentration. We conclude that when pectin and salt concentrations are both increased appropriately, the number of fractal flocs of pectin increases simultaneously with the density of crosslinks, giving rise to very large values of the bulk elastic modulus.

Cornstarch suspensions are known for their complex mechanical response. Chapter 6 presents rheological measurements on cornstarch suspensions. The flow curve measurements on cornstarch suspensions show a shear thinning region, followed by a shear thickening and a shear banding region with increasing shear rate. The extents of the different regions of cornstarch suspensions depend upon the concentration and sample volume. Small angle light scattering experiments, which are simultaneously done with rheology, show huge intensity fluctuations in the shear banding region. Non linear time series analysis of the stress fluctuation data acquired from cornstarch samples lying in the shear banding region indicates the presence of rheological chaos.

Chapter 7 summarizes the main results reported in this thesis and briefly discusses the scope for future works.

Publication List

Publications from this thesis:

1. Experimental studies of the jamming behaviour of triblock copolymer solutions and triblock copolymer-anionic surfactant mixtures

Rajib Basak, N. Mukhopadhyay, and R. Bandyopadhyay
Eur. Phys. J. E , **34**, 103 (2011)

2. The encapsulation of hydrophobic drugs in Pluronic F127 micelles: the effects of drug hydrophobicity, solution temperature and pH

Rajib Basak and R. Bandyopadhyay
Langmuir, **29** (13), 4350 (2013)

3. Formation and Breakage of Ca^{2+} Induced Pectin Biopolymer Gels.

Rajib Basak and R. Bandyopadhyay
(Submitted to Soft Matter)

Contents

Acknowledgements	v
Synopsis	viii
Publication List	xii
1 Introduction	5
1.1 Soft matter	5
1.2 Examples of soft matter systems	6
1.2.1 Amphiphilic molecules	6
1.2.2 Colloidal suspensions	7
1.2.3 Hydrogels	8
1.3 Intermolecular interactions in soft matter	9
1.3.1 van der Waals interaction	9
1.3.2 Electric double layer interaction	10
1.3.3 Hydrophobic interaction	11
1.4 Some examples of phase transitions in soft matter	12
1.4.1 Self assembly of amphiphilic molecules:	12

1.4.2	Jamming transition	13
1.5	Materials studied	15
1.5.1	Pluronic F127	15
1.5.2	Pectin gels	16
1.5.3	Cornstarch suspensions	17
1.6	Experimental studies	18
1.6.1	Rheology	19
1.6.2	Dynamic Light Scattering	24
1.7	Chaotic dynamics in dissipative systems:	27
1.8	Thesis Organization	29
References		31
2 Experimental Techniques and Data Analysis		39
2.1	Introduction:	39
2.2	Experimental techniques:	40
2.2.1	Rheological measurements:	40
2.2.2	Dynamic light scattering:	47
2.2.3	Cryo-SEM (scanning electron microscopy) measurements:	52
2.2.4	Fluorescence measurements.	54
2.2.5	Small angle X-ray scattering (SAXS).	56
2.3	Data Analysis:	57
2.3.1	Analysis of observed chaotic data:	57
References		63
3 Jamming Behavior of Triblock Copolymer Solutions and Triblock Copolymer-Anionic Surfactant Mixtures		65
3.1	Introduction	65
3.2	Sample preparation	68

3.3 Results	68
3.4 Conclusions	83
References	85
4 Encapsulation of drugs in Pluronic F127 Micelles: The Effects of Drug Hydrophobicity, Solution Temperature and pH	89
4.1 Introduction	89
4.2 Sample preparation	92
4.3 Results and Discussion	93
4.4 Conclusion	108
References	110
5 Formation and Rupture of Ca²⁺ Induced Pectin Biopolymer Gels	113
5.1 Introduction	113
5.2 Sample preparation	115
5.3 Results and Discussions	116
5.3.1 Gel Formation:	116
5.3.2 Gel Rupture:	124
5.4 Conclusions	134
References	136
6 Chaotic Rheological Response in the Shear Banding Region of Cornstarch Suspensions	141
6.1 Introduction	141
6.2 Sample Preparation	143
6.3 Results and Discussions	144

6.4 Conclusion	156
References	157
7 Summary and Future Directions	161

1

Introduction

1.1 Soft matter

Soft matter refers to the broad range of condensed matter systems which includes different macromolecular materials like polymers, colloidal suspensions, self-assembling surfactant molecules, macroemulsions and biological substances such as membranes, vesicles, DNA etc. Soft materials have a range of applications as structural and packing materials, detergents, food additives, paints etc. Though there is great diversity in soft matter systems, they show some common features. The name 'soft matter' was first introduced by de Gennes for those materials that show both complexity and flexibility [1, 2]. Soft materials are viscoelastic as they show both solid and liquid like behaviors at timescales that are accessible in the laboratory. The interaction energy between structural units of soft matter is approximately $k_B T$. As a consequence, temperature plays a crucial role in determining the material structures and properties. Due to the weak interactions between the constituents of soft materials, they can be easily deformed by applying relatively small stresses

and strains. The relevant length scales in soft matter can vary between 1 and 1000 nm and are therefore much larger than atomic length scales. The relevant time scales in soft matter lie between 10^{-8} to 10^3 seconds [3] and are easily accessible in different experiments.

1.2 Examples of soft matter systems

1.2.1 Amphiphilic molecules

Amphiphiles are a special class of compounds that possess chemical groups with differing chemical affinities for water. The word amphiphile is derived from two Greek words *amphis* meaning both and *philia* meaning love or friendship. As the name suggests, one portion of an amphiphilic molecule has affinity to water and is usually known as *hydrophilic* (water-loving), while the other portion prefers to stay away from water and is called *hydrophobic* (water-fearing) or *lipophilic* (fat-loving). Amphiphiles, when dissolved in water, have a tendency to self assemble into remarkable structures. Moreover, these aggregates, each of which contains many amphiphilic molecules, may themselves associate in ordered or disordered arrangements to produce different complex phases.

Block copolymers

A polymer is a very long molecule consisting of repeating structural units (monomers) connected by covalent bonds. For a homopolymer all the monomers are identical, whereas a copolymer consists of different chemical constituents. A block copolymer has a linear and/or radial arrangement of two or more different blocks of varying monomer compositions. According to the number of blocks, a block copolymer is called di-, tri- or multi- block copolymer. These block copolymers are synthesized by sequential polymerization of the different monomers [4]. A characteristic feature of a block copolymer is the

incompatibility between unlike segments due to the different molecular structures. These different blocks show different solubilities in solution, resulting in an amphiphilic nature. These block copolymers therefore show self-organizing properties.

Surfactants

Amphiphiles that lower the surface tension of a liquid, the interfacial tension between two liquids, or that between a liquid and a solid, are often referred to as surfactants (or surface active agents). The hydrophobic portion of a surfactant molecule is made of aliphatic chains, which may be saturated or partially saturated. The hydrophilic portion, on the other hand, consists of a polar head group. The non-polar hydrocarbon tail is attached to the hydrophilic head group *via* covalent bonding.

1.2.2 Colloidal suspensions

A colloidal suspension is a heterogeneous system in which solid particles are dispersed in a continuous fluid medium. The sizes of the colloidal particles can vary from nm to μm . Colloidal suspensions remain stable in the dispersing fluid due to the random thermal motion of the colloid particles. Simultaneously, gravity tries to destabilize the suspension. If the colloidal particles are denser than the dispersing fluid, the colloidal particles will tend to sediment due to gravity. The stability of the colloidal suspension depends upon the competition between the thermal Brownian process and the sedimentation process. For the thermal diffusion of the colloidal particles, one can define a diffusion time τ_D which is the time taken by the particle to diffuse a distance equal to its radius. The diffusion time $\tau_D = a^2/D = 6\pi\eta a^3/k_B T$, where a is the radius of the particle, D is its translational diffusion coefficient, η is the viscosity of the medium and T is the temperature, is estimated using the Stokes-Einstein

relation ($D = k_B T / 6\pi\eta a$). For the sedimentation process in a dilute suspension, the sedimentation velocity v_s is calculated as $v_s = 2\Delta\rho g a^2 / 9\eta$, where $\Delta\rho$ is the density difference between the colloidal particle and the dispersing fluid. The corresponding sedimentation time is $\tau_s = a / v_s$. One can define a dimensionless gravitational Peclet number Pe as follows [5]:

$$Pe = \tau_D / \tau_s = 4\pi\Delta\rho g a^4 / 3k_B T \quad (1.1)$$

This Peclet number estimates the ratio of the time taken by a particle to diffuse its own radius to the time taken to sediment over the same length scale. For a stable colloidal suspension, $Pe < 1$. For polystyrene spheres of radius 100 nm in water, $Pe \sim 5 \times 10^{-5}$. Colloidal suspensions comprising 100 nm polystyrene particles in water are therefore stable. For 10 μm polystyrene spheres in water, $Pe \sim 5 \times 10^3$; sedimentation therefore dominates in these suspensions, making them unstable. Stable colloidal suspensions of big colloidal particles can be achieved by decreasing the density difference $\Delta\rho$ between the colloid particle and the dispersing fluid.

1.2.3 Hydrogels

Hydrogels are three dimensional cross-linked networks of hydrophilic polymers which can absorb large quantities of water. Hydrogels can be divided into two categories based on the chemical or physical natures of the cross-link junctions. Chemically cross-linked networks have irreversible junctions, which can be formed by the process of polymerization. Physical cross-links have transient junctions that arise from either polymer chain entanglements or physical interactions such as ionic interactions, hydrogen bonds or hydrophobic interactions. Gelatin gels (formed due to a coil-helix transition with decreasing temperature) [6], Ca^{2+} induced alginate gels [7], the aggregates formed by globular proteins

close to their isoelectric points [8] are some examples of physical hydrogels.

1.3 Intermolecular interactions in soft matter

The structures, surfaces and material properties of soft materials are very strongly dependent on the nature of the intermolecular forces that exist between their constituents. The relevant intermolecular interactions in soft matter systems are described below:

1.3.1 van der Waals interaction

van der Waals forces are the universal attractive forces acting between all atoms, molecules, ions etc. This short range force arises from the interactions between the dipoles of two neighboring molecules. The effective range of the van der Waals interaction can vary from 0.2 nm to 10 nm [13]. The interaction energy $V(S)$ between two identical spheres of radius R with a distance H between their centers is given by the following relation:

$$V(S) = -\frac{A}{6} \left[\frac{2}{S^2 - 4} + \frac{2}{S^2} + \ln \frac{S^2 - 4}{S^2} \right] \quad (1.2)$$

where S is defined as H/R and A is the Hamaker constant [10]. The value of Hamaker constant is of the order of 10^{-20} J and this value depends on the properties of the particles and the suspending medium [11]. For the simplest case, the net attractive interaction between two spherical particles at small separations ($H \rightarrow 2R$) can be written as

$$V(S) = \frac{-A R}{12 l} \quad (1.3)$$

where $l = H - 2R$. When the separation between the particles is very large ($H \rightarrow \infty$), then $V(S)$ can be written as

$$V(S) = -\frac{16A}{9S^6} \quad (1.4)$$

1.3.2 Electric double layer interaction

When macromolecules having ionizable groups are added to water, they are surrounded by an equal but oppositely charged region of counter ions, forming a diffuse double layer. According to Debye and Hückel, a reasonable one-dimensional representation of the potential distribution can be given by the Poisson - Boltzmann equation as [11]

$$\frac{d^2\psi}{dx^2} = -\frac{e}{\epsilon} \sum z_i n_i \exp\left(-\frac{z_i e \psi}{k_B T}\right) \quad (1.5)$$

where ψ is the potential at a distance x from the surface, ϵ is the permittivity of the medium, n_i is the bulk concentration of ions of charge z_i , e is the electronic unit charge, k_B is the Boltzmann constant and T is the absolute temperature. For low charge density, the Debye-Hückel approximation leads to the following equation:

$$\nabla^2 \psi = \kappa^2 \psi \quad (1.6)$$

where κ is called the inverse of Debye length which can be calculated as

$$\kappa = \left(\frac{\rho_\infty e^2 z^2}{\epsilon k_B T}\right)^{1/2} \quad (1.7)$$

where ρ_∞ is the bulk concentration of ions.

The solution of this equation, for a particle of radius a_0 , with a compact layer

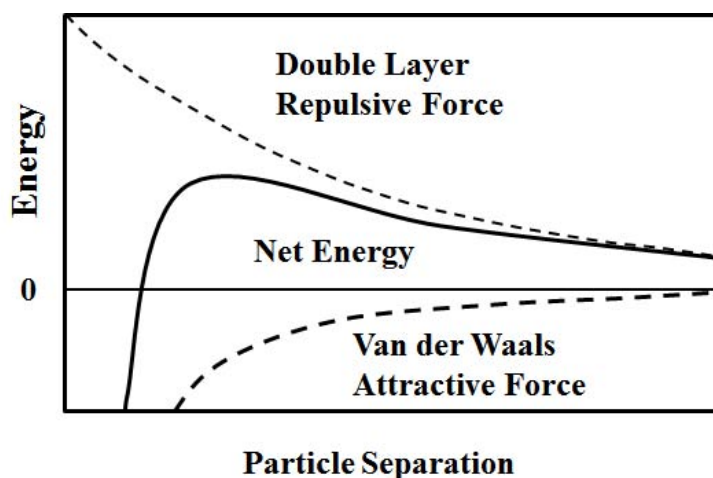


FIGURE 1.1: DLVO energy vs. distance in aqueous salt solutions. The figure is adapted from [13].

of thickness d is

$$\psi(x) = \psi_d \frac{a}{x} e^{-\kappa(x-a)} \quad (1.8)$$

where ψ_d is the potential at the beginning of the diffused double layer and $a = a_0 + d$ [11].

The overall interaction energy for a molecule in a solvent is described by the DLVO theory, where both the electrostatic double-layer interaction and van der Waals forces are taken into account [9, 12] (Fig. 1.1).

1.3.3 Hydrophobic interaction

Water molecules form hydrogen bonds between themselves. Non-polar or hydrophobic molecules like hydrocarbons are incapable of forming H bonds with water molecules. When non polar molecules are added in water, then neighboring water molecules will reorient themselves in ordered structures around the non polar molecules [13]. But this orientation of water molecules around non-polar molecules is entropically unfavorable as it disrupts the existing water structures and imposes ordering. Hydrophobic molecules therefore self assemble to minimize the number of ordered structures of water molecules,

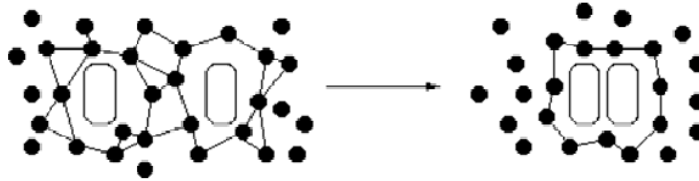


FIGURE 1.2: The hydrophobic interaction: water molecules around a non-polar solute form a cage-like structure, which reduces the entropy. When two non-polar groups associate with each other, water molecules are liberated from the solvation shell, thereby increasing the entropy. The figure is adapted from [13].

a process that leads to the reduction of the free energy of the system. (Fig. 1.2). Hydrophobic forces were first measured experimentally by Israelachvili and Pashley [14]. The hydrophobic interaction energy is found to decay exponentially in the range of 0-10 nm [15].

1.4 Some examples of phase transitions in soft matter

1.4.1 Self assembly of amphiphilic molecules:

When amphiphilic molecules or surfactants are added to an aqueous solution, these molecules reversibly self assemble to form spherical micelles above a critical concentration and temperature. In a spherical micelle, hydrophobic parts of different surfactant molecules assemble to form the core of the micelle, whereas the micellar corona is formed by the hydrophilic portions of the molecules (Fig. 1.3). The formation of micelles occurs when the surfactant concentration is above a critical micellar concentration or CMC and above a critical temperature. This temperature is called the critical micellization temperature (CMT) or the Krafft temperature. For micelle formation, the aggregation

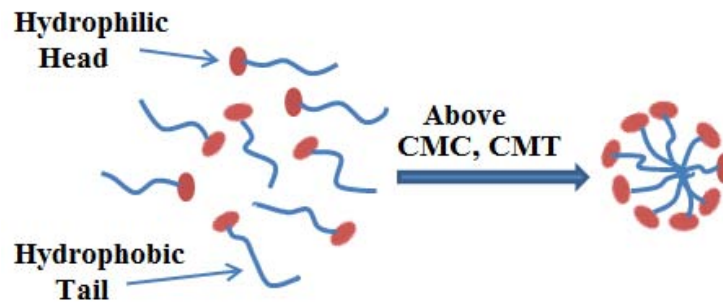


FIGURE 1.3: Sketches of micelle formation from surfactant molecules with hydrophilic head and hydrophobic tail. This figure is adapted from [13].

numbers depend upon the free energy differences between the monomers and the different structures. With further increase in surfactant concentration, these surfactant molecules will form more complex self assembled structures like bilayers, cylinders, vesicles etc. The probable structures in which the amphiphilic molecules will self-assemble depend upon a dimensionless parameter characterizing the molecule. This parameter is known as the packing parameter or shape factor $S = \frac{v_0}{a_0 l_c}$, where v_0 is the total volume occupied by the monomer, a_0 is the optimal head group area and l_c is the maximum or critical length of the hydrocarbon chain [13].

1.4.2 Jamming transition

A wide class of materials, such as foams, emulsions, colloidal suspensions, pastes, granular media and glasses exhibit jamming transitions due to macromolecular crowding. In such a transition, a flowing fluid-like state is converted to a disordered and metastable solid-like state due to the kinetic constraints imposed by the crowded environment upon the constituents. In the jammed state, the particles remain dynamically arrested and they respond elastically to small applied shear stresses. The jamming transition can be induced by varying different parameters such as temperature, density or the stress applied to

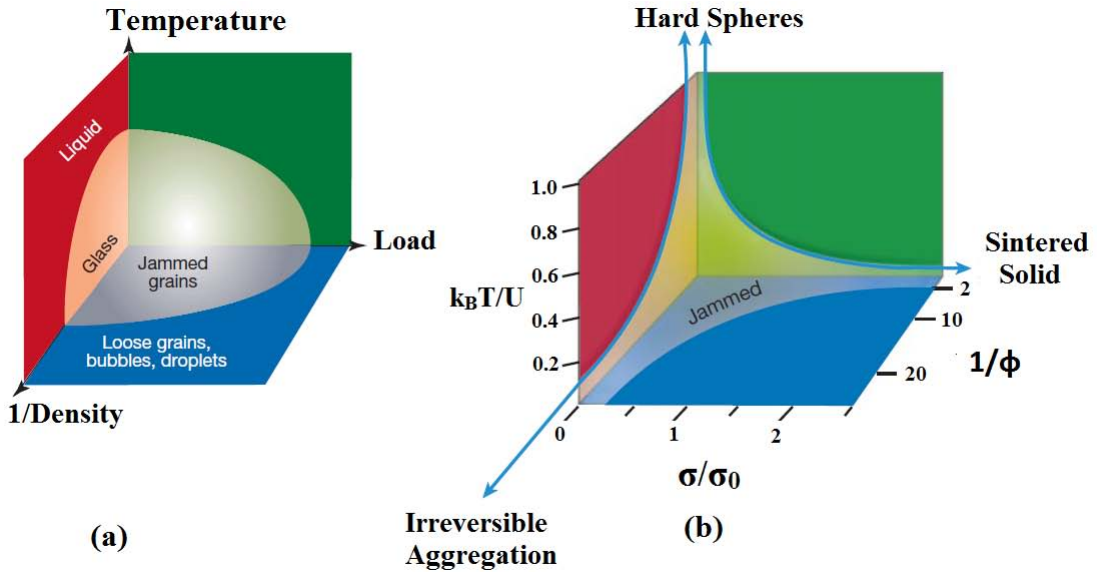


FIGURE 1.4: (a) Jamming phase diagram proposed by Liu *et al.* in the plane of inverse density ϕ^{-1} , temperature T and shear stress σ [23]. (b) Jamming phase diagram for attractive particles proposed by Trappe *et al.* [26].

the sample. Supercooled liquids form glasses due to jamming when the temperature is lowered below the glass transition temperature [16, 17]. Colloidal dispersions become colloidal glasses as their densities approach the random close packing (RCP) value [18–22]. Jammed systems can be unjammed when mechanical stresses greater than the materials' yield stresses are applied. All these features of the jamming transition are summarized by Liu and Nagel in the three dimensional jamming phase diagram [23–25] proposed by them (Fig. 1.4 (a)) in a temperature, load and 1/density space. This jamming phase diagram was later modified for attractive particles where the contribution from interparticle attractive energy U was taken into account (Fig. 1.4 (b)) [26]. According to the jamming phase diagrams, jamming can only occur in dense systems when the temperatures and applied stresses are kept low. Contrary to the suggestions of the phase diagrams reported above, the jamming phenomenon can also be triggered by the shear driven crowding of the constituents. One example of such shear induced jamming is the shear thickening behavior of

concentrated cornstarch suspensions, where cornstarch particles are seen to jam at high shear rates [27, 28]. Recent experiments on the strain induced slowing down of the dynamics of jammed aqueous foams and aging clay suspensions can also be explained by the strain induced jamming phenomenon [29, 30].

1.5 Materials studied

1.5.1 Pluronic F127

Pluronic is the generic name of symmetric triblock copolymers of the type $A_xB_yA_x$, where the central 'B' block comprises of polypropylene oxide (PPO) molecules and the end 'A' blocks comprise of polyethylene oxide (PEO) molecules. These blocks are attached to each other by covalent bonds. For Pluronic F127, the number of PEO molecules is 100 and the number of PPO molecules is 70. Pluronic F127 has a molecular weight of 12,600 g/mol, a critical micellization concentration of 0.007 g/cc and a critical micellization temperature in the range 15°-20°C. When Pluronic molecules are dissolved in certain selective solvents, they self-assemble to form micellar aggregates whose properties often mimic those of micelles formed by low molecular weight surfactants [31]. However, in contrast to normal surfactants, the aggregation of block copolymers depends more strongly on temperature. For Pluronic, the hydrophobicity of the central polypropylene oxide (PPO) increases with temperature, while the polyethylene oxide (PEO) blocks at the ends remain hydrophilic [32]. Aqueous solutions of these compounds can therefore show significant surface-activity above certain temperatures and concentrations, and can aggregate to form micelles with a dense PPO core surrounded by a corona of hydrated PEO brush-like chains [33]. With further increase in concentration and temperature, these Pluronic micelles can enter a solid-like phase that is characterized by very large values of the elastic modulus and very slow dynamics, features that

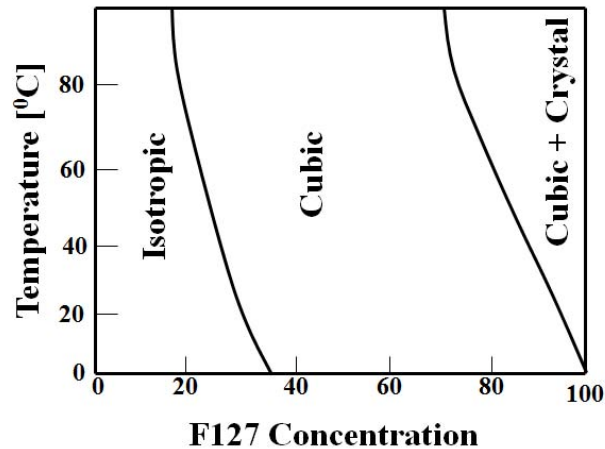


FIGURE 1.5: Phase diagram of aqueous solution of Pluronic F127. The phase diagram shows three different regions: isotropic micellar liquid, cubic phase and coexistence of cubic and liquid crystalline phases. This figure is adapted from [33].

are typically associated with soft glasses [34]. These solid like mesophases of Pluronic micelles are generally attributed to the coexistence of a close-packed crystal with a fluid [35]. Fig 1.5 shows a phase diagram for Pluronic F127, which shows an isotropic liquid phase at low concentrations. Increase in concentration of F127 results in a cubic phase which can coexist with a liquid crystalline phase at the highest concentration [33]. Detailed experiments have been performed to study the aggregation behaviors, its dependence on temperature and copolymer concentration, and its effects on the sample dynamics and phase behavior using techniques such as small angle X-ray scattering [35, 36], static light scattering [33, 37], photon correlation spectroscopy [38–40], small angle neutron scattering [36, 37, 41, 42], differential scanning calorimetry [33, 38] and rheology [34, 35, 37, 43, 44].

1.5.2 Pectin gels

Pectins, extracted from plant cell walls, are complex polysaccharides. Pectin is widely used in the food industry as a gelling agent, thickener, emulsifier and stabilizer [45]. Pectin primarily consists of linear chains of partly methyl esterified α -D-galacturonic acid, interrupted and bent in places by rhamnose units.

Depending upon the degree of esterification of the carboxyl groups of galacturonic acid with methanol, pectin can be categorized into two types. The species of pectin whose degree of methylation (molar ratio of methanol to galacturonic acid) is higher than 50% is called high methoxyl pectin, whereas pectin characterized by less than 50% degree of methylation is called low methoxyl pectin. Low methoxyl (LM) pectin can form gels in different ways that depend upon the pH of the system and the presence of Ca^{2+} or other multivalent ions. At low pH and in the absence of Ca^{2+} ions, LM pectin can form gels *via* non-ionic associations based on hydrophobic interactions and the formation of hydrogen bonds [46]. In the presence of divalent cations like Ca^{2+} , LM pectin can form gels *via* Ca^{2+} ion bridges between two carboxyl groups of two different chains. This mechanism is popularly known as egg-box mechanism and was first observed in Ca^{2+} induced alginate biopolymer gels [7, 47, 48]. Recently, small-angle X-ray scattering (SAXS), dynamic light scattering (DLS) and diffusive wave spectroscopy (DWS) were employed to report that rod-like junctions, both single ion junctions and those comprising multi-unit egg-box structures, form in these Ca^{2+} induced biopolymer gels [49, 50].

1.5.3 Cornstarch suspensions

Cornstarch particles are polydisperse colloidal particles with irregular shapes (Fig. 1.6(a)) having an average diameter of 14 μm . They are very popular in the rheological community as a prototypical shear thickener. Cornstarch suspensions show shear thinning at low shear rates followed by a discontinuous shear thickening region at high shear rates [27, 28, 51] (Fig. 1.6(b)). Bonn *et al.* have performed magnetic resonance imaging (MRI) measurements to

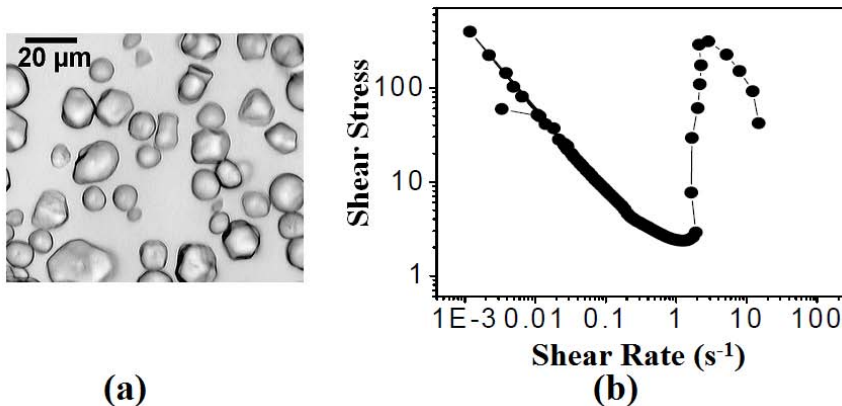


FIGURE 1.6: (a) Micrograph of cornstarch particles and (b) a typical viscosity vs. shear rate plot for a 44 wt% cornstarch suspension in a vane in cup geometry. These figures are adapted from [28]

elucidate the local flow properties of cornstarch suspensions by experimentally determining the local velocity profiles in a Couette cell [27]. They proposed that the discontinuous shear thickening observed in cornstarch suspensions is a consequence of dilatancy. The slope of the shear thickening viscosity vs. shear rate curve is found to increase with cornstarch concentration and finally diverges at a critical concentration [51]. Recent experiments on cornstarch suspensions show that the suspensions can generate very large, positive normal stresses under impact [52]. These normal stresses originate from an impact-generated dynamic jamming front that propagates through the system. The extensional rheology of cornstarch suspensions demonstrates a Newtonian response at low extension rates, followed by strain hardening and a brittle fracture at higher rates [53].

1.6 Experimental studies

This section describes the theoretical backgrounds of the two main experimental methods which have been used in this thesis.

1.6.1 Rheology

Rheology is the study of the flow and deformation of matter. Rheology measurements tell us about the mechanical responses of the material when a stress or strain is applied to it. From Hooke's law, for a purely elastic solid [54]

$$\sigma = G\gamma, \quad (1.9)$$

where σ is the applied stress and γ is the corresponding strain response. On the other hand, for a Newtonian fluid, the constitutive equation is [55]

$$\sigma = \eta\dot{\gamma}, \quad (1.10)$$

where $\dot{\gamma} = \frac{d\gamma}{dt}$ is the shear rate. Most of the materials that we encounter in everyday life show both elastic and viscous behaviors and are called viscoelastic.

(i) Linear Rheology

The development of the mathematical theory of linear rheology is based on a "superposition principle". A linear response is observed in rheological measurements when small stresses or strains are applied to viscoelastic materials in such a way that the material microstructure is not altered (Fig. 1.7 at $\gamma < \gamma_L$). This implies that the mechanical response at any time is directly proportional to the value of the initiating signal. The differential equations characterizing linear viscoelasticity are therefore linear. In this regime, for an applied strain γ at time t , the stress response σ can be written as [56]

$$\sigma(t) = G(t, t_1)\gamma(t), \quad (1.11)$$

where t_1 is a past time variable and $G(t, t_1)$ is the stress relaxation function. In the linear regime, G depends on the time difference between t and t_1 i.e. $G(t,$

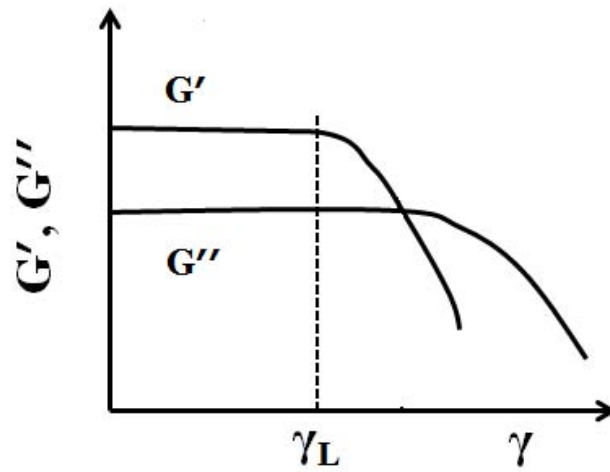


FIGURE 1.7: Typical plot of mechanical moduli with the variation of strain for a soft solid. The plot shows a linear regime for $\gamma < \gamma_L$ where mechanical moduli are independent of the strain amplitude. The non-linear regime is observed for $\gamma > \gamma_L$, where mechanical moduli decrease with increase in strain.

$t_1) = G(t - t_1)$. For a small applied shear rate $\dot{\gamma}$ at time t , the shear stress $\sigma(t)$ induced in the material can be written in the linear rheology limit as [56]

$$\sigma(t) = \int_{-\infty}^t G(t - t_1) \dot{\gamma}(t_1) dt_1 \quad (1.12)$$

(ii) Non-linear Rheology

In the non-linear rheological regime, the applied strain or strain rate is not small. The different stress responses (sinusoidal oscillations, creep, stress relaxation after step strain or steady shearing) therefore behave non-linearly. In the non-linear regime, the shear modulus is dependent on the instantaneous applied strain (Fig. 1.7 at $(\gamma > \gamma_L)$). If a large enough step strain γ is applied to a sample, the stress induced in the sample in the non-linear regime can be expressed by $\sigma(t) = G_{nl}(t, t_1, \gamma)\gamma(t)$, where G_{nl} is the relaxation modulus in the non-linear regime. The non-linear behavior of viscoelastic materials is characterized by non-zero normal stress differences, shear thinning, shear thickening, shear banding etc. The variations of shear stresses with shear rates in shear

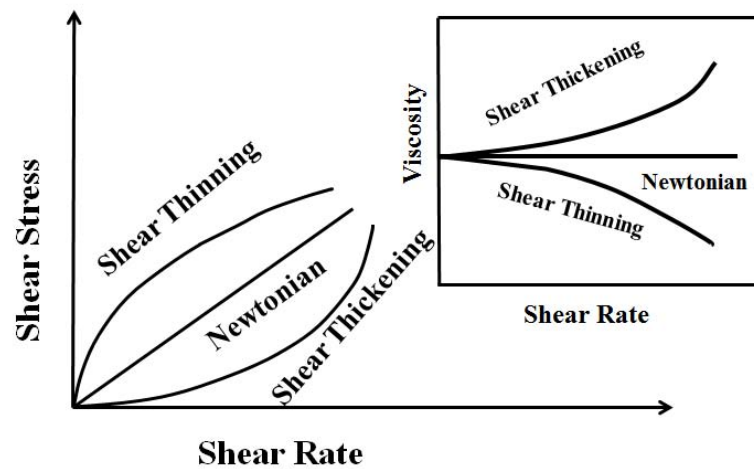


FIGURE 1.8: The different flow behaviors of viscoelastic fluids are shown. For a Newtonian fluid, shear stress increases linearly with shear rate, giving a constant viscosity (inset). For a shear thinning material, shear stress increases non-linearly with shear rate, giving a decreasing viscosity (inset). For a shear thickening material, non-linear increase in shear stress with shear rate results in an increasing viscosity (inset).

thinning and shear thickening regions are shown in Fig. 1.8.

(a) Shear thinning: Shear-thinning is said to occur when the sample viscosity decreases with increasing shear rate in steady flow (inset of Fig. 1.8). The squeezing of toothpaste from a toothpaste tube is a familiar example of shear-thinning and the existence of a non-zero yield stress. Due to this shear thinning behavior, materials that are solid-like under normal circumstances can flow when sheared or stirred above their yield stresses. The time-dependent shear-thinning behavior, where the sample returns to a steady state after the cessation of shear is called ‘thixotropy’. Non-drip paint is a common example of a thixotropic material. The shear thinning phenomenon is especially pronounced in polymer melts and in concentrated polymer solutions [56].

(b) Shear thickening: In a shear thickening material, the viscosity of the material increases with shear rate (inset of Fig. 1.8). The shear thickening phenomenon is generally observed in concentrated colloidal suspensions if

appropriate shear rates are applied to them [57, 58]. The parameters that control shear thickening behavior are particle size and particle size distribution, particle volume fraction, inter-particle interactions and the type, rate and time of shear [58]. The shear thickening phenomenon is described as a process involving the formation of jamming hydroclusters. In concentrated colloid suspensions, the strong hydrodynamic coupling between particles at high shear rates leads to the formation of hydroclusters due to shear induced jamming [59, 60]. The shear rate dependence of the flow behaviors can be described by defining a dimensionless Peclet number Pe , which relates the shear rates of flow to the particle dynamics. Pe can be written as $Pe = \frac{\dot{\gamma}a^2}{D}$, where D is the diffusion coefficient of the colloidal particles and a is the particle radius [59]. For high Pe values (high shear rates), the change in the colloid microstructures (formation of hydroclusters) cannot be restored by Brownian motion of particles, resulting in the onset of shear thickening. The change in microstructures of the shear thickening colloidal suspensions can be studied by rheo-optical [61, 62] and neutron scattering experiments [63, 64]. A common example of a shear thickening material is a cornstarch suspension, where shear induced jamming results in the increase of viscosity at high shear rates (Fig. 1.6)[27, 28].

(c) Shear banding: When the applied stress or shear strain is above a critical value, the flow of the sample can become unstable. In this unstable state, the sample separates into macroscopic coexisting bands of different local viscosities and internal structures. This phenomenon is called shear banding. Shear banding can be observed in wormlike surfactant solutions, liquid crystalline polymers, soft glasses, polymer solutions and colloidal suspensions [65]. The occurrence of shear banding can be understood by observing the plot of shear stress σ vs. shear rate $\dot{\gamma}$. In a theoretical shear stress vs. shear rate plot, steady flow cannot be sustained in the regions where $d\sigma/d\dot{\gamma}$ is negative (Fig. 1.9 (a)). This results in the formation of bands of unequal shear rates $\dot{\gamma}_1$ and

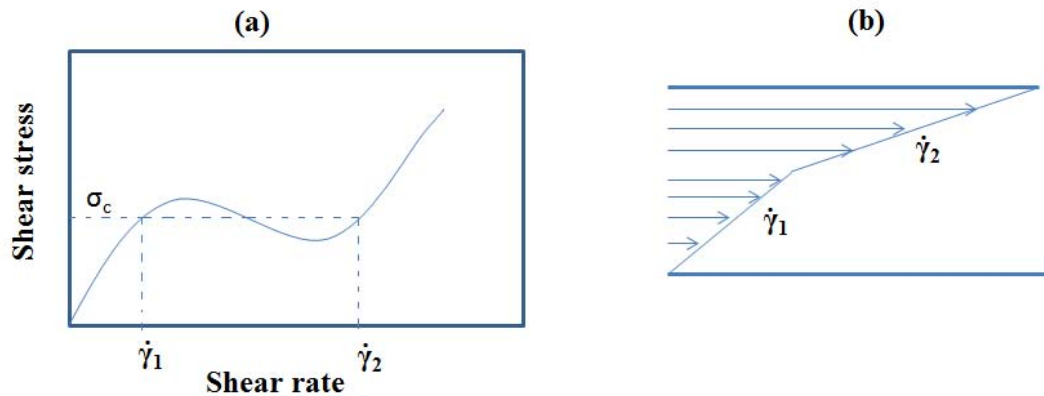


FIGURE 1.9: (a) Shear bands are formed in the regions of the flow curve with negative values of $d\sigma/d\dot{\gamma}$. In these regions, the shear bands, that can be characterized by unequal shear rates $\dot{\gamma}_1$ and $\dot{\gamma}_2$ (shown by vertical dashed lines), coexist at a common shear stress σ_c (shown by horizontal dashed line) (b) Formation of coexisting bands of unequal shear rates $\dot{\gamma}_1$ and $\dot{\gamma}_2$. This figure is adapted from [65].

$\dot{\gamma}_2$, which coexist at a common shear stress $\sigma = \sigma_c$ (Fig. 1.9 (a)) with layer normals in the flow gradient direction (Fig. 1.9 (b)) [65]. Such shear bands are called gradient bands which usually arise in a shear rate controlled environment. Shear bands of unequal shear stresses can also form at a common shear rate with layer normals in the vorticity direction in controlled stress conditions [65, 66]. They are called vorticity shear bands. Shear banding phenomena have been widely studied in worm-like surfactant systems [67, 68], liquid crystalline systems [69], polymer solutions [70], colloidal systems [71] etc.

(d) Soft glassy rheology: A diverse variety of jammed soft materials like foams, emulsions, pastes, concentrated polymer solutions etc. are characterized by structural disorder and metastability. These materials are commonly known as soft glassy materials and the rheology of these materials show qualitatively same behaviors. Linear rheology experiments on these materials show that the elastic modulus G' and viscous modulus G'' both show weak power law increases with increasing angular frequency [73, 74]. Near the glass transition, both moduli become flat. These features are explained by the soft glassy

rheology (SGR) model proposed by Sollich *et al.* [76, 77]. According to the SGR model, particles are trapped in cages formed by their neighbors. When these particles are activated, they can hop from one cage to other cage. The activation in these materials happens *via* rearrangement processes when the local yield stresses are exceeded. The interactions are described in terms of a mean-field noise temperature x . According to this model, when the system lies above the glass transition ($x > 1$), both the storage modulus G' and the loss modulus G'' vary with frequency as ω^{x-1} for $1 < x < 2$ in the limit of low frequencies. Below the glass transition ($x < 1$), this model gives $G' \sim \text{constant}$ and $G'' \sim \omega^{x-1}$ [76]. This model also predicts the existence of a macroscopic yield stress in the flow behavior of soft glassy materials.

When the nonlinear rheological properties of these materials are investigated experimentally, the soft glassy materials show some common rheological features [78–81]. The storage modulus G' shows a linear response with strain γ , which is followed by a power law decay of the form $G' \sim \gamma^\nu$. The loss modulus G'' exhibits a distinct peak before decreasing at even larger applied strains according to the form $G'' \sim \gamma^\mu$. Miyazaki *et al.* proposed a microscopic description based on mode coupling theory (MCT) theory to explain these observations in the rheology of soft glasses [75]. The model assumes that application of strains in the nonlinear rheological regime results in a decrease of the structural relaxation time τ according to the following relation: $1/\tau = 1/\tau_0 + K|\dot{\gamma}|^n$, where $\dot{\gamma}$ is the applied shear rate, τ_0 is the relaxation time in the linear rheological regime, K and n are constants. This results in the observation of a peak at $\omega \sim 1/\tau$ in G'' and the power law decreases of both G' and G'' at higher strains.

1.6.2 Dynamic Light Scattering

A medium with heterogeneities scatters light [82]. If an electromagnetic wave of frequency ω interacts with scatterers, it induces oscillating electric dipoles in the scatterers. The oscillating dipoles result in the secondary radiation of

light of the same frequency ω in all directions. This is called elastic light scattering radiation [82, 83]. The electric field associated with the incident light wave, propagating in the z direction, can be written as $E_0 = e^{-ikz+i\omega t}$, where the wavevector $k = \frac{2\pi}{\lambda}$, where λ is the wavelength of the incident light. This incident electric field E_0 can be resolved into components perpendicular (E_{0l}) and parallel (E_{0r}) to the scattering plane. The scattered electric field E_s at a distance r and for a scattering angle θ , is related to the incident electric field E_0 in the following matrix form [82, 83] ,

$$\begin{pmatrix} E_{sl} \\ E_{sr} \end{pmatrix} = \begin{pmatrix} S_2 & S_3 \\ S_4 & S_1 \end{pmatrix} \cdot \frac{e^{-ikr+ikz}}{ikr} = \begin{pmatrix} E_{0l} \\ E_{0r} \end{pmatrix} \quad (1.13)$$

where E_{sl} and E_{sr} are the scattered electric fields with polarization perpendicular to and parallel with the plane of scattering respectively [83]. S_1 , S_2 , S_3 and S_4 , which are the functions of scattering angle, are called the scattering amplitude functions. For a spherical particle, $S_3 = S_4 = 0$ [82]. In this case, the scattered intensity I_s at a distance r can be written as

$$I_s = \frac{i_1 + i_2}{2k^2 r^2} I_0 \quad (1.14)$$

where I_0 is the incident intensity, $i_1 = |S_1(\theta)|^2$ and $i_2 = |S_2(\theta)|^2$. As the scattered intensity originates from the induced dipoles in the scatterers, S_1 and S_2 can be written in terms of the polarizability α of the scatterer. If the polarizability is isotropic, then the scattered intensity at a distance r can be written as

$$I_s = \frac{(1 + \cos^2\theta)k^4 |\alpha|^2}{2r^2} I_0 \quad (1.15)$$

If we assume that the size of the spherical particle is much smaller compared to the wavelength of light, then we get Rayleigh scattering [83]:

$$I_s = \frac{8\pi^4 a^6}{\lambda^4 r^2} \left| \frac{m^2 - 1}{m^2 + 1} \right|^2 (1 + \cos^2 \theta) I_0 \quad (1.16)$$

where m is the refractive index of the particle and a is the radius of the scatterer.

According to the single scattering assumption (the number of scatterers is small and their separation is sufficiently large), the total scattered field is small compared to the external field. With this assumption, the total scattered field is the sum of the scattered electric fields of all the scatterers [82].

If all the scattered particles are identical, the scattered intensity depends only on the phase differences between the scattered electric fields. Due to the dynamics of the scatterers in solution, the phase differences between the electric fields fluctuate with time, resulting in the fluctuation of the scattered intensity. The time required for the intensity to fluctuate between the two extremes is roughly equal to the time required by two scatterers to move a distance that is sufficient to change the phase of the scattered light from 0 to π radians [85]. The time between the maxima and minima to occur at the same spot on a screen therefore gives us information about the dynamics of the scatterers in the solution. The analysis of the fluctuation of the scattered electric field or scattered intensity is performed by measuring autocorrelation functions. The autocorrelation function $g_1(\tau)$ for a time dependent electric field $E(t)$ is defined as [84, 85]

$$g_1(\tau) = \frac{1}{2T} \lim_{T \rightarrow \infty} \int_{-T}^T E(t)E(t + \tau)dt \quad (1.17)$$

where T is the sampling time and τ is the delay time.

In a dynamic light scattering (DLS) experiment, we measure the autocorrelation function of the scattered intensity $g_2(\tau)$, which is defined as [85, 86],

$$g_2(\tau) = \frac{1}{2T} \lim_{T \rightarrow \infty} \int_{-T}^T I(t)I(t + \tau)dt \quad (1.18)$$

Here, $g_1(\tau)$ and $g_2(\tau)$ are the second order and fourth order moments of $E(t)$ respectively. For a dilute solution, the scatterers undergo random motion. If the number of scatterers is large, the central limit theorem predicts that $E(t)$ has a Gaussian distribution. For this case, the fourth order moment of $E(t)$ can be reduced to an expression in terms of the second order moments of $E(t)$. This results in the Siegert relation [87]:

$$g_2(\tau) = 1 + A|g^{(1)}(\tau)|^2, \quad (1.19)$$

where A is the coherence factor which depends upon the scattering volume and the detector optics. $g_2(\tau)$ is measured in a DLS experiment and modeled appropriately to extract the scatterer dynamics.

1.7 Chaotic dynamics in dissipative systems:

Chaos represents the irregular dynamics of a dynamical system which arises from strictly deterministic laws [88]. Unlike stochastic noise, which has no predictability, chaotic dynamics are characterized by short time predictability. In addition, chaotic dynamics are very sensitive to the initial conditions and can be described by m coupled differential equations [88]:

$$\frac{dx_i}{dt} = F_i(x_1, x_2, \dots, x_N, P) \quad i = 1, 2, \dots, m \quad (1.20)$$

where x_i is a phase space variable and P is a control parameter. Depending upon the value of P , a dynamical system can show either steady state, periodic or deterministic chaotic behavior. An example of a system showing chaotic dynamics is the Hénon map, which is described by the following differential equations:

$$x_{n+1} = y_n + 1 - ax_n^2 \quad (1.21)$$

$$y_{n+1} = bx_n, \quad (1.22)$$

where a and b are control parameters.

A dissipative system is usually characterized by the presence of an attractor. An attractor is a low dimensional subset of the phase space to which the initial non-zero phase space converges asymptotically with the advancement of time [88]. For a dissipative chaotic system, the attractor often shows a very intricate geometrical structure that can be characterized in terms of a non-integer or fractal dimension, the correlation dimension ν_0 . Such an attractor is called a strange attractor. One of the most important characteristics of chaotic dynamics is an exponential sensitivity to the initial conditions. If two nearby points in phase space have a separation $|\nabla 0|$ at an initial time $t = 0$, and a separation $|\nabla t|$ at time t , then for chaotic dynamics, $\frac{|\nabla t|}{|\nabla 0|} = \exp(h t)$, where h is positive and is called the Lyapunov exponent.

Chaos was first described mathematically by Lorenz in his work on weather prediction, where deterministic equations that were previously used to describe hydrodynamical systems [89] were employed. One example of chaotic dynamics in a classical hydrodynamic system is Rayleigh-Bernard convection, where a fluid, subjected to gravity, is contained between two plates maintained at a temperature gradient ΔT . As ΔT is increased gradually, convective circular currents in the fluid can go from regular to chaotic.[90–92].

Chaotic behavior is also observed in the rheological responses of different samples in their shear banding regions. Such chaotic behavior is known as

'rheological chaos' or simply 'rheochaos' [93]. Rheo-chaos was first observed in semi-dilute solutions of surfactant cetyltrimethyl ammonium tosylate (CTAT) which forms giant wormlike micelles in solution. It was observed that when a CTAT solution is sheared at a constant shear rate that lies in the metastable region of the flow curve, the stress fluctuation data is found to be characterized by a finite correlation dimension and a positive Lyapunov exponent. These signatures confirm the existence of deterministic chaotic behavior in these sheared surfactant solutions [94]. It was seen in another work that CTAT solutions follow the Type-II intermittency route to chaos [95, 96]. Chaotic flow behaviors were also observed in other systems like shear thickening solutions of micelles [97], lamellar phases of surfactant solutions [98], concentrated colloidal suspensions [99] etc.

1.8 Thesis Organization

This thesis employs dynamic light scattering and rheological studies to investigate the structure, dynamics and the mechanical properties of some aqueous soft matter systems including micellar copolymer solutions, biopolymer gels and concentrated colloidal suspensions. The background material necessary to understand the thesis work is described in Chapter 1. Chapter 2 presents a detailed description of the experimental techniques and data analysis methods that are used. The jamming-unjamming transition of micelle-forming triblock copolymer (Pluronic F127) solutions and the effects of surfactant (SDS) addition on this jamming transition are described in Chapter 3. In Chapter 4, the effects of drug hydrophobicity, temperature and pH on drug encapsulated Pluronic micelles in dilute solution are discussed. The microscopic dynamics of the gelation process and the rupture of gel networks of salt induced biopolymer pectin solutions are described in Chapter 5. In Chapter 6, the non-linear rheology of concentrated cornstarch suspensions is described. Chapter

7 summarizes the main results of this thesis and discusses the scope for future work.

References

- [1] P. G. de Gennes, *Science*, **256**, 495 (1992).
- [2] P. G. de Gennes, *Rev. Mod. Phys.*, **64**, 645 (1992).
- [3] P. N. Pusey, *Colloidal Suspensions, Liquids, Freezing and the Glass Transition*, (Elsevier, Amsterdam , 1991).
- [4] G. Reiss, *Prog. Poly. Sci.*, **28**, 1107 (2003).
- [5] S. Ramaswamy, *Advances in Physics*, **50**, 297 (2001).
- [6] M. Djabourov, J. Leblond and P. Papon, *J. Phys. France*, **49**, 319 (1988).
- [7] I. Braccini and S. Perez, *Biomacromol.*, **2**, 1089 (2001).
- [8] D. Durand, J. C. Gimel and T. Nicolai, *Physica A*, **304**, 253 (2002).
- [9] E. J. W. Verwey and J. T. G. Overbeek, *The theory of stability of liophobic colloids*, (Elsevier, Amsterdam, 1948).
- [10] H. C. Hamaker, *Physica*, **4**, 1058 (1937).
- [11] R. J. Hunter, *Foundations of Colloidal Science* , Volume I, (Oxford University Press, New York, 1987).

-
- [12] B. V. Derjaguin and L. D. Landau, *Acta Physicochim, USSR*, **14**, 633 (1941).
- [13] J. N. Israelachvili, *Physics of Amphiphiles: Micelles, Vesicles and Microemulsions*, (North Holland, Amsterdam, 1985).
- [14] J.N. Israelachvili and R.M. Pashley, *J. Coll. Int. Sci.*, **98**, 500 (1984).
- [15] C. J. van Oss, *Interaction Forces in Aqueous Media* (Marcel Dekker, New York, 1994).
- [16] F. H. Stillinger, *Science*, **267**, 1935 (1995).
- [17] P. G. Debenedetti and F. H. Stillinger, *Nature*, **410**, 259(2001).
- [18] P. N. Pusey and W. van Megen, *Nature*, **320**, 340 (1986).
- [19] P. N. Pusey and W. van Megen, *Phys. Rev. Letter*, **59**, 2083 (1987).
- [20] P. G. Bolhuis and D. A. Kofke, *Phys. Rev. E*, **54**, 634 (1996).
- [21] W. van Megen and S. M. Underwood, *Phys. Rev. Lett.*, **70**, 2766 (1993).
- [22] J. D. Bernal and J. Mason, *Nature*, **188**, 910 (1960).
- [23] A. J. Liu and S. R. Nagel, *Nature*, **396**, 21 (1998).
- [24] C. S. O' Hern, L. E. Silbert, A. J. Liu and S. R. Nagel, *Phys. Rev. E*, **68**, 011306 (2003).
- [25] Z. Zhang, N. Xu, D. T. N. Chen, P. Yunker, A. M. Alsayed, K. B. Aptowicz, P. Habdas, A. J. Liu, S. R. Nagel and A. G. Yodh, *Nature*, **459**, 230 (2009).
- [26] V. Trappe, V. Prasad, L. Cipelletti, P. N. Segre and D. A. Weitz, *Nature*, **411**, 772 (2001).
- [27] A. Fall, F. Bertrand, G. Ovarlez and D. Bonn. *Phys. Rev. Lett.*, **100**, 018301 (2008).

-
- [28] A. Fall, F. Bertrand, G. Ovarlez and D. Bonn., *J. Rheol.*, **56**, 575 (2012).
- [29] A. D. Gopal and D. J. Durian, *Phys. Rev. Lett.*, **91**, 188303 (2001).
- [30] R. Bandyopadhyay, P. H. Mohan and Y. M. Joshi, *Soft Matter*, **6**, 1462 (2010).
- [31] W. Loh, *Encyclopedia of Surface and Colloid Science* (Marcel Dekker, New York, 2002).
- [32] J. N. Israelachvili, *Proc. Natl. Acad. Sci.*, **94**, 8378 (1997).
- [33] G. Wanka, H. Hoffmann and W. Ulbricht, *Macromol.*, **27**, 4145 (1994).
- [34] P. Harsha Mohan and R. Bandyopadhyay, *Phys. Rev. E*, **77**, 041803 (2008).
- [35] V. Castelletto, C. Caillet, J. Fundin, I. W. Hamley, Z. Yang and A. Kelarakis, *J. Chem. Phys.*, **116**, 10947 (2002).
- [36] V. Castelletto, I. W. Hamley, X.-F. Yuan, A. Kelarakis and C. Booth, *Soft Matter*, **1**, 138 (2005).
- [37] L. Lobry, N. Micali, F. Mallamace, C. Liao and S.-H. Chen, *Phys. Rev. E*, **60**, 7076 (1999).
- [38] P. Alexandridis, T. Nivaggiolli and T. Alan Hatton, *Langmuir*, **11**, 1468 (1995).
- [39] B. Nystrom and A-L. Kjoniksen, *Langmuir*, **13**, 4250 (1997).
- [40] M. M. Jebari, N. Ghaouar, A. Aschi and A. Gharbi, *Polymer International* **55**, 176 (2006).
- [41] K. Mortensen, W. Brown and E. Jorgesen, *Macromol.*, **27**, 5654 (1994).
- [42] H. Yardimci, B. Chung, J. L. Harden and R. L. Leheny, *J. Chem. Phys.* **123**, 244908 (2005).

-
- [43] R. K. Prud'homme, G. Wu and D. K. Schneider, *Langmuir*, **12**, 4651 (1996).
- [44] B. K. Lau, Q. Wang, W. Sun and L. Li, *J. Poly. Sc.*, **42**, 2014 (2004).
- [45] B. R. Thakur, R. K. Singh and A. K. Handa, *Critical Reviews in Food Science and Nutrition*, **37**, 47 (1997).
- [46] P. Gilseman, R. Richardson and E. Morris, *Carbohydrate Polymers*, **41**, 339 (2000).
- [47] G. Ravanat and M. Rinaudo, *Biopolymers*, **19**, 2209 (1980).
- [48] E. R. Morris, D. A. Rees, D. Thom and J. Boyd, *Carbohydrate Research*, **66**, 145 (1978).
- [49] I. Ventura, J. Jammal, H. Bianco-Peled, *Carbohydrate Polymers*, **97**, 650 (2013).
- [50] D. Larobina and L. Cipelletti, *Soft Matter*, **9**, 10005 (2013).
- [51] E. Brown and H. M. Jaeger, *Phys. Rev. Lett.*, **103**, 086001 (2009).
- [52] S R Waitukaitis and H M Jaeger, *Nature*, **487**, 205 (2012)
- [53] E. E. White, M. Chellamuthu and J. P. Rothstein, *Rhol. Acta*, **49**, 119, 2009.
- [54] R. Hooke, *Lectures de Potentia Reestitution*, (1678).
- [55] I. S. Newton, *Principia Mathematica* (1687).
- [56] C. W. Macosko, *Rheology: Principles, Measurements and Applications*, (VCH Publishers, New York, 1993).
- [57] R. L. Hoffman, *J. Coll. Int. Sc.*, **46**, 491 (1974).
- [58] H. A. Barnes, *J. Rheol.*, **33**, 329 (1989).

- [59] N. J. Wagner and J. F. Brady, *Phys. Today*, **27** (2009).
- [60] D. R. Foss and J. F. Brady, *J. Fluid Mechanics*, **407**, 167 (2000).
- [61] P. D. D'Haene, J. Mewis and G. G. Fuller, *J. Coll. Int. Sc.*, **156**, 350 (1993)
- [62] J. W. Bender and N. J. Wagner, *J. Coll. Int. Sc.*, **172**, 171 (1995).
- [63] J. W. Bender and N. J. Wagner, *J. Rheol.*, **40**, 899 (1996).
- [64] H. M. Laun, R. Bung, S. Hess, W. Loose, K. Hahn, E. Hadicke, R. Hingmann, F. Schmidt and P. Lindner, *J. Rheol.*, **36**, 743 (1992).
- [65] S. M. Fielding, *Soft Matter*, **3**, 1262 (2007).
- [66] J. K. G. Dhont and W. J. Briels, *Rheo. Acta*, **47**, 257 (2008).
- [67] V. Schmitt, F. Lequeux, A. Pousse and D. Roux, *Langmuir*, **10**, 955 (1994).
- [68] J. F. Berret, D. C. Roux, G. Porte and P. Lindner, *Europhys. Lett.*, **25**, 521 (1994).
- [69] C. Pujolle-Robic and L. Noirez, *Nature*, **409**, 167 (2001).
- [70] L. Hilliou and D. Vlassopoulos, *Ind. Eng. Chem. Res.*, **41**, 6246 (2002).
- [71] L. B. Chen, C. F. Zukoski, B. J. Ackerson, H. J. M. Hanley, G. C. Straty, J. Barker and C. J. Glinka, *Phys. Rev. Lett.*, **69**, 688 (1992).
- [72] S. M. Fielding, M. E. Cates and P. Sollich, *J. Rheol.*, **44**, 323 (2000).
- [73] M. R. Mackley, R. T. J. Marshall, J. B. A. F. Smeulders, and F. D. Zhao, *Chem. Eng. Sci.*, **49**, 2551 (1994).
- [74] R. J. Ketz, R. K. Prudhomme, and W. W. Graessley, *Rheol. Acta*, **27**, 531 (1988).
- [75] K. Miyazaki, H. M. Wyss, D. A. Weitz and D. R. Reichman, *Europhys. Lett.*, **75**, 915 (2006).

-
- [76] P. Sollich, F. Lequeux, P. Hebraud and M. E. Cates, Phys. Rev. Lett., **78**, 2020 (1997).
- [77] P. Sollich, Phys. Rev. E, **58**, 738 (1998).
- [78] V. Tirtaatmadja, K. C. Tam and R. D. Jenkins, Macromolecules **30**, 1426 (1997).
- [79] S. R. Raghavan and S. A. Khan, J. Rheol., **39**, 1311 (1995).
- [80] G. Petekidis et al., Phys. Rev. E, **66**, 051402 (2002).
- [81] T. G. Mason et al., Phys. Rev. Lett., **75**, 2051 (1995).
- [82] C. F. Bohren and D. R. Huffman, Absorption and Scattering of Light by Small Particles, (Willey-VCH, Weinheim, 1998).
- [83] V. D. Hulst, Light Scattering by Small Particles., (John Wiley & sons., New York, 1957).
- [84] B. J. Berne and R. Pecora, Dynamic Light Scattering, (Wiley-Interscience, New York, 1976).
- [85] R. Pecora, Dynamic Light Scattering, (Plenum, New York, 1985).
- [86] B. Chu, Laser Light Scattering, (Academic, New York, 1974).
- [87] P. A. Lemieux and D. J. Durian, J. Opt. Soc. Am., **16**, 1651 (1999).
- [88] E. Ott, Chaos in Dynamical Systems, (Cambridge University Press, New York, 2002).
- [89] E. N. Lorenz, J. atmospheric Sc., **20**, 130 (1963).
- [90] G. Ahlers and R. L. Behringer, Phys. Rev. Lett., **40**, 712 (1978).
- [91] J. P. Gollub and S. V. Benson, J. Fluid Mechanics, **100**, 449 (1980).

- [92] A. Libchaber and J. Maurer, J. Phys. (Paris) Coll. **41**, C3 (1980).
- [93] M. E. Cates, D. A. Head and A. Ajdari, Phys. Rev. E, **66**, 025202 (2002).
- [94] R. Bandyopadhyay, G. Basappa and A. K. Sood, Phys. Rev. Lett., **84**, 2022 (2000).
- [95] R. Ganapathy and A. K. Sood, Phys. Rev. Lett., **96**, 108301 (2006).
- [96] A. K. Sood and R. Ganapathy, Pramana, **67**, 33 (2006).
- [97] R. Bandyopadhyay and A. K. Sood, Europhys. Lett., **56**, 447 (2001).
- [98] J. B. Salmon, A. Colin and D. Roux, Phys. Rev. E, **66**, 031505 (2002).
- [99] D. Lootens, H. V. Damme and P. Hebraud, Phys. Rev. Lett., **90**, 178301 (2003).

2

Experimental Techniques and Data Analysis

2.1 Introduction:

This chapter describes the different experimental techniques and data analysis methods that have been used in this thesis work. The two main experimental techniques used in this thesis work are rheology and dynamic light scattering (DLS). Bulk rheological measurements are performed with the help of a stress controlled rheometer. A brief description of a rheometer and the measurement methods of different rheological moduli can be found in section 2.2. Experiments on microscopic dynamics of different soft matter systems are carried out in a DLS setup, which is described in section 2.3. Other experimental techniques such as cryogenic scanning electron microscopy (Cryo-SEM) imaging, fluorescence spectroscopy and small angle X-ray scattering (SAXS) are also

used to support the rheological and DLS results. Cryogenic scanning electron microscopy (Cryo-SEM) imaging (described in section 2.4) allows direct visualization of different soft matter systems. Section 2.5 describes fluorescence spectroscopy methods, which gives information regarding the micellar core environment. Small angle X-ray scattering (SAXS) techniques are described in section 2.6. In the data analysis section, we describe nonlinear time series analysis methods, which are commonly used to analyze chaotic dynamics. These analysis methods are used to calculate certain dynamical invariants to determine whether the irregular time evolution of experimentally measurable parameters arises due to deterministic chaos or random noise.

2.2 Experimental techniques:

2.2.1 Rheological measurements:

Rheology is a very important technique to characterize mechanical properties of soft matter by studying their flow and deformation behaviors. The measurements of rheological quantities can be performed using a rheometer. A rheometer can be either stress controlled or strain controlled, depending upon the control parameter (stress or strain).

For our work, a modular compact Anton Paar MCR 501 rheometer is used to perform all the rheological measurements. This is a stress controlled rheometer. In this rheometer, a known stress (torque) is applied to the material under study and the resultant strain is measured. We can also use this rheometer to control strain or shear rate by a feedback mechanism [1]. Fig. 2.1 shows a schematic diagram of the main components of the Anton Paar MCR 501 rheometer. This rheometer includes an air bearing-supported synchronous motor. The motor of the rheometer consists of permanent magnets. These magnets are mounted on a small rotor disc and produce a constant magnetic

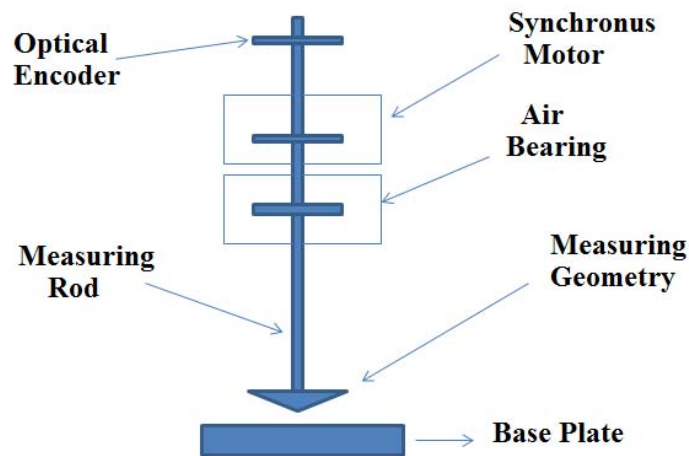


FIGURE 2.1: Schematic diagram of the main components of the Anton Paar MCR series rheometer. The figure is adapted from [1].

field, providing a delay-free response. The rotor moves synchronously with the stator field produced by a series of coils [1]. The existence of air bearing results in almost friction free motion of the motor. This helps to achieve very low torques (upto 2 nN.m with a resolution of 0.01 nN.m) in rheometric measurements. The air bearing also contains a normal force transducer which helps to detect natural movements of the air bearing due to the presence of normal forces in the range between 0.01 μ N.m to 300 mN.m with a resolution of 0.01 nN.m.

A high-resolution optical encoder is included in this rheometer to measure the strain. This optical encoder enables precise measurements of the angular deflection with a resolution $< 1 \mu$ rad [1]. All the rheological data are acquired using the Rheoplus software (version 3.40) provided by the manufacturer. A water circulation unit Viscotherm VT2 is used to control the temperature of the sample in the measuring cell in the range between 5°C and 80°C with temperature stability $\pm 0.1^\circ\text{C}$.

During measurement, a measuring geometry is attached to the rotating rod of the rheometer and lowered onto the sample using the TruGap™ technique providing with the rheometer. Depending on the experimental requirements

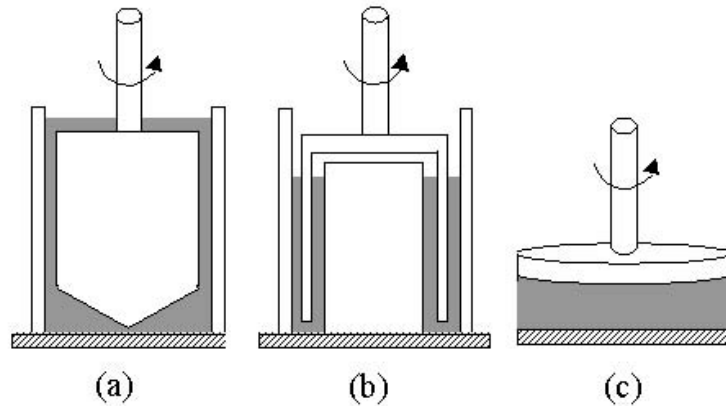


FIGURE 2.2: Different measuring geometries: (a) concentric cylinder, (b) double gap and (c) parallel plate geometries. The figure is adapted from [1].

and the nature of the system to be studied, we have used different types of measuring geometries. These different geometries are described below:

Concentric cylinder geometry: The concentric cylinder geometry consists of a co-axially arranged cylindrical cup and a rotating cylindrical bob (Fig. 2.2(a)). The test fluid is kept in the annulus between the cylinder surfaces. The concentric cylinder CC17 geometry, used in our experiments, has a gap of 0.71 mm and an effective length of 24.99 mm. This geometry requires a sample volume of 4.72 ml for every run. In this geometry, one can measure shear stresses in the range between 771.345×10^{-6} Pa and 17740.935 Pa, shear strains above 1.23×10^{-5} and strain rates between $1.283 \times 10^{-7} \text{s}^{-1}$ and $3.849 \times 10^3 \text{s}^{-1}$.

Double gap geometry: The double-gap geometry is a special type of concentric cylinder geometry, where the cylindrical bob is replaced by a inner hollow cylinder resulting in two gaps between the cylinder surfaces (Fig. 2.2 (b)). This geometry is very useful for low viscosity fluids, as it increases the total surface area of the sample in contact, and therefore the viscous drag, on the rotating inner cylinder. The double gap DG26.7/Q1 geometry, which we have used in our experiments, has a gap of 1.886 mm, an effective length of

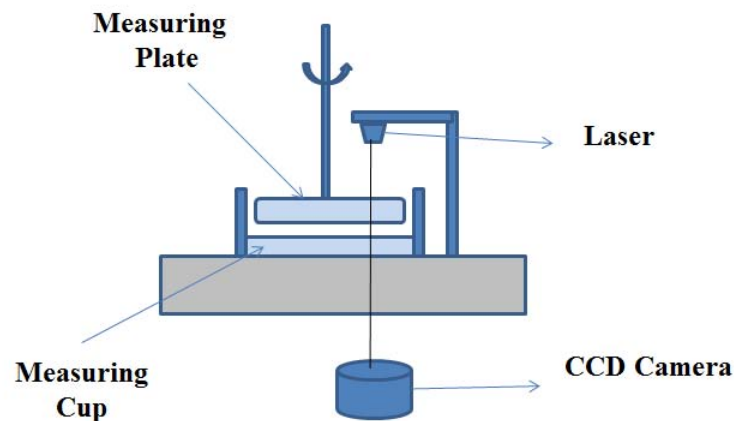


FIGURE 2.3: Experimental setup for a rheo-SALS measurement.

40 mm and requires a sample volume of 3.8 ml for every run. It can measure shear stresses in the range between 109.407×10^{-6} Pa and 2516.361 Pa, shear strains above 2.93×10^{-5} and strain rates between $3.0697 \times 10^{-7} \text{ s}^{-1}$ and $9.209 \times 10^3 \text{ s}^{-1}$.

Parallel plate geometry: The parallel plate geometry consists of two parallel plates separated by a gap (Fig. 2.2 (c)). The upper plate can rotate and the gap between the plates can be controlled. This parallel plate geometry is usually used for viscoelastic materials which are unlikely to flow out of the geometry after the sample is loaded. One of the advantages of this geometry is that the sample volume can be controlled by changing the distance between plates. The PP43/GL geometry supplied by the manufacturer has an upper plate diameter $R = 42.89$ mm. The required volume of sample for this geometry with a plate gap of 1 mm is 1.45 ml.

Rheo-SALS system: Rheo-SALS is one of the most widely used techniques for getting structural information of the sample when the sample is under flow. In this technique, rheological and small angle light scattering measurements are simultaneously performed. This technique is quite useful for understanding systems whose rheological properties depend on their microstructures. The schematic diagram of a rheo-SALS setup is shown in Fig. 2.3. This

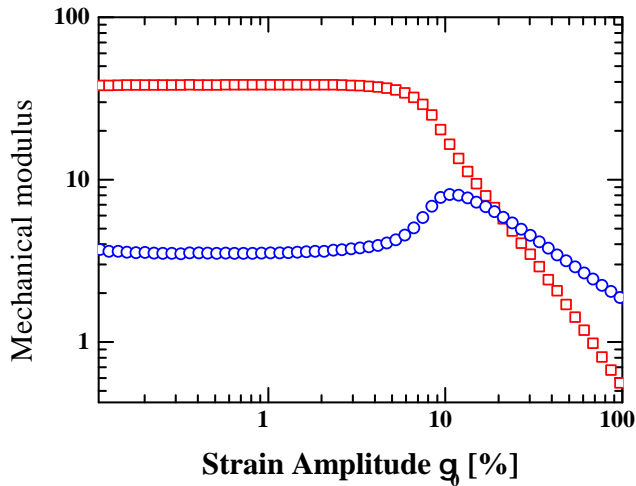


FIGURE 2.4: Plot of amplitude sweep measurement of 2.5 g/L pectin sample containing 6 mM CaCl_2 at 25°C. The angular frequency ω is kept constant at 1 rad/s, while the amplitude of the strain γ_0 is increased logarithmically from 0.1% to 100%. The figure shows a linear regime for the strain $\gamma_0 \leq 4\%$.

system includes a parallel plate measuring system which has a glass bottom plate and a rotating upper glass plate of diameter 43 mm. Polarized light from a laser diode with a wavelength of 658 nm is incident on the sample in the measuring system. The light scattered by the sample is collected by a CCD camera. The angular distribution and the magnitude of the scattered intensity is measured and analyzed to get structural information of the sample.

Applications of the rheometer:

The Anton Paar MCR 501 rheometer can perform different rheological measurements. Some of the basic applications of the rheometer are discussed below. In an oscillatory rheology measurement, a sinusoidal strain ($\gamma = \gamma_0 \sin \omega t$) is applied to the material and the corresponding stress response $\sigma(t) (= \gamma_0 e^{i\omega t} G^*(\omega))$ is measured, where $G^*(\omega)$ is the complex shear modulus [2]. In oscillatory measurements, rheological properties are characterized by the complex shear

modulus $G^*(\omega)$, which can be written as

$$G^*(\omega) = G'(\omega) + iG''(\omega) \quad (1.14)$$

where $G'(\omega)$ and $G''(\omega)$ are the elastic modulus and viscous modulus of the material respectively. The ratio of these mechanical moduli is called loss factor $\tan\delta = G''(\omega)/G'(\omega)$. Most oscillatory measurements are performed in the following different ways:

- **Amplitude sweep:** In amplitude sweep measurements, the amplitude of the applied oscillatory strain (γ_0) is increased, while the frequency of the strain ω remains constant and the corresponding $G'(\omega)$, $G''(\omega)$ and $\eta^*(\omega)$ are measured. Fig. 2.4 shows a plot of amplitude sweep measurements for an aqueous solution of 2.5 g/L pectin containing 6 mM CaCl_2 , which is in a soft solid phase at 25°C. The range of the amplitudes of the applied strain, where the mechanical moduli show constant values, is defined as linear regime. In this case, the linear regime is seen when $\gamma_0 \leq 4\%$

- **Frequency sweep:** In frequency sweep measurements, the amplitude of the applied oscillatory strain γ_0 is kept constant, the frequency of the oscillatory strain varies with time and the corresponding $G'(\omega)$, $G''(\omega)$ and $\eta^*(\omega)$ are calculated. Frequency sweep measurements are generally performed in the linear regimes of the viscoelastic materials. Fig 2.5 shows the plots of G' and G'' for a 2.5 g/L pectin solution containing 6 mM CaCl_2 at 25°C, where the amplitude of strain is kept constant at 0.2%. As the sample lies in the soft glassy regime, G' remains constant in the applied frequency range, whereas G'' is weakly dependent on frequency and G' has a much higher value than G'' .

Flow experiments:

In a flow experiment, a rotational shear strain or shear rate is applied to the sample to estimate the flow properties of the samples by measuring the shear

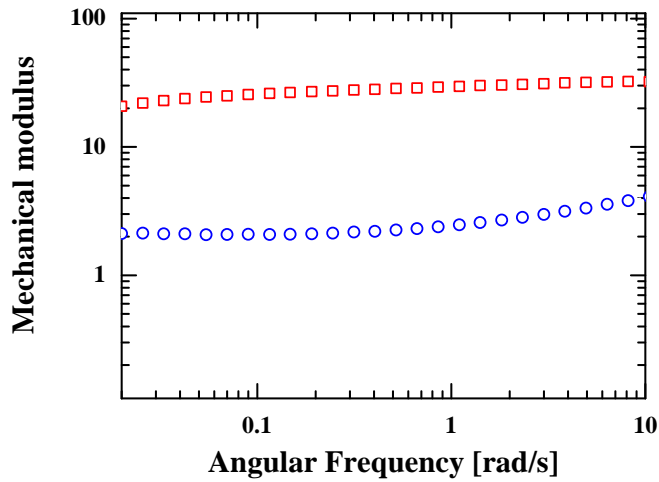


FIGURE 2.5: Plot of frequency sweep measurements of 2.5 g/L pectin sample containing 6 mM CaCl_2 when γ_0 is kept constant at 0.2 % at 25°C.

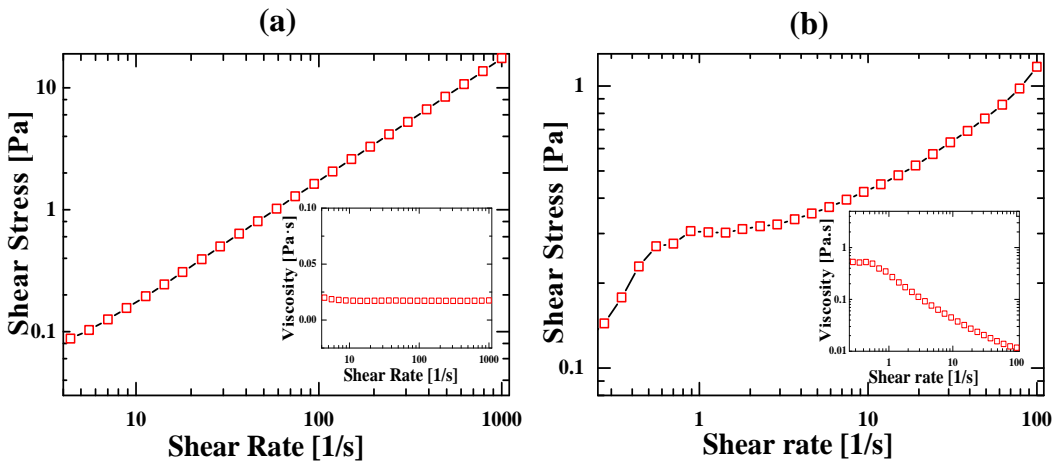


FIGURE 2.6: Flow curves of (a) silicon oil and (b) 2.5 g/L pectin gel with 6 mM added CaCl_2 . The insets of (a) and (b) show the viscosity vs. shear rate plots of silicon oil and 2.5 g/L pectin gel with 6 mM added CaCl_2 respectively.

stress response (σ) or viscosity (η). The flow properties that are more often investigated are shear thinning, shear thickening or shear banding behaviors, creep and recovery behaviors and stress relaxation. The relevant flow experiments are discussed below:

- **Flow curves and viscosity measurements:** The flow curve is measured

by increasing the shear rate or stress and measuring the resultant shear stress or strain rate. This information is used to measure the sample viscosity. Fig. 2.6 (a) shows the flow curve and the corresponding viscosity plot of silicon oil. The viscosity of silicon oil is independent of the applied shear rate, therefore revealing Newtonian liquid behavior. Fig. 2.6 (b) shows the shear thinning behavior of a 2.5 g/L pectin gel with 6 mM added CaCl_2 salt with viscosity decreasing with increasing shear rate.

- **Creep and recovery test:** In the creep test, the time-dependence of the strain that develops due to the application of a constant stress on the sample is recorded. In the recovery test, the time-dependence of the strain is measured after the removal of the applied stress. Fig. 2.7 shows the plot of strain evolution for a 2.5 g/L pectin gel containing 6 mM CaCl_2 at 25°C , when a constant stress is applied. When the applied stress is removed from the sample, the strain relaxes to a non-zero plateau value indicating the incorporation of permanent strain in the gel structure.

- **Stress relaxation:** A stress relaxation measurement is performed by observing the stress variation when a step shear rate is applied to the system throughout the experimental duration. For a 39% cornstarch suspension, the sample does not relax to a steady state for a imposed step shear rate of 30 s^{-1} and large fluctuations are observed in the stress response, suggesting the possible existence of chaotic behavior (shown by red line in Fig. 2.8). No such fluctuation is observed when a lower shear rate (1 s^{-1}) is applied to the same sample.

2.2.2 Dynamic light scattering:

Experimental setup

In a dynamic light scattering (DLS) measurement, the microscopic dynamics of the scatterers in solution is studied by measuring the autocorrelation function

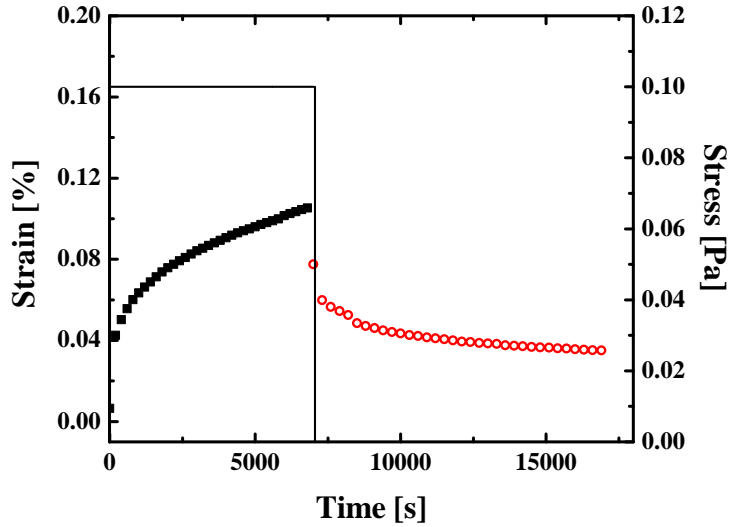


FIGURE 2.7: Strain variation during a creep (black squares) and recovery (red circles) test for 2.5 g/L pectin gel containing 6 mM CaCl_2 at 25°C is plotted. The applied stress during this experiment is also plotted (black line).

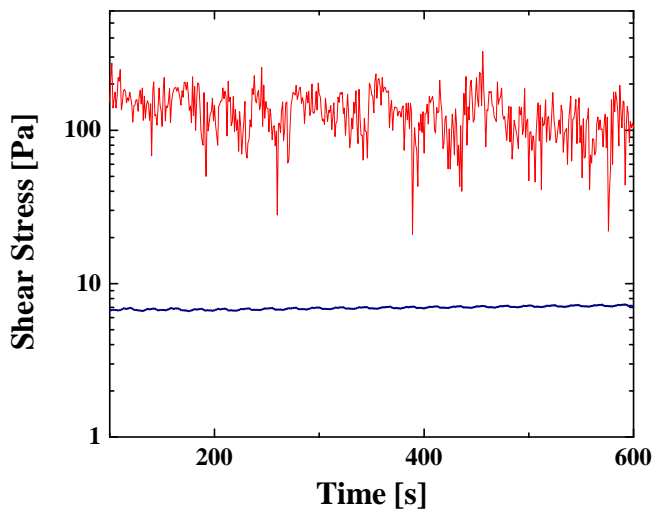


FIGURE 2.8: Plot of shear stress variation for 39% cornstarch suspension with a gap of 1mm at applied shear rates of 1 s^{-1} (blue solid line) and 30 s^{-1} (red solid line).

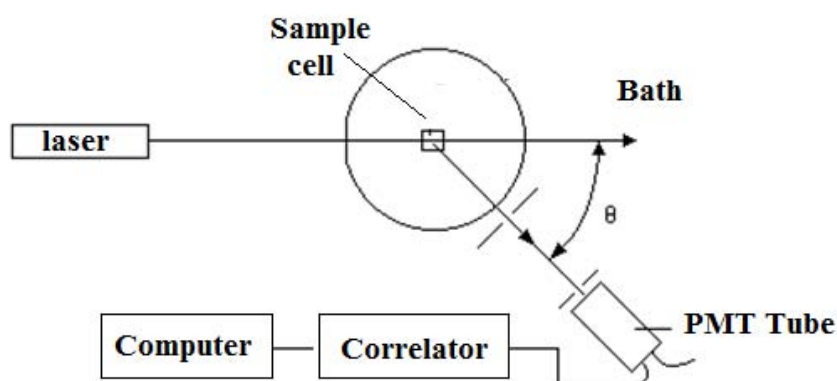


FIGURE 2.9: A schematic diagram of a dynamic light scattering setup.

of the scattered intensity. A typical setup for this DLS measurements is shown in Fig. 2.9. A BIC (Brookhaven Instruments Corporation) BI-200SM spectrometer is used to measure the scattered light intensity at angles between 10° and 150° [3]. A 150 mW solid state laser (Spectra Physics Excelsior) with an emission wavelength of 532 nm is used as a light source. The sample cell is immersed in decalin, a refractive index matching liquid to avoid the scattering from the wall of the sample cell. This decalin container is held in a brass thermostat block. The temperature of the sample cell is controlled between 10°C and 80°C with the help of a temperature controller (Polyscience Digital).

A Brookhaven BI-9000AT digital autocorrelator is used to measure the intensity autocorrelation function of the light scattered from the samples. The Brookhaven BI-9000AT is a digital, high speed processor which can be used as autocorrelator or crosscorrelator, operating in real time with very high efficiency over 10 decades of delay time. The scattered photon pulses are registered in correlator channels, which are separated by linearly or logarithmically spaced delay times. The maximum number of channels, which can be used for calculating the autocorrelation function is 522 [4]. The intensity autocorrelation function $g^{(2)}(\tau)$ is calculated by the digital correlator in the following way [4]:

$$g^{(2)}(\tau) = \frac{1}{N} \sum_{i=1}^N n_i n_{i-j} \quad j = 1, 2, \dots, M$$

where M is number of the correlator channels, n_i is the number of photon pulses in a sampling time or bin time $\Delta\tau$ and N is the number of samples which depends upon sampling time and the measurement time.

DLS data analysis

The intensity autocorrelation function $g^{(2)}(\tau)$ is defined as $g^{(2)}(\tau) = \frac{\langle I(0)I(\tau) \rangle}{\langle I(0) \rangle^2} = 1 + A|g^{(1)}(\tau)|^2$, [5], where $I(\tau)$ is the intensity recorded at time τ , $g^{(1)}(\tau)$ is the normalized electric field autocorrelation function, A is the coherence factor which depends on the detector optics, and the angular brackets $\langle \rangle$ represent an average over time.

For a dilute solution of monodisperse scatterers, $g^{(1)}(\tau) \sim \exp(-\Gamma\tau)$ [5–7], where Γ is the relaxation rate. For a suspension of spheres diffusing in a solvent of refractive index n , $\Gamma = Dq^2$, where D is the translational diffusion coefficient and $q = \frac{4\pi n}{\lambda} \sin(\theta/2)$ is the scattering wave vector at a scattering angle θ and for a wavelength λ . The effective hydrodynamic radius R_H of the scatterer is measured by using the Stokes-Einstein relation $D = k_B T / 6\pi\eta R_H$ [8], where k_B is the Boltzmann constant, T is the temperature and η is the viscosity of the solvent. For suspensions of polydisperse particles, there is a distribution of relaxation rates given by $g^{(1)}(\tau) = \sum_{i=1}^m G_i(\Gamma_i) \exp(-\Gamma_i\tau) = \int_0^\infty G(\Gamma) \exp(-\Gamma\tau) d\Gamma$, where $G_i(\Gamma_i)$ is the contribution to the normalized distribution function of the relaxation rates from the i th scatterer, and \sum indicates a summation over all m scatterers in the scattering volume. If the diffusive relaxation rates Γ are closely spaced, then $g^{(1)}(\tau) \sim \exp(-\Gamma\tau)^\beta$, where $\beta < 1$.

The DLS measurements for a very dilute solution of standard polystyrene spheres at different wavevectors are shown in Fig. 2.10. The polystyrene particles have a diameter of 92 nm and a polydispersity of 3.7% as quoted

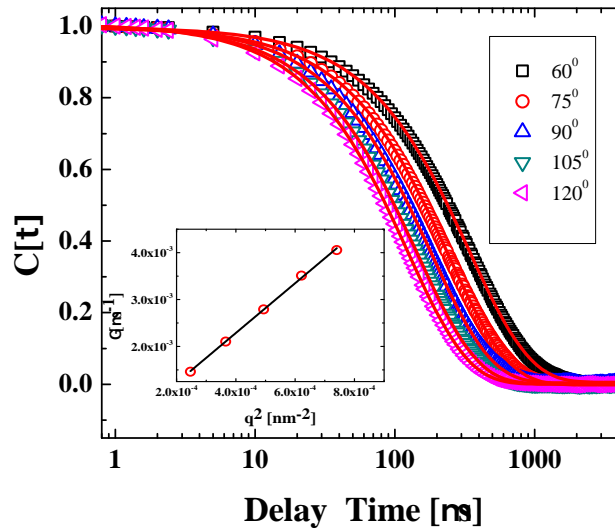


FIGURE 2.10: Plots of the normalized intensity autocorrelation functions $C[\tau]$ vs. delay time τ for the DLS measurements with 92 nm standard polystyrene solution at different scattering angles: 60° (black squares), 75° (red circles), 90° (blue up-triangles), 105° (green down-triangles) and 120° (pink left-triangles). The $C[\tau]$ data all fit to exponential decay functions. In the inset, Γ vs. q^2 is plotted. The slope (solid line) of the linear fit gives the translational diffusion coefficient $D = 6.16 \times 10^{-12} \text{ m}^2\text{s}^{-1}$, which is used to calculate the particle diameter ($a = 91.8 \pm 0.4 \text{ nm}$) using the Stokes-Einstein relation.

by the supplier (Duke Scientific Corporation). The volume fraction ϕ of the polystyrene is kept very low ($\phi \sim 10^{-5}$) to ensure single scattering. Normalized intensity autocorrelation functions [$C[\tau] = g^{(2)}(\tau) - 1$] are plotted in Fig. 2.10 at several scattering angles while varying the delay times. The intensity autocorrelation data fit well to exponential functions of the form $C[\tau] \sim \exp(-\Gamma\tau)$ where Γ is the relaxation time. From the fits, the relaxation rates Γ at all q values are extracted. The inset of Fig. 2.10 shows that Γ varies linearly with q^2 , with $\Gamma \rightarrow 0$ as $q \rightarrow 0$. The slope of the straight line fit to the data gives the translational diffusion coefficient D . This D value gives the diameter of the polystyrene sphere to be $91.8 \pm 0.4 \text{ nm}$, which matches almost exactly with the value supplied by the manufacture.

2.2.3 Cryo-SEM (scanning electron microscopy)

measurements:

The cryo-SEM technique is often used for observing biological substances and allows the preservation and observation of the sample in the hydrated and chemically unmodified state [9]. This technique is also used for the observation of sample phases which are highly dependent on water content. Cryo-SEM is a special type of scanning electron microscopy technique where the sample is kept at cryogenic temperatures. Scanning electron microscopy is a very powerful technique to get images of structures of sizes much smaller than the micrometer scale. The main components of a typical SEM are electron column, scanning system, detector, display, vacuum system and electronics controls (Fig. 2.11) [10]. The electron column of the SEM consists of an electron gun and two or more electromagnetic lenses operating in vacuum. The electron gun generates free electrons. These electrons are accelerated to energies in the range 1-100 keV in the SEM. The purpose of the electromagnetic lenses is to create a small, focused electron probe on the specimen. Typically the electron beam is defined by probe diameter in the range of 1 nm to 1 μm [10]. In order to produce images the electron beam is focused into a fine probe, which is scanned across the surface of the specimen with the help of scanning coils. Each point on the specimen that is struck by the accelerated electrons emits signal in the form of electromagnetic radiation. Selected portions of this radiation, usually secondary (SE) and/or backscattered electrons (BSE), are collected by a detector and the resulting signal is amplified and displayed on a computer monitor [10].

For cryo-SEM experiments, the samples are cryo-fractured by quickly dipping them into liquid nitrogen. The frozen samples are then transferred in vacuum to the cold-stage of SEM cryo-preparation chamber PP3000T cryo unit (Quorum Technologies) and cut with a cold knife. The fractured and cut

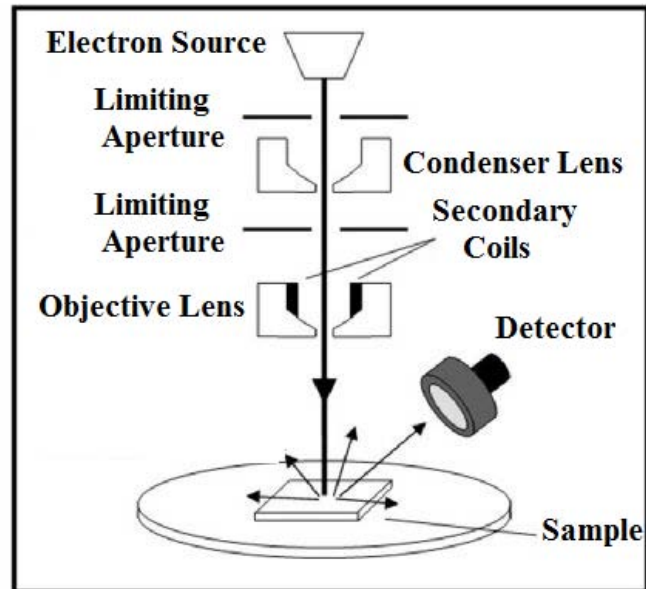


FIGURE 2.11: Schematic diagram of a scanning electron microscopy setup. This is adapted from [10].

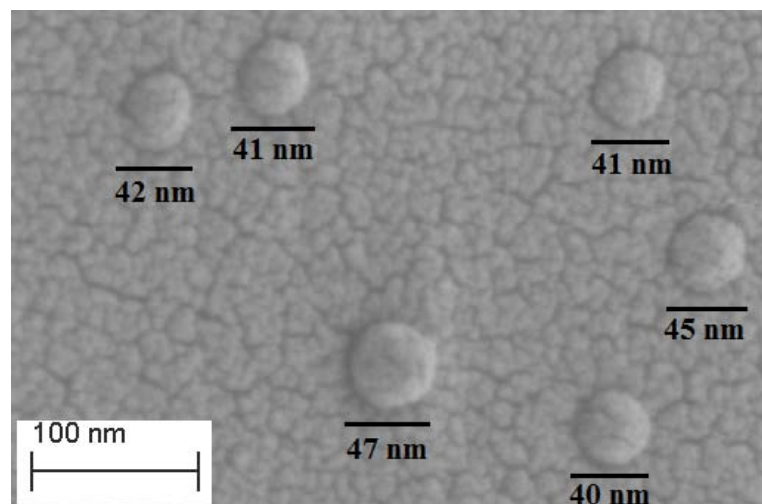


FIGURE 2.12: Cryo-SEM images of standard polystyrene spheres, where the diameters of the spheres are measured to lie in the range of 40-47 nm.

samples are sublimated at -130°C for 5 minutes and then sputtered with platinum for 90 seconds inside the unit. The samples are then transferred to the main chamber of a Zeiss Ultra Plus SEM and the imaging is performed at a temperature of -160°C . Fig. 2.12 shows the images of standard polystyrene spheres of diameters 41 ± 4 nm, which is the value quoted by manufacturer (Thermo Fisher Scientific). From the images, calculation of the diameters of the spheres shows a size range of 40-47 nm.

2.2.4 Fluorescence measurements.

Fluorescence spectroscopy describes the photon emission processes that occur during molecular relaxation from electronic excited states. These photonic processes involve transitions between electronic and vibrational states of polyatomic fluorescent molecules [11, 12]. Electronic states are typically separated by energies of the order of 10000 cm^{-1} . Optical transition due to the incidence of light of appropriate wavelength excites the molecules from the lowest vibrational level of the electronic ground state to an accessible vibrational level in an electronic excited state. After excitation, the molecule quickly relaxes to the lowest vibrational level of the excited electronic state, which is called Stokes shift. This rapid vibrational relaxation process occurs on the time scale of femtoseconds to picoseconds. The fluorescent molecules remain in the lowest vibrational level of the excited electronic state for a period of the order of nanoseconds, the fluorescence lifetime, and then decay to an allowable vibrational level in the electronic ground state resulting in fluorescence emission.

A typical spectrofluorometer includes a light source, a specimen chamber with integrated optical components and high sensitivity detectors. The detailed setup of a typical spectrofluorometer is shown in Fig. 2.13 [13]. The most common light source for fluorometers are lamp sources, such as xenon arc lamps. These lamps provide a relatively uniform intensity over a broad spectral range

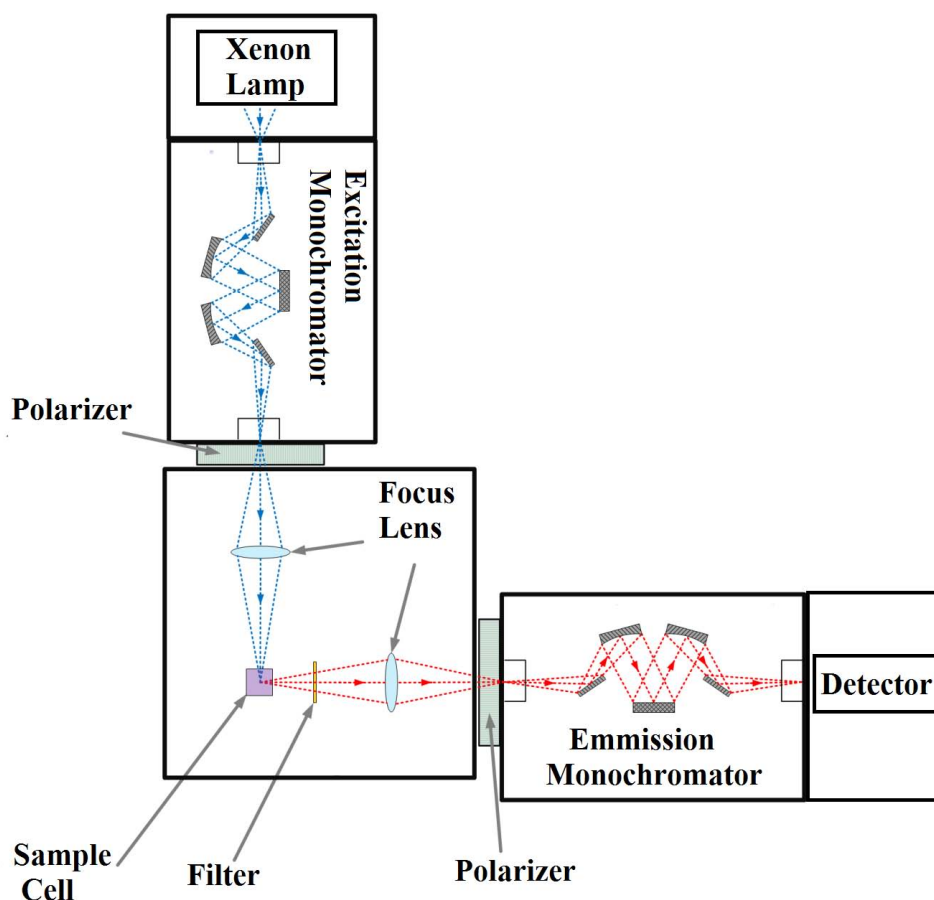


FIGURE 2.13: A schematic diagram of the fluorescence measurement setup. This figure is adapted from [13].

from the ultraviolet to the near infrared. The light shines onto an excitation monochromator, which selects a band of wavelengths. This monochromatic excitation light is directed onto a sample, which emits luminescence. The luminescence is directed into a second emission monochromator, which selects a band of wavelengths, and shines them onto a detector. The optical paths of the excitation and the detection light paths are along the orthogonal axis. The obtained emission spectrum in this experiment is the fluorescent intensity measured as a function of emission wavelength at a constant excitation wavelength.

The spectrofluorometer that we use for the study of the drug encapsulated

micellization process (described in Chapter 4) is a Horiba Jobin Yvon FluoroMax-4 Spectrofluorometer and the corresponding detector is an R928P photomultiplier tube. We use pyrene molecules as the fluorescence probe for our experiments on drug-encapsulated micellar systems. For each fluorescence measurement, 5×10^{-7} M pyrene is added to the drug-encapsulated Pluronic micellar solution. The samples are stirred in an ultrasonicator for sufficient time to encapsulate the pyrene molecules in the micelles. The samples are then kept in quartz cells and excited with light of wavelength 339 nm in the spectrofluorometer and the emission spectrum is measured using a photomultiplier tube.

2.2.5 Small angle X-ray scattering (SAXS).

The small angle X-ray scattering (SAXS) technique is widely used in soft matter systems to get information about different macromolecular phases like micelles, lamellar phases of amphiphilic molecules, protein solutions etc. According to Bragg, the position of X-ray peaks follow the following relation [14]:

$$2d\sin\theta = n\lambda$$

where d is the spacing between the lattice planes and λ is the incident wavelength of the radiation from an X-ray source. The scattered X-ray is captured by a detector and the data is analyzed (Fig. 2.14). Most often, normal X-ray diffraction data for large scattering angles θ is used to extract information about crystalline structures of the order of angstroms. When the scattering angles are very small ($\theta < 3^\circ$), SAXS measurements are performed to elucidate much bigger structures, of the order of 1-100 nm. The schematic diagram of the SAXS setup is shown in Fig. 2.14 [15]. For our experiment, SAXS measurements are performed using a Hecus S3-Micro System using a Cu K_α ($\lambda =$

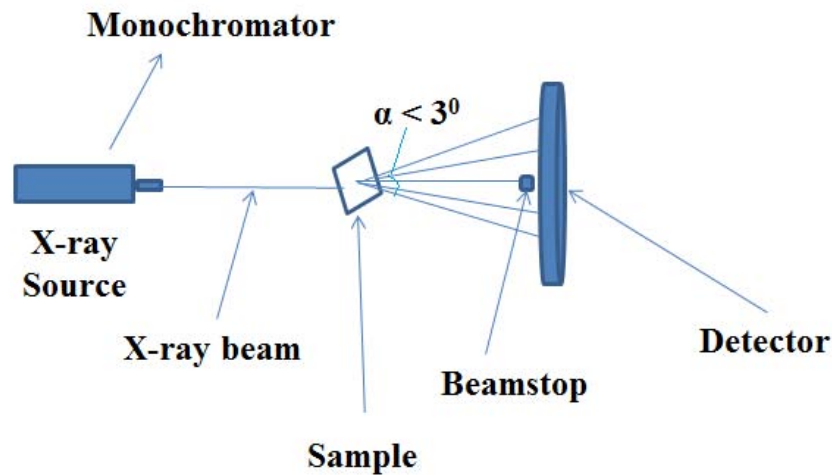


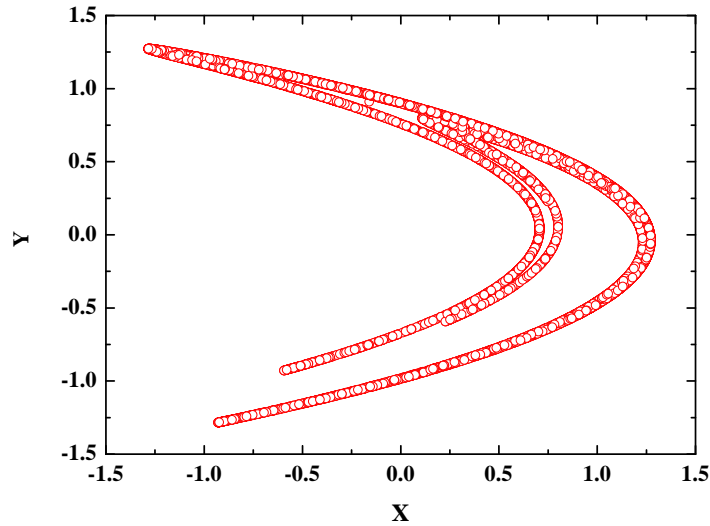
FIGURE 2.14: Experimental set up of SAXS measurements.

1.54 angstrom). The scattered intensity is measured with a one-dimensional position sensitive detector (PSD). The X-ray diffraction studies are carried out on samples loaded in 1 mm diameter glass capillaries.

2.3 Data Analysis:

2.3.1 Analysis of observed chaotic data:

In this section, we describe some standard nonlinear time-series analysis techniques employed to analyze chaotic time series. The purpose of nonlinear time-series analysis is the calculation of certain invariants to understand whether the apparently irregular time evolution of experimentally measurable physical parameters is due to deterministic chaos or random noise. In our rheological measurements, stress fluctuation data is obtained during the experiments which could be generated due to rheological chaos. The observed stress fluctuation data is analyzed to extract signatures of chaotic dynamics. The two

FIGURE 2.15: Hénon map for $a = 2$, $b = 0$.

main dynamical invariants, calculated from our experimental data to characterize possible chaotic dynamics, are correlation dimension and Lyapunov exponent. The calculation protocol of these invariants is described below by using the example of the Hénon map. The dynamical equations of the Hénon time series are [21]:

$$x_{n+1} = y_n + 1 - ax_n^2$$

$$y_{n+1} = bx_n$$

The plot of the Hénon map for $a = 2$ and $b = 0$ is shown in Fig. 2.15.

Correlation dimension calculation

Chaotic dynamics are characterized by the presence of an attractor. A correlation dimension gives us an idea of the geometry of the attractor in phase space. The attractor is usually a low dimensional subset of the phase space, to which the initial non-zero phase space converges asymptotically with the

advancement of time. A numerically simple and widely used method to calculate correlation dimension is described by Grassberger and Procaccia [16]. According to this method, for a given time series $T_i = T(i\Delta t)$ with $i = 1$ to N with a regular interval Δt , an m dimensional vector $X_j = (T_j, T_{j+L}, T_{j+2L}, \dots, T_{j+(m-1)L})$ with $j = 1$ to $N-(m-1)L$ is constructed. Here, m is the embedding dimension and L is the delay time. The vector X_j defines a trajectory in an m dimensional phase space in such a way that the original time series can be described by the following dynamics $F: X_j \rightarrow X_{j+1}$. The delay time L is calculated from the time when the correlation function of the time series T_i decays to $1/e$ of its initial value. According to the algorithm of Kennel *et al.*, one can estimate the embedding dimension by calculating the number of false nearest neighbors around the data point [18]. At the optimum embedding dimension m , the number of the false nearest neighbors decreases to approximately 0. Next, we calculate the correlation integral $C(R)$ as a function of distance R in m dimensional phase space. $C(R)$ gives the number of point pairs separated by a distance less than R and is calculated by the following method:

$$C(R) = \frac{1}{N^2} \sum_{j,i+1}^N H(R - |X_j - X_i|)$$

where H is the Heaviside functions, whose values are 0 for negative arguments and 1 for positive arguments, and $|X_j - X_i|$ is the distance between the i th and j th points in the m dimensional phase space. For low values of R , $C(R)$ is found to follow a power law with R in the form of $C(R) = R^v$, where v is called the correlation dimension [16]. A plateau in the plot of v vs. $\log(R)$ gives the correct value of correlation dimension for an embedding dimension m . If we take a large enough embedding dimension m ($= m_0$), then the correlation dimension v will saturate to v_0 . If the given time series data owes its origin to chaotic dynamics, $v_0 \leq m_0$ [16].

The above recipe is used to calculate the correlation dimension for the

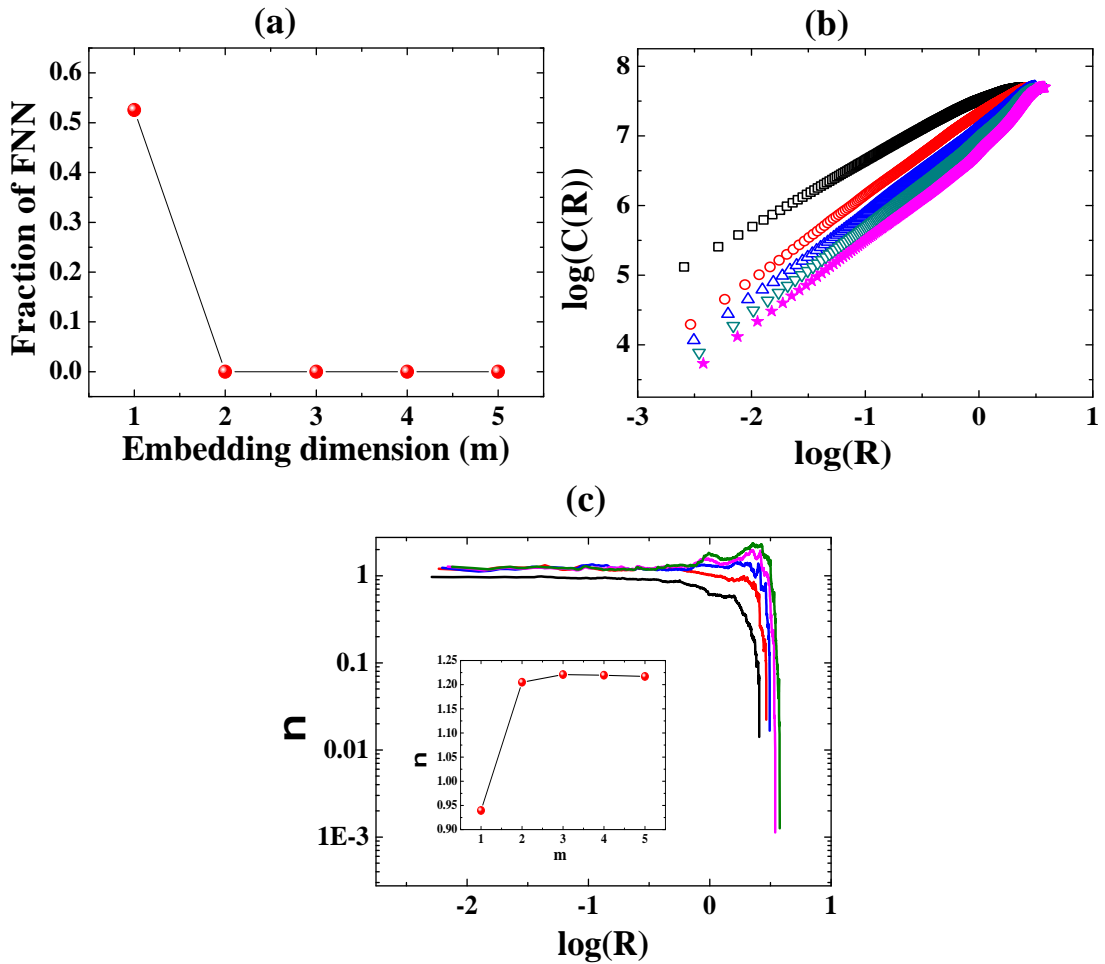


FIGURE 2.16: A plot of the fraction of false nearest neighbors (FNN) vs. embedding dimension m for henon map is shown in 2.16(a). The plots of $\log(C(R))$ vs. $\log(R)$ are shown in 2.16(b) for different dimensions: $m=1$ (black square), $m=2$ (red circle), $m=3$ (blue uptriangle), $m=4$ (pink downtriangle) and $m=5$ (green star). From this plot, the corresponding correlation dimension ν vs. $\log(R)$ is plotted for $m=1$ (black line), $m=2$ (red line), $m=3$ (blue line), $m=4$ (pink line) and $m=5$ (green line)) in 2.16(c). In the inset of 2.16(c), correlation dimension ν vs. embedding dimension m is plotted. It is seen that the embedding dimension $m_0=2$ and the correlation dimension $\nu_0=1.25$ for this map.

Hénon map. We first calculate the false nearest neighbors around the data point for different embedding dimensions and plot the fraction of false nearest neighbors (FNN) vs. embedding dimension m in Fig. 2.16(a). From this plot, we estimate that the optimum embedding dimension for Hénon map is 2. Then we calculate the correlation integral $C(R)$ and plot $\log(C(R))$ vs. $\log(R)$ in Fig. 2.16(b). From the slope of $\log(C(R))$ vs. $\log(R)$ plot, we calculate the correlation dimension ν as a function of distance R for different embedding dimensions m (shown in Fig. 2.16(c)). The plateau value of ν (ν_0) gives the correct value of correlation dimension for an embedding dimension m . Fig. 2.16(c) shows a plot of correlation dimensions ν vs. $\log(R)$ for $m = 1-5$. The value of ν , obtained from the plateau in the ν vs. $\log(R)$ plot, is found to saturate to a value of $\nu_0 = 1.25$ for embedding dimensions $m \geq 2$. This satisfies the criterion of chaos and the value of ν_0 perfectly matches with the reported value for the Hénon map [16].

Lyapunov exponent calculation:

One of the most significant features of deterministic chaotic data is the existence of a positive Lyapunov exponent. A positive Lyapunov exponent suggests that the Euclidean distance between two neighboring data points diverges exponentially with time. This is a characteristic of deterministic chaos.

In this work, Lyapunov exponent is calculated using the TISEAN (Time series analysis) [17] software package which uses the method proposed by Rosenstein *et al.* to calculate the maximum Lyapunov exponent [19]. For this calculation, we first calculate the Euclidean distance $d_{ij}(K)$ between two vectors in an m dimensional space for different numbers of iterations K using the formula $d_{ij}(K) = \left| \vec{X}_i - \vec{X}_j \right|$ [20]. We plot $\Lambda = \langle \ln d_{ij}(K) / d_{ij}(0) \rangle$ as a function of K . The slope of the linear fit to the data gives the Lyapunov exponent λ .

We calculate the maximum Lyapunov exponent of the Hénon map using the method used by Rosenstein *et al.* (described earlier). Λ vs. K for the Hénon

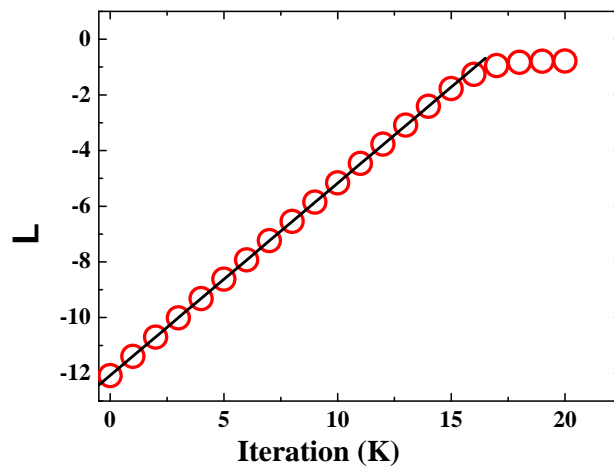


FIGURE 2.17: Plot of Λ vs. K for the Hénon map. Slope of the plot gives the maximum Lyapunov exponent for the Hénon map for $m=2$.

map is plotted in Fig 2.17. Slope of the plot gives the maximum Lyapunov exponent for the Hénon map to be around 0.69.

References

- [1] Anton Paar MCR 501 rheometer users manual.
- [2] C. W. Macosko, Rheology: Principles, Measurements and Applications, (VCH Publishers, New York, 1993).
- [3] BI-200SM Goniometer manual, Brookhaven Instruments Corporation.
- [4] Bi-9000AT manual, Brookhaven Instruments Corporation.
- [5] B. J. Berne and R. Pecora, Dynamic Light Scattering: With Applications to Chemistry, Biology, and Physics, (Wiley-Interscience, New York, 1976).
- [6] R. Pecora, Dynamic Light Scattering: Applications of Photon Correlation Spectroscopy, (Plenum, New York, 1985).
- [7] B. Chu, Laser Light Scattering: Basic Principles and Practice, (Academic, New York, 1974).
- [8] A. Einstein, A, Investigations on the Theory of Brownian Movement, edited by R. Furth, (Dover, New York, 1956).
- [9] S. Craig and C. D. Beaton, J. Microscopy, **182**, 102 (1996).
- [10] Carl Zeiss Ultra Plus SEM manual.

- [11] J. R. Lakowicz, Principles of Fluorescence Spectroscopy, (Plenum, New York, 1999).
- [12] R. S. Becker, Theory and Interpretation of Fluorescence and Phosphorescence, (Wiley, New York, 1969).
- [13] Horiba Jobin Yvon FluoroMax-4 Spectrofluorometer operation manual.
- [14] B.D. Cullity, Elements of X-ray Diffraction (Prentice Hall, New Jersey, 2001).
- [15] Hecus X-Ray Systems manual.
- [16] P. Grassberger and I. Procaccia, Phys. Rev. Lett. **50**, 346-349 (1983).
- [17] The TISEAN package is written by R. Hegger, H. Kantz and T. Schreiber. (downloaded from <http://www.mpipks-dresden.mpg.de/tisean>).
- [18] M. B. Kennel, R. Brown and H. D. I. Abarbanel, Phys. Rev. A **45**, 3403 (1992).
- [19] M. T. Rosenstein, J. J. Collins and C. J. D. Luca, Physica D **65**, 117 (1993).
- [20] J. Gao and Z. Zheng, Phys. Rev. E **49**, 3807 (1994).
- [21] M. Henon, Communications in Mathematical Physics **50**, 69 (1976).

3

Jamming Behavior of Triblock Copolymer Solutions and Triblock Copolymer-Anionic Surfactant Mixtures

3.1 Introduction

A wide variety of systems, including polymer solutions, granular media, colloidal suspensions and molecular systems, exhibit the jamming phenomenon, which is characterized by a sudden arrest of their dynamics and the emergence of an elastic response [1–3]. This is discussed in Chapter 1. According to the

universal jamming phase diagram proposed by Liu *et al.* [1], an unjammed system can undergo a transition to a jammed state when its concentration is increased. It is known that at high volume fractions, micelle forming triblock copolymer solutions of Pluronic, of the type $\text{PEO}_x\text{PPO}_y\text{PEO}_x$ (PEO: polyethylene oxide and PPO: polypropylene oxide), that are typically identified by the generic name Pluronic, can enter a solid-like phase that is characterized by very large values of the elastic modulus and very slow dynamics, features that are typically associated with soft glasses [4]. There have been extensive theoretical and experimental studies to understand the soft glassy rheology of materials as diverse as foams, pastes, emulsions and colloidal suspensions [5–9]. Solid-like mesophases of block copolymers exhibit low yield stresses, very high zero shear viscosities ($\sim 10^6$ Pa.s) and shear-thinning. Lobry *et al.* describe the observed behavior as a gelation process involving a percolation transition between a micellar liquid phase and a solid phase [10]. In contrast, Castelletto *et al.* attribute the solidity of the sample to the coexistence of a close-packed crystal with a fluid [11]. It is now well-known that in the case of Pluronics of varying chain lengths, the sequence of phase transitions normally remains the same with increasing concentration, while the relative extents of the phases depend upon the details of the copolymer architecture [12].

Block copolymers find important uses in diverse industrial and technical applications and as novel agents in drug and gene delivery [13]. In the work described in this chapter, rheological measurements are combined with dynamic light scattering (DLS) experiments to relate the mechanical response of Pluronic samples to the microscopic dynamics of the constituent aggregates. Above a certain copolymer concentration, pure F127 solutions have very high viscosities ($\sim 10^5$ - 10^6 Pa.s) and can be characterized as soft glasses. In a recent publication, our group established the presence of soft glassy rheology in Pluronic F108 ($\text{PEO}_{127}\text{PPO}_{48}\text{PEO}_{127}$) solutions, estimated the characteristic relaxation times of the samples and isolated a coexistence of glassy and

fluid-like regimes in a temperature-copolymer concentration phase diagram [4]. One of the aims of this work was to show that the emergence of soft glassy rheology in triblock copolymer solutions was accompanied by a slowing down of the slow relaxation mode of the sample, similar to the results reported in [15, 27] for concentrated, nonaqueous suspensions of sterically stabilized colloidal spheres.

Recent experiments have studied the aggregation of Pluronic micelles in the presence of the drug Ibuprofen [16]. An understanding of the interaction between polymers and surfactants is important due to the wide use of polymer-surfactant mixtures in the manufacture of paints, detergents, cosmetics and pharmaceuticals [17, 18]. The association of additives with Pluronic molecules is therefore a very interesting topic and has been studied in detail in the literature [19–22]. Recent studies find that when the anionic surfactant SDS (sodium dodecyl sulfate) is added to Pluronic solutions, the micellar gel structure is altered considerably, and the observed structural changes are strongly dependent on the length ratios of the PPO and PEO blocks of the Pluronic sample, the concentrations of Pluronic and SDS and the sample temperature. Hecht *et al.* show that for F127 (PEO₇₀PPO₁₀₀PEO₇₀) solutions, the addition of SDS can completely suppress the micellization of Pluronic by destroying the gel phase formed in pure Pluronic micellar solutions [23], while for P123 (PEO₂₁PPO₆₇PEO₂₁) solutions, the addition of SDS initially enhances the stability of the gel phase before completely destroying this phase at very high SDS concentrations [24]. It is now well-established that the addition of SDS causes the hydrophobic tail (DS⁻) of the surfactant to bind to the hydrophobic core of the Pluronic micelles [18]. The resulting intra-aggregate repulsion causes the breakup of the aggregates into smaller mixed micelles. The formation of such Pluronic-SDS mixed micelles has been studied in detail using calorimetry [22, 25, 26], light scattering [17, 22, 26, 27], electromotive force measurements

[22, 25] and rheology [27, 28]. To investigate the effects of an anionic surfactant additive (SDS) on the micellar packing in F127 solutions, the rheological properties of F127-SDS mixtures are studied here by varying the concentration of SDS over a very wide range (the mole ratio $[\text{SDS}]/[\text{F127}]$ is varied between 0 and 35). It is argued here that the shape anisotropy and the size polydispersity of the constituents of F127-SDS mixtures give rise to dramatic changes in the packing behavior of the micelles, resulting in micellar unjamming and our observation of the disappearance of soft glassy rheology in these samples. This unjamming process causes the complex moduli of the sample to decrease by almost six orders of magnitude in the SDS concentration range studied. This is consistent with our DLS data which shows a speeding up of the relaxation dynamics in F127-SDS mixtures.

3.2 Sample preparation

To prepare pure F127 solutions, appropriate amounts of F127 are dissolved in deionized and distilled Millipore water (measured resistivity: $18.2 \text{ M}\Omega\text{-cm}$) under vigorous stirring conditions. To prepare F127-SDS mixtures, appropriate amounts of SDS are dissolved in deionized and distilled Millipore water. Next, F127 is slowly added to the solution and the mixture is stirred in a magnetic stirrer. Each sample is homogenized by storing it overnight at 5°C , which is well below the critical micellization temperature of F127. The concentration of F127 in all the F127-SDS mixtures is kept constant at 0.25 g/cc (19.8 mM).

3.3 Results

We study the evolution of the mechanical modulus of the F127 solutions with increase in sample concentration and relate this data to the change in the microscopic dynamics of the sample. Fig. 3.1 plots the magnitude of the complex modulus $|G^*|$ (black circles) of F127 solutions vs. F127 concentration. $|G^*|$ is defined as $|G^*| = (G'^2 + G''^2)^{1/2}$ [29], where G' and G'' are the elastic (storage)

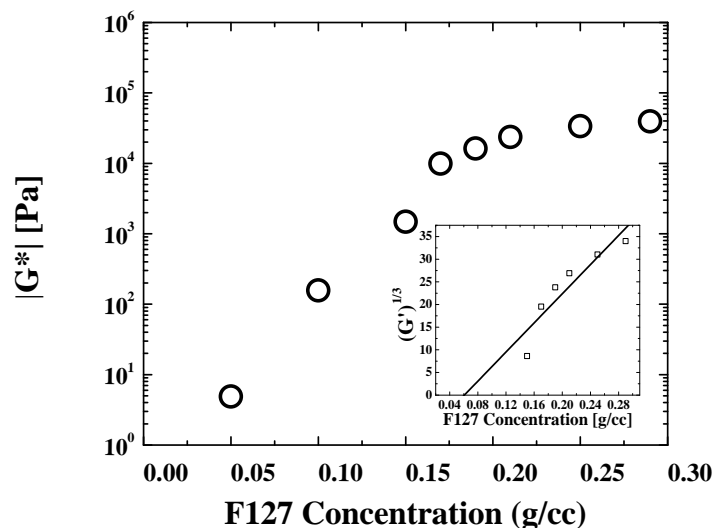


FIGURE 3.1: The magnitude of the complex modulus $|G^*|$ (\circ) at $T = 40^\circ\text{C}$ with increasing F127 concentration. Inset shows the plot of $G'^{1/3}$ vs. F127 concentration. A straight line fit to the data intersects the x axis at $c_{gel} = 0.06$ g/cc.

and viscous (loss) moduli respectively at an angular frequency $\omega = 1$ rad/s, acquired in oscillatory rheology experiments performed at small strain amplitudes $\gamma = 0.5\%$ at 40°C . It can be seen from Fig. 1 that $|G^*|$ shows a monotonic increase with F127 concentration, similar to the results in [30]. At the lowest concentration of F127 (0.05 g/cc), $|G^*| \approx 5$ Pa. When the concentration of F127 is increased to 0.20 g/cc, $|G^*|$ increases by 4 decades ($\approx 5 \times 10^4$ Pa). Similar to the work on near critical polymer gels reported in [31], a straight line fit to a plot of $G'^{1/3}$ vs. F127 concentration (inset of Fig. 3.1) intersects the $G'^{1/3} = 0$ axis at $c_{gel} \approx 0.06$ g/cc, which gives a reasonable estimate for the gelation concentration threshold of F127 micellar solution.

Oscillatory frequency sweep measurements for F127 solutions of different concentrations are performed at $T = 40^\circ\text{C}$ by decreasing the angular frequency ω logarithmically from 100 rad/s to 0.1 rad/s while keeping the strain amplitude fixed at 0.5%. For the samples of higher concentrations (data for 0.25 g/cc F127 solution is denoted by solid symbols in Fig. 3.2), the elastic modulus G' (denoted by red squares) is almost independent of ω , the viscous modulus

3. JAMMING BEHAVIOR OF TRIBLOCK COPOLYMER SOLUTIONS AND TRIBLOCK COPOLYMER-ANIONIC SURFACTANT MIXTURES

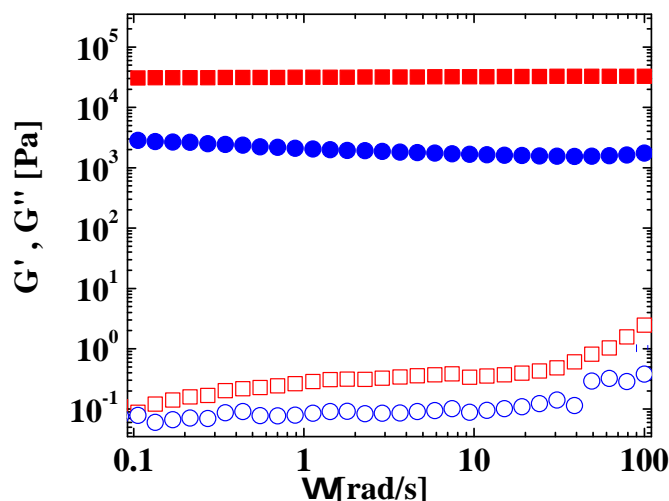


FIGURE 3.2: The figure plots the frequency responses at 40°C for F127 solutions of concentration (a) 0.05 g/cc (hollow symbols) and (b) 0.25 g/cc (solid symbols). The squares denote G' and the circles denote G'' .

G'' (denoted by blue circles) is weakly dependent on frequency, and $G' \gg G''$ over the entire frequency range. These are typical signatures of jammed soft solids [4, 7, 8] and indicate the presence of a crowded micellar environment in this F127 sample. Previous small angle neutron scattering experiments have demonstrated that the aggregation number of F127 micelles is independent of concentration and temperature above the critical micellization temperature [32]. The increased overlap of the PEO chains [10] in concentrated F127 solutions therefore results in micellar jamming and compaction and the large magnitudes of the characteristic moduli. In contrast to the high-concentration regime, the magnitudes of G' and G'' (hollow squares and circles respectively in Fig. 3.2) are significantly lower in the dilute samples and indicates the absence of a predominantly solid-like response in this concentration regime.

Systematic DLS experiments are next performed to study the relaxation processes of F127 solutions in different concentration regimes. To take care of sample non-ergodicity, the method proposed by van Meegen and Pusey [15] is employed to measure the intensity autocorrelation functions of the scattered

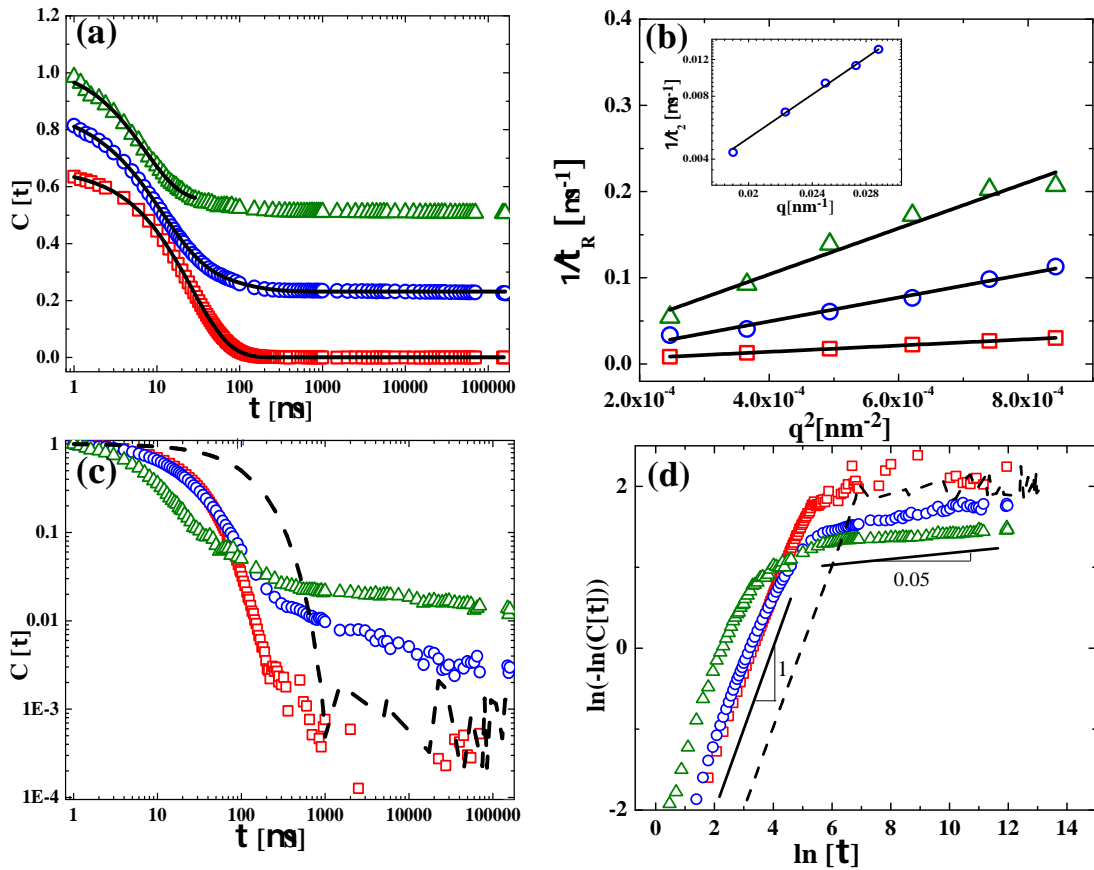


FIGURE 3.3: DLS data for F127 solutions of concentrations 0.05 g/cc (□), 0.10 g/cc (○) and 0.25 g/cc (△). 3.3(a) shows the plots of the intensity autocorrelation functions $C[\tau]$ on a linear-logarithmic scale at $T = 40^\circ\text{C}$, acquired at $\theta = 90^\circ$ (data sets are shifted vertically for better visibility). Fits to this data, whose functional forms are discussed in the text, are shown by solid lines. 3.3(b) shows the linear fits to $1/\tau_R$ vs. q^2 for all three samples. Inset of 3.3(b) shows a power law fit with exponent 3 to $1/\tau_2$ vs. q on a logarithmic-logarithmic scale. 3.3(c) shows the plots of the normalized intensity autocorrelation functions $C[\tau]$ vs. τ on a logarithmic-logarithmic scale. The dashed line in 3.3(c) corresponds to the autocorrelation plot for a dilute aqueous solution of freely diffusing polystyrene colloidal spheres of size 95 nm at $T = 40^\circ\text{C}$ and $\theta = 90^\circ$. The data of Fig. 3.3(c) is recast in 3.3(d), where $\ln(-\ln(C[\tau]))$ is plotted vs. $\ln[\tau]$.

light. The unnormalized time-averaged intensity autocorrelation functions are measured for six different scattering volumes obtained by rotation and vertical translation of the sample cell. The intensity autocorrelation functions acquired using this protocol are added and then normalized. Ensemble averaged autocorrelation functions are acquired at six different scattering angles. For a pure F127 sample of concentration 0.05 g/cc (the low viscosity regime), the intensity autocorrelation function $C[\tau] = g^{(2)}(\tau) - 1$ is plotted vs. the delay time τ at $T = 40^\circ\text{C}$ and scattering angle $\theta = 90^\circ$ (red squares) in Fig. 3.3(a). The solid line fit to this data is $C[\tau] \sim \exp(-\frac{\tau}{\tau_R})^\beta$, where the stretching exponent $0.9 < \beta < 0.95$ indicates the presence of an approximately single relaxation rate. Fig. 3.3(b) shows that $1/\tau_R$ (denoted by red squares) varies linearly with q^2 with $1/\langle \tau_R \rangle \rightarrow 0$ as $q \rightarrow 0$, which confirms the diffusive nature of the micellar relaxation in the dilute regime.

As the concentration of F127 is increased, the intensity autocorrelation functions do not show stretched exponential decays, but can instead be described as two-step relaxation processes. Fig. 3.3(a) also shows the intensity autocorrelation plot for a sample in the semi-dilute viscosity regime (0.10 g/cc F127 solution, denoted by blue circles) at $\theta = 90^\circ$ and $T = 40^\circ\text{C}$. This autocorrelation data is fitted to the form $C[\tau] = (A \exp(-\tau/\tau_R) + B \exp(-(\tau/\tau_2)^\beta))^2$. The values of τ_R (relaxation time for the fast exponential decay) and τ_2 (relaxation time for the slow stretched exponential process) are estimated for six different wavevectors. Fig. 3.3(b) shows the plot of $1/\tau_R$ (denoted by blue circles) vs. q^2 . This data fit to a straight line with $1/\langle \tau_R \rangle \rightarrow 0$ as $q \rightarrow 0$, indicating that the fast relaxation of the micelles in the semi-dilute regime is diffusive. The slower stretched exponential relaxation process yields a non-diffusive relaxation time (τ_2) that is approximately 10 times slower than τ_R . τ_2 has an approximately q^{-3} dependence (shown in the inset of Fig. 3.3(b)) and can be attributed to intraparticle dynamics arising out of large scale sample heterogeneities/ clusters [33].

As the F127 concentration is further increased, the overlapping of the PEO coronas increase and the close-packed micelles undergo a jamming transition due to the constraints imposed upon their motion. The micelles are now trapped in cages formed by their neighbors and structural relaxation by micellar rearrangements becomes less probable. At F127 concentrations ≥ 0.15 g/cc, the system enters an elastic soft solid phase characterized by $G' \gg G''$. The fluctuations in the intensity of the light scattered by these samples become so slow that a full decay of $C[\tau]$ to zero (or to instrumental noise level) is not possible within the experimental time window. To highlight the non-ergodic nature of the relaxation at high sample concentrations, the normalized intensity autocorrelation function $C[\tau]$ is plotted vs. the delay time τ on a logarithmic-logarithmic scale in Fig. 3.3(c). Fig. 3.3(c) also shows the intensity autocorrelation data for freely diffusing 95 nm polystyrene (PS) spheres in an aqueous solution (volume fraction $\phi \sim 10^{-5}$; shown by dashed line). After an initial exponential decay, the $C[\tau]$ plot for the freely diffusing PS spheres decays to 10^{-3} - 10^{-4} at $\tau \approx 1000 \mu\text{s}$ which defines the instrumental noise level for our experiments. For the dilute unjammed F127 sample of concentration 0.05 g/cc (squares in Fig. 3.3(c)), $C[\tau]$ decays to the experimental noise level in $\tau \sim 1000\mu\text{s}$, verifying that the dynamics in the dilute concentration regime is ergodic. From the rheological data for the F127 solution of concentration 0.05 g/cc (hollow symbols in Fig. 3.2), we observe that $G' \geq G''$, which indicates a weak gel. However, the DLS data for the same sample (Fig. 3.3) shows a complete decay of $C[\tau]$, confirming fluid like mobility of the micelles. We believe that this discrepancy arises because rheology and DLS experiments probe very different length scales [34].

For the soft solid-like sample (0.25 g/cc F127, green triangles in Fig. 3.3(c)), it is seen that $C[\tau]$ does not decay to the noise level within our experimental time window. This indicates a slowing down of the dynamics of the sample and is a signature of a jammed micellar environment. The data of Fig. 3.3(c) is

recast in Fig. 3.3(d), where $\ln(-\ln(C[\tau]))$ is plotted vs. $\ln[\tau]$ for the same samples. Similar to the PS suspension data (dashed lines), the data for the 0.05 g/cc sample (squares) is a straight line of slope $\beta = 1$ at $\ln[\tau] \leq 5$ followed by a noisy plateau at $\ln(-\ln(C[\tau])) \sim 2$, which corresponds to $C[\tau] \approx 10^{-3.5}$ (noise level defined in Fig. 3.3(c)). The data for the 0.10 g/cc and 0.25 g/cc samples (blue circles and green triangles respectively), are characterized by two components, a faster straight line component which extends upto $2 \leq \ln[\tau] \leq 4$ with a slope of 1. This indicates a mono-exponential faster relaxation process and is followed by a slower straight line component of significantly smaller slope. The systematic decrease in the magnitudes of $\ln(-\ln(C[\tau]))$ and the decreasing slopes of the straight lines characterizing the slow components on increasing F127 concentration is a clear indication of the slowing down of the sample dynamics.

In Fig. 3.3(a), the faster decay of the autocorrelation function for the 0.25 g/cc sample (green triangles) is fitted to an exponential form $C[\tau] \sim \exp(-\frac{\tau}{\tau_R})$. The relaxation process associated with this exponential decay is diffusive as $1/\tau_R$ varies linearly with q^2 with $1/\langle \tau_R \rangle \rightarrow 0$ as $q \rightarrow 0$ (green triangles in Fig. 3.3(b)). In the soft solid phase, the micellar aggregates are closely packed and the interaction between aggregates is very strong [35]. The diffusive fast relaxation process is attributed to the constrained diffusion of the confined F127 micelles.

Next, F127-SDS mixtures are prepared to study the effects of the addition of the anionic surfactant SDS to the soft solid-like phase formed by concentrated F127 solutions. Fig. 3.4 plots the magnitudes of the complex moduli $|G^*|$ (denoted by red circles) of F127-SDS mixtures (concentration of F127 fixed at 0.25 g/cc, SDS concentration is varied in the range 0-700 mM) at 40°C, acquired in oscillatory rheology experiments ($\gamma = 0.5\%$ and $\omega = 1$ rad/s). As demonstrated earlier, the 0.25 g/cc F127 system is a jammed, soft solid. F127-SDS mixtures exhibit very high magnitudes of the complex moduli $|G^*|$ when

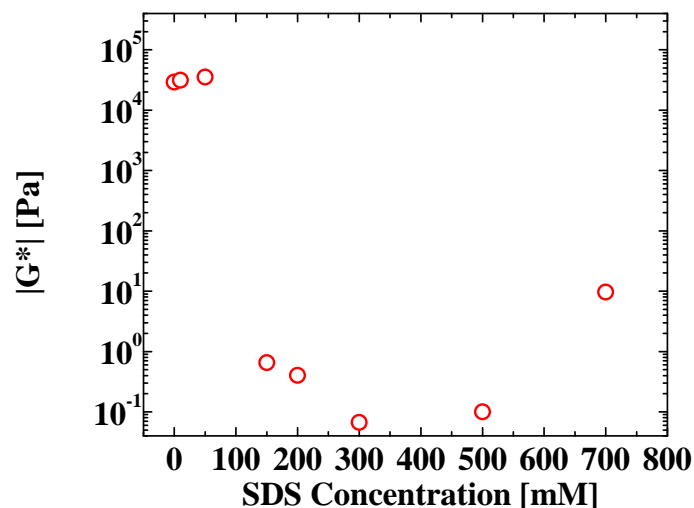


FIGURE 3.4: The magnitude of the complex modulus $|G^*|$ (\circ) of F127-SDS mixtures (concentration of F127 fixed at 0.25 g/cc) at $T = 40^\circ\text{C}$ with increasing SDS concentration.

SDS concentration ≤ 50 mM. For higher concentrations of SDS (~ 150 -500 mM), $|G^*|$ decreases by six orders of magnitude. The non-monotonic dependence of $|G^*|$ on SDS concentration at higher SDS concentrations (> 150 mM) arises due to the complex dependence of the mechanical moduli on the different aggregates present in the mixtures.

To further characterize the mechanical responses of the mixtures, G' and G'' are measured while performing strain amplitude sweep measurements at $T = 40^\circ\text{C}$. These experiments are performed by ramping up the amplitude of the oscillatory strain γ at a fixed angular frequency $\omega = 1$ rad/s. The results are displayed in Fig. 3.5. For the pure F127 solution (denoted by red squares in Fig. 3.5), G' (filled red squares) stays almost constant at the lower strain amplitudes, followed by a power law decrease at strain amplitudes $\gamma > 1\%$. G'' (hollow red squares) is significantly lower than G' and shows a peak at $\gamma \sim 2\%$, followed by a power law decay. These features ($G' \gg G''$ at low strains, a peak in G'' at a characteristic strain, and power law decays of both moduli at higher strains such that $G'' > G'$ for very high strains) are typical features of

3. JAMMING BEHAVIOR OF TRIBLOCK COPOLYMER SOLUTIONS AND TRIBLOCK COPOLYMER-ANIONIC SURFACTANT MIXTURES

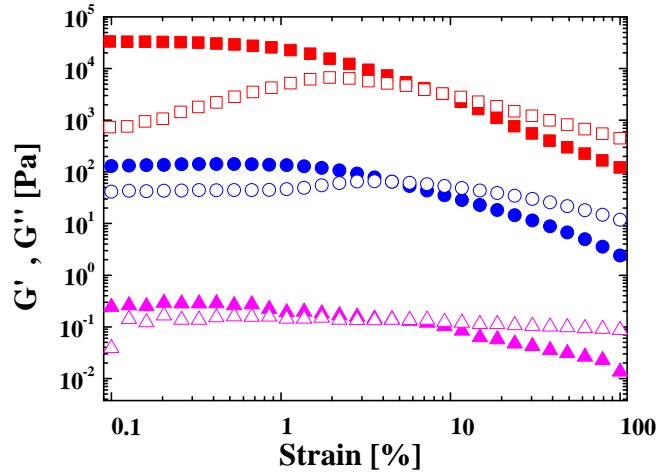


FIGURE 3.5: Oscillatory amplitude sweep data for a pure F127 sample (\square) and for F127-SDS mixtures with SDS concentrations 150 mM (\circ) and 700 mM (\triangle) at $T = 40^\circ\text{C}$. The F127 concentration is fixed at 0.25 g/cc. The solid symbols denote G' and the hollow symbols denote G'' .

soft solids [5, 7–9]. With increasing SDS concentration, G' and G'' decrease significantly, the magnitude of G' approaches that of G'' and the peak in G' eventually disappears, signaling the gradual disappearance of soft glassy rheology and the onset of sample unjamming. For the mixture with 700 mM SDS, this is clearly indicated by the very weak strain dependence of G' and G'' (magenta triangles in Fig. 3.5) and the observation that $G' \approx G''$ for $\gamma < 10\%$.

The microscopic relaxation processes contributing to the unjamming of F127-SDS mixtures are studied by performing DLS experiments. In Fig. 3.6(a), the normalized intensity autocorrelation function $C[\tau]$ is plotted vs. the delay time τ at $\theta = 90^\circ$ and $T = 40^\circ\text{C}$ for a pure F127 solution (denoted by red squares) and for F127-SDS mixtures with SDS concentrations 10 mM (blue circles), 300 mM (magenta up triangles) and 500 mM (green down triangles) respectively. The DLS plot for freely diffusing 95 nm PS spheres in water is also incorporated as a reference process that exhibits a complete decay to the experimental noise level (shown by dashed line). The $C[\tau]$ plots for the jammed

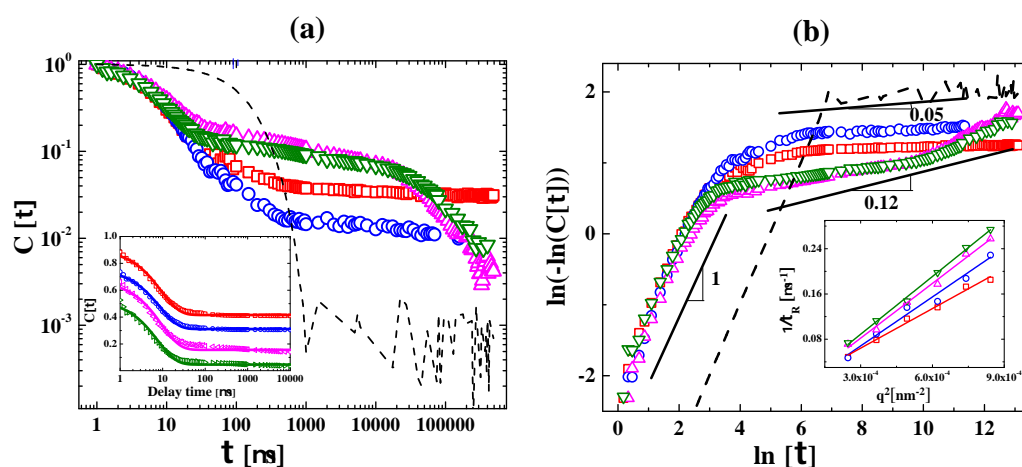


FIGURE 3.6: In (a), the normalized intensity autocorrelation functions $C[\tau]$ are plotted on a logarithmic-logarithmic scale for a pure F127 sample (\square), for F127-SDS mixtures containing 10 mM (\circ), 300 mM (\triangle), 500 mM (∇) SDS and a dilute aqueous solution of 95 nm polystyrene spheres (shown by dashed line) at $T = 40^\circ\text{C}$ and $\theta = 90^\circ$. The concentration of the F127 solution is fixed at 0.25 g/cc. The inset shows the linear-logarithmic plots of $C[\tau]$ vs. τ for the same data sets, with the corresponding exponential fits to the faster relaxation processes shown by solid lines (data sets are shifted vertically for better visibility). The data of 3.6(a) is replotted as $\ln(-\ln(C[\tau]))$ vs. $\ln[\tau]$ in 3.6(b). The inset of 3.6(b) shows the linear fits to $1/\tau_R$ (extracted from the exponential fits) vs. q^2 for all the samples.

samples (the F127 solution and the F127-SDS mixture with 10 mM SDS, denoted by red squares and blue circles respectively) do not show complete decays to the noise level within the experimental time window. This confirms the slowing down of the slow relaxation times of these samples due to the kinetic constraints experienced by the close-packed micelles. For F127-SDS mixtures with higher SDS content (300 mM and 500 mM, denoted by magenta up triangles and green down triangles respectively), $C[\tau]$ shows a comparatively faster decay within the experimental time window, indicating that the relaxation times of mixtures with higher SDS content are much faster than those with lower SDS content. The data of Fig. 3.6(a) is recast in Fig. 3.6(b) where $\ln(-\ln(C[\tau]))$ is plotted vs. $\ln[\tau]$. For all the samples, the initial part of the plot comprises a straight line of slope 1, indicating a fast monoexponential component in the sample dynamics. For the pure F127 solution and the F127-SDS mixtures,

the plot shows a transition at $\ln[\tau] \approx 3$ to a second slower regime which is characterized by a change in the slope of the straight lines to very small values. For the 0.25 g/cc F127 solution (red squares) and the F127-SDS mixture with 10mM SDS (blue circles), the slope of the straight line in the slow regime is approximately 0.05. For the F127-SDS mixtures with 300mM and 500mM SDS (denoted by magenta up triangles and green down triangles respectively), the slow regime is characterized by a more complex functional form, with the data eventually increasing rapidly to the experimental noise level set by the PS spheres at $\ln[\tau] \geq 10$. This indicates a speeding up of the slow dynamics in these samples.

It is now understood that the addition of SDS to F127 solutions results in the adsorption of the DS^- chains to the hydrophobic PPO cores of the F127 micelles. This imparts negative charges to the mixed aggregates. The resulting intra-aggregate repulsion leads to the breakdown of the large spherical micelles into smaller mixed micelles comprising both F127 and SDS [18, 19]. Previous experiments [17] suggest that the addition of small amounts of SDS can result in the formation of large copolymer-rich charged complexes, while the addition of larger amounts of SDS results in the breakup of these complexes and the formation of smaller surfactant-rich complexes. For high concentrations of SDS, the mixtures comprise anisotropic SDS-rich mixed micelles and pure SDS micelles of smaller sizes [17, 19]. In contrast to pure copolymer solutions where the micellar aggregates are spherical and monodisperse, the aggregates present in mixtures are characterized by substantial anisotropy and polydispersity. Anisotropic particles possess more rotational degrees of freedom than spherical particles and therefore require higher numbers of contacts for mechanically stable close packings. The packing volume fraction required for the random close packing (ϕ_{RCP}) of anisotropic particles is therefore substantially larger than the ϕ_{RCP} of spherical, monodisperse particles [36, 37]. Simulations of colloidal hard sphere systems [39, 40], theoretical models [41]

and experimental studies [42, 43] show that ϕ_{RCP} increases with increase in the standard deviation of the particle size. Since smaller spheres can fill the gaps between larger particles very efficiently in packings of polydisperse spheres, the increase of ϕ_{RCP} with polydispersity is not surprising. Changes in SDS content in F127-SDS mixtures result in changes in the number fractions of the different micellar species in solution. This induces large changes in the packing behaviors of the aggregates. As a result, F127-SDS mixtures are characterized by ϕ_{RCP} values that are higher than those expected for pure F127 solutions. Increase in ϕ_{RCP} removes the space constraints previously experienced by the overlapping micelles and results in the unjamming and decompaction of the aggregates in F127-SDS mixtures. This manifests as a speeding up of the microscopic dynamics and the disappearance of soft glassy rheology of the mixtures as SDS content is increased.

In the inset of Fig. 3.6(a), the intensity autocorrelation functions are re-plotted on a linear-logarithmic scale (the data is shifted vertically for better visibility) and the fast decays are fitted to the form $C[\tau] \sim \exp(-\frac{\tau}{\tau_R})$ for six different wave vectors. It is observed that $1/\tau_R$ varies linearly with q^2 (shown in the inset of 3.6(b)), confirming the diffusive nature of the fast relaxation processes. For the jammed samples (pure F127 solution and the F127-SDS mixture with 10 mM SDS, denoted by red squares and blue circles in Figs. 3.6(a) and (b)), the fast processes are attributed to the constrained diffusion of confined micelles. In the F127-SDS mixtures with 300 mM and 500 mM SDS (denoted by magenta up triangles and green down triangles in Fig. 3.6), the constituent aggregates tend to unjam due to the anisotropy and the polydispersity of the constituent aggregates. At high concentrations of SDS, a significant fraction of SDS molecules exist as pure SDS micelles [19] which, due to their small sizes, can diffuse easily through the free spaces available in the system. By combining the Stokes-Einstein relation with the measured diffusive relaxation rates for the mixtures with high SDS content, it is estimated that the fast exponential

3. JAMMING BEHAVIOR OF TRIBLOCK COPOLYMER SOLUTIONS AND TRIBLOCK COPOLYMER-ANIONIC SURFACTANT MIXTURES

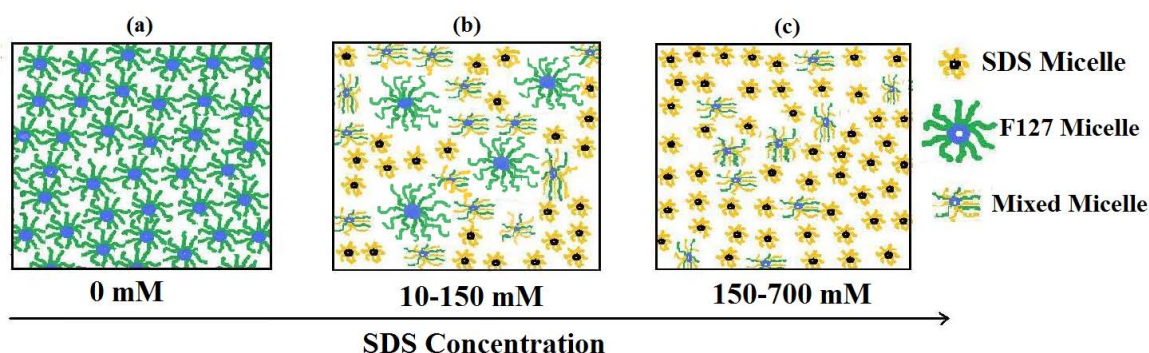


FIGURE 3.7: Cartoon depicting the unjamming of micellar aggregates due to the formation of mixed micelles and free SDS micelles upon the addition of SDS to 0.25 g/cc F127 solutions. Here, (a) shows closely packed F127 micelles due to jamming in pure, concentrated F127 solutions, while (b) and (c) show the formation of mixed micelles and free SDS micelles due to the addition of SDS and the subsequent micellar unjamming.

decays are due to the relaxation of scatterers of size $\sim 1\text{-}2$ nm [19, 44] which can be identified as spherical SDS micelles. This jamming-unjamming transition due to change in packing behavior in the presence of SDS is summarized in Fig. 3.7.

Temperature sweep oscillatory rheology experiments are next performed by ramping up the sample temperatures at a rate of $0.25^\circ\text{C}/\text{minute}$, while keeping the amplitude of the oscillatory strain constant at $\gamma = 0.5\%$ at an angular frequency $\omega = 1$ rad/s. This data is plotted in Fig. 3.8. At the lowest temperatures, the samples comprise unimers in solution and are characterized by low values of the elastic modulus: $G' \sim 1\text{-}10$ mPa and $G' < G''$ (G' data is shown in Fig. 3.8). Above a certain temperature, each sweep is characterized by an abrupt increase of the elastic modulus G' to a higher value that decreases sharply with SDS concentration. The increase in G' is identified with a liquid-solid phase transition and is consistent with the data reported in a previous publication [4]. Our observation that the temperature sweep data of the mixtures are characterized by lower values of G' at temperatures greater than the liquid-solid transition temperature is consistent with the picture of micellar

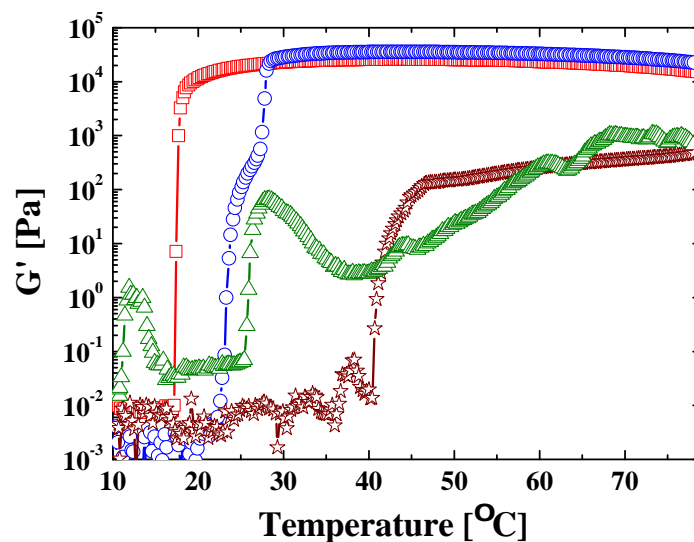


FIGURE 3.8: Temperature sweep data showing the evolution of G' in an F127 solution of concentration 0.25 g/cc (\square) and when 50 mM (\circ), 150 mM (\star) and 700 mM (\triangle) SDS are added to pure F127 solutions.

unjamming in mixtures proposed earlier. This conclusion is supported by the rheology and DLS data displayed earlier in Figs. 3.5 and 3.6.

To summarize the jamming-unjamming behavior exhibited by the pure F127 solution and F127-SDS mixtures (F127 concentration is fixed at 0.25 g/cc), we construct a phase diagram in the temperature-SDS concentration plane (Fig. 3.9). The grey region in this phase diagram indicates the soft solid regime (comprising jammed aggregates), while the white region represents the liquid-like response that is typically seen below the critical micellization temperature. The phase boundary corresponds to the temperature at which the liquid-solid transition occurs in each sample and is found to have a non-monotonic dependence on SDS concentration. The jammed region is characterized by different degrees of disorder and metastability and the elasticity of this phase varies over almost two orders of magnitude as SDS concentration is varied. Inset (a) of Fig. 3.9 shows the frequency response curves measured at 42°C for the 0.25 /cc F127 sample (red squares) and when 150 mM and 700 mM SDS

3. JAMMING BEHAVIOR OF TRIBLOCK COPOLYMER SOLUTIONS AND TRIBLOCK COPOLYMER-ANIONIC SURFACTANT MIXTURES

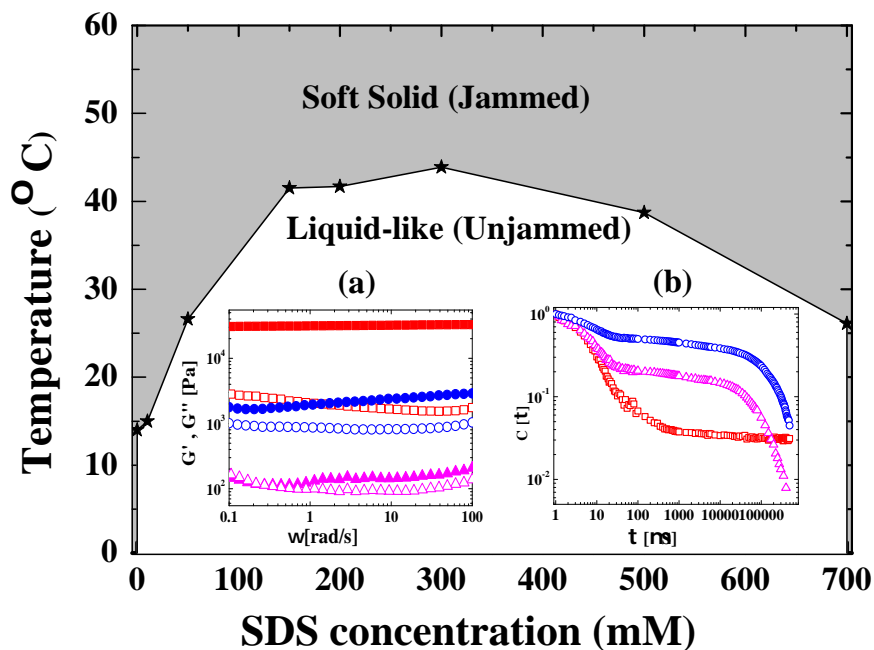


FIGURE 3.9: Phase diagram in the temperature-SDS concentration plane when F127 concentration is fixed at 0.25 g/cc. The grey region denotes the jammed soft solid phase while the white region represents the liquid-like (unjammed) regime. Inset (a) shows the frequency responses at 42°C for a pure F127 solution (\square) and for F127-SDS mixtures with SDS concentrations 150 mM (\circ) and 700 mM (\triangle). The solid symbols denote G' and the hollow symbols denote G'' . Inset (b) shows the DLS data for the same samples.

(blue circles and magenta triangles respectively) are added to this sample. G' , denoted by solid symbols, and G'' , denoted by hollow symbols, are measured while decreasing the angular frequency logarithmically from 100 rad/s to 0.1 rad/s. The strain amplitude is held fixed at 0.5% to ensure linear response in all the samples. As expected, the measured moduli decrease sharply with increasing surfactant concentration. For the pure F127 sample (red squares), $G' \gg G''$ and is independent of the angular frequency over the entire measurement range, while G'' is weakly frequency dependent. These are typical signatures of soft glassy rheology [7, 8]. With increasing SDS concentration,

the soft glassy behavior becomes much less prominent. In the frequency response data for the F127-SDS mixture with an SDS concentration of 700 mM (magenta triangles in inset (a) of Fig. 3.9), G' and G'' are almost equal, indicating that the sample displays a weak solid-like behavior over the entire frequency range investigated here. Inset (b) of Fig. 3.9 shows the DLS data for the same samples. It is observed that after an initial fast decay, the 0.25 g/cc sample (red squares) slows down enormously and does not decay within the experimental time window. With the addition of SDS (150 mM SDS and 700 mM SDS, denoted by blue circles and magenta triangles respectively), the slow decay becomes faster, which is identified as the onset of micellar unjamming. Our frequency response and DLS data, combined with the amplitude sweep measurements displayed in Fig. 3.5, confirm the gradual disappearance of soft glassy rheology in F127-SDS mixtures on increasing SDS concentration.

3.4 Conclusions

Dynamic light scattering is employed to study the microscopic dynamics of the aggregates that constitute pure F127 solutions and F127-SDS mixtures. This data is related to the mechanical properties of the samples measured using oscillatory rheology. Above a critical temperature, the F127 copolymers in an aqueous solution self-assemble to form micelles with hydrophobic PPO cores and hydrophilic PEO coronas. The PEO chains, which interact *via* a soft potential, overlap and compress with increasing copolymer concentration. The jamming behavior that arises from such macromolecular crowding at F127 concentration ≥ 0.10 g/cc increases the solidity of the samples. By combining DLS and rheology data, it is shown that the appearance of soft glassy rheology in the samples is accompanied by a slowing down of their characteristic relaxation time scales. When sufficient quantities of the anionic surfactant SDS is added to a jammed solution of F127 micelles, the pure F127 micelles break

3. JAMMING BEHAVIOR OF TRIBLOCK COPOLYMER SOLUTIONS AND TRIBLOCK COPOLYMER-ANIONIC SURFACTANT MIXTURES

up to form anisotropic mixed micelles that are typically much smaller than pure F127 micelles. These anisotropic mixed aggregates, together with the SDS micelles that exist in solution, increase the polydispersity of the sample, thereby increasing its random close packing fraction and resulting in an unjamming of the aggregates in F127-SDS mixtures. This unjamming phenomenon manifests as a dramatic decrease in the complex moduli of these mixtures and is accompanied by a disappearance of the signature features of soft glassy rheology. Finally, a phase diagram is constructed in the temperature-SDS concentration plane to summarize the jamming-unjamming behavior of micelles in F127-SDS mixtures.

References

- [1] A. J. Liu and S. R. Nagel, *Nature* **396**, 21 (1998).
- [2] V. Trappe, V. Prasad, Luca Cipelletti, P. N. Segre and D. A. Weitz, *Nature* **411**, 772 (2001).
- [3] E. I. Corwin, H. M. Jaeger and S. R. Nagel, *Nature* **435**, 1075 (2005).
- [4] P. Harsha Mohan and R. Bandyopadhyay, *Phys. Rev. E* **77**, 041803 (2008).
- [5] P. Sollich, F. Lequeux, P. Hebraud and M. E. Cates, *Phys. Rev. Lett.* **78**, 2020 (1997).
- [6] P. Sollich, *Phys. Rev. E* **58**, 738 (1998).
- [7] H. M. Wyss, K. Miyazaki, J. Mattsson, Z. Hu, D. R. Reichman and D. A. Weitz, *Phys. Rev. Lett.* **98**, 238303 (2007).
- [8] K. Miyazaki, H. M. Wyss, D. A. Weitz and D. R. Reichman, *Europhys. Lett.* **75**, 915 (2006).
- [9] K. Hyun, S. H. Kim, K. H. Ahn and S. J. Lee, *J. Non-Newtonian Fluid Mech.* **107**, 51 (2002).

-
- [10] L. Lobry, N. Micali, F. Mallamace, C. Liao and S.-H Chen, *Phys. Rev. E* **60**, 7076 (1999).
- [11] V. Castelletto, C. Caillet, J. Fundin, I. W. Hamley, Z. Yang and A. Kelarakis, *J. Chem. Phys.* **116**, 10947 (2002).
- [12] H. Yardimci, B. Chung, J. L. Harden and R. L. Leheny, *J. Chem. Phys.* **123**, 244908 (2005).
- [13] A. V. Kabanov, E. V. Batrakova and V. Y. Alakhov, *J. Controlled Release* **82**, 189 (2002).
- [14] W. van Meegen and P. N. Pusey, *Physical Review A* **43**, 5429 (1991).
- [15] P. N. Pusey and W. van Meegen, *Physica A* **157**, 705 (1989).
- [16] B. Foster, T. Cosgrove and B. Hammouda, *Langmuir* **25**, 6760 (2009).
- [17] J. Jansson, K. Schillen, G. Olofsson, R C da Silva and W. Loh, *J. Phys. Chem. B* **108**, 82 (2004).
- [18] N. V. Sastry and H. Hoffmann, *Colloids Surfaces A* **250**, 247 (2004).
- [19] E. Hecht and H. Hoffmann, *Langmuir* **10**, 86 (1994).
- [20] R. Ivanova, P. Alexandridis and B. Lindman, *Colloids Surfaces A* **183**, 41 (2001).
- [21] P. R. Desai, N. J. Jain, R. K. Sharma and P. Bahadur, *Colloids Surfaces A* **178**, 57 (2001).
- [22] Y. Li, R. Xu, S. Couderc, D. M. Bloor, E. Wyn-Jones and J. F. Holzwarth, *Langmuir* **17**, 183 (2001).
- [23] E. Hecht, K. Mortensen, M. Gradzielski and H. Hoffmann, *J. Phys. Chem.* **99**, 4866 (1995).

-
- [24] R. Ganguly, V. K. Aswal, P. A. Hassan, I. K. Gopalakrishnan and S. K. Kulshreshtha, *J. Phys. Chem.* **110**, 9843 (2006).
- [25] T. Thurn, S. Couderc, J. Sidhu, D. M. Bloor, J. Penfold, J. F. Holzwarth and E. Wyn-Jones, *Langmuir* **18**, 9267 (2002).
- [26] Y. Li, R. Xu, D. M. Bloor, J. F. Holzwarth and E. Wyn-Jones, *Langmuir* **16**, 10515 (2000).
- [27] J. Mata, T. Joshi, D. Varade, G. Ghosh and P. Bahadur, *Colloids Surfaces A* **247**, 1 (2004).
- [28] K. Kurumada and B. H. Robinson, *Prog. Colloid Polym. Sci.* **123**, 12 (2004).
- [29] C. W. Macosko, *Rheology: Principles, Measurements and Applications* (Wiley-VCH, New York, 1994).
- [30] G. Wanka, H. Hoffmann and W. Ulbricht, *Colloid Polym. Sci.* **268**, 101 (1990).
- [31] R. H. Colby, J. R. Gillmor and M. Rubinstein, *Phys. Rev. E* **48**, 3712 (1993).
- [32] R. K. Prud'homme, G. Wu and D. K. Schneider, *Langmuir* **12**, 4651 (1996).
- [33] B. Nystrom and A-L. Kjoniksen, *Langmuir* **13**, 4250 (1997).
- [34] R. Bandyopadhyay, P. H. Mohan and Y. M. Joshi, *Soft Matter* **6**, 1462 (2010).
- [35] P.G. Nilsson, H. Wennerstrom and B. Lindman, *J. Phys. Chem.* **87**, 1377 (1983).
- [36] A. Donev, R. Connely, F.H. Stillinger and S. Torquato, *Phys. Rev. E* **75**, 051304 (2007).

- [37] A. Donev, I. Cisse, D. Sachs, E. A. Variano, F. H. Stillinger, R. Connelly, S. Torquato and P. M. Chaikin, *Science* **303**, 990 (2004).
- [38] S. R. Williams and A. P. Philipse, *Phys. Rev. E* **67**, 051301 (2003).
- [39] W. Schaertl and H. Sillescu, *J. Stat. Mech.* **77**, 1007 (1994).
- [40] A. Yang, C. T. Miller and L. D. Turcoliver, *Phys. Rev. E* **53**, 1516 (1996).
- [41] N. Ouchiyama and T. Tanaka, *Ind. Eng. Chem. Fundamen.* **20**, 66 (1981).
- [42] H. Y. Sohn and C. Moreland, *Canadian J. Chem. Eng.* **46**, 162 (1968).
- [43] M. Suzuki, H. Sato, M. Hasegawa and M. Hirota, *Powder Tech.* **118**, 53 (2001).
- [44] M. Almgren and S. Swarup, *J. Phys. Chem.* **86**, 4212 (1982).

4

Encapsulation of drugs in Pluronic F127 Micelles: The Effects of Drug Hydrophobicity, Solution Temperature and pH

4.1 Introduction

In recent times, block copolymers have emerged as a potential agent for targeted drug delivery and gene therapy [1–5]. One such block copolymer proposed for controlled drug delivery is Pluronic, which has a triblock PEO-PPO-PEO structure (PEO: polyethylene oxide, PPO: polypropylene oxide). At high

temperatures, the central PPO block becomes hydrophobic, while the PEO blocks remain hydrophilic [6]. Due to this amphiphilic nature, Pluronic molecules, above a critical temperature and concentration, self-aggregate in aqueous solutions to form spherical micelles with hydrophobic PPO cores surrounded by hydrophilic PEO coronas. This has been discussed in the earlier chapters.

The formation of micellar block copolymer-drug complexes was first proposed by Dorn *et al.* [7]. When hydrophobic drug molecules are mixed with suitable quantities of Pluronic molecules and the temperature is raised, the drug molecules accumulate in the hydrophobic PPO cores. The hydrated PEO coronas are non-toxic and prevent the drug molecules from being removed from the core. The solubilities of the hydrophobic drugs therefore increase substantially in an aqueous medium, increasing the bioavailability of the drugs [8]. It has been reported that the passive accumulation of drugs encapsulated in Pluronic micelles at solid tumor cells is more efficient than that of free drugs [2]. This arises from the long circulation time of the drug-encapsulated micelles and the slow dissociation of drugs from these micelles in the blood circulation system [2]. Drug-encapsulated Pluronic micelles can also enhance the transport of drugs across the blood-brain and intestinal barriers [1, 2]. These and other pharmaceutical advantages of Pluronic micelles make it a serious contender as a drug carrier [9].

The solubilization of drugs in Pluronic micelles has been extensively studied in recent times. It is reported in the literature that the presence of the hydrophobic drug molecules naproxen and indomethacin in F127 solutions result in slight decreases in the micellar sizes and aggregation numbers, in addition to a lowering of the gelation temperature [10]. The aggregation behavior of F127 micelles has been studied systematically when drugs of varying hydrophobicities are incorporated in the micellar cores [11]. It is found that the most hydrophobic drugs increase the sizes of the micellar core and corona while generally decreasing the micellar aggregation numbers. Scherlund *et*

al. observe a decrease in the critical micellization temperature (CMT) and the gelation temperature when local anesthetics are added to Pluronic solutions [4]. These authors further confirm that these temperatures decrease with dilution and increase in solution pH. More recently, Foster *et al.* encapsulated Ibuprofen molecules in Pluronic P-104 and P-105 solutions and Flurbiprofen molecules in P103 and P123 solutions. Using SANS and pulsed-field gradient stimulated-echo nuclear magnetic resonance (NMR) measurements, they demonstrate that the encapsulation of drugs favors the micellization process, resulting in an increase in the aggregation number and the micellar core radius [12, 13]. A strong dependence of the aggregation number and the core radius on the solution pH is reported when Ibuprofen is added to P104 solutions and Flurbiprofen to P103 and P123 solutions [14, 15].

In this work, the non-steroidal anti-inflammatory drug Ibuprofen, the salicylate analgesic drug Aspirin and the macrolide antibiotic drug Erythromycin are encapsulated in the hydrophobic cores of spherical Pluronic F127 micelles. The dilute, completely fluid-like F127 solutions used here are studied at several temperatures and pH values and are prepared at concentrations that are much higher than the critical micellization concentrations of F127 at the temperatures studied. The encapsulation of drugs in Pluronic F127 micelles are studied using cryo-SEM, DLS, small angle X-ray scattering and fluorescence spectroscopy. The changes in the CMTs of the solutions, the variations in the hydrodynamic radii of the micelles containing the encapsulated drugs and the micellar polydispersities are investigated using DLS. The temperature dependence of the encapsulation process and the penetration of solvent in the micellar core are studied using fluorescence spectroscopy. Finally, the release of the drugs from the micellar cores when solution pH is increased is reported.

4. ENCAPSULATION OF DRUGS IN PLURONIC F127 MICELLES: THE EFFECTS OF DRUG HYDROPHOBICITY, SOLUTION TEMPERATURE AND PH

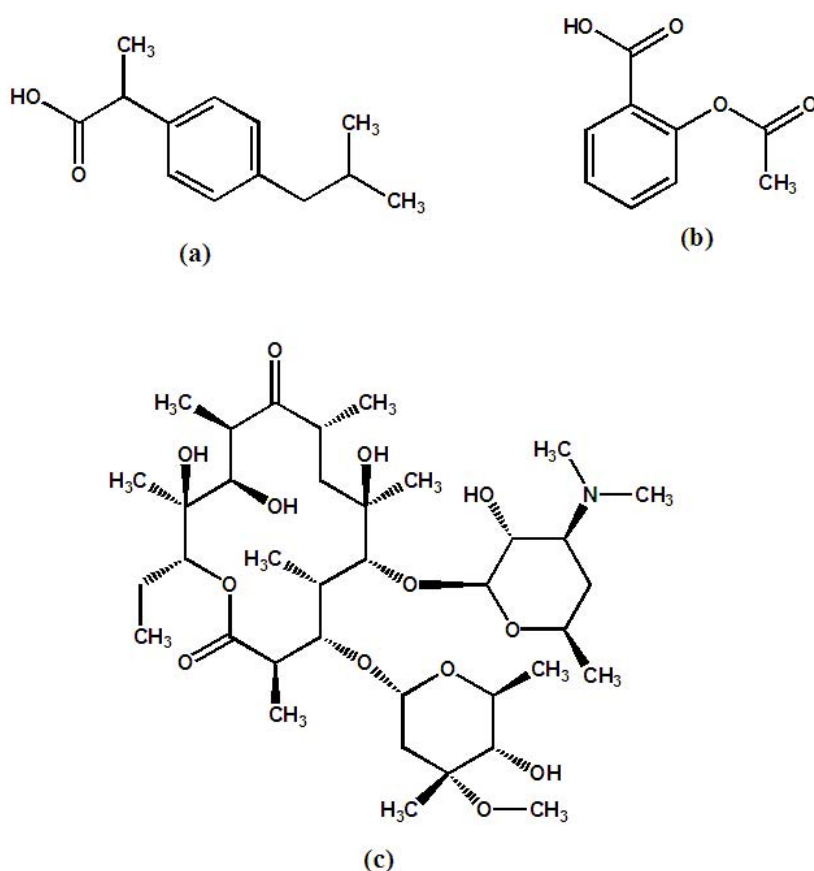


FIGURE 4.1: Chemical structures of (a) Ibuprofen, (b) Aspirin and (c) Erythromycin.

4.2 Sample preparation

Pluronic F127, Ibuprofen, Aspirin and Erythromycin are purchased from Sigma-Aldrich and used as received without further purification. Ibuprofen (mol. wt. 206.29 g/mol), Aspirin (mol. wt. 180.16 g/mol) and Erythromycin (mol. wt. 733.93 g/mol) are three aromatic hydrophobic drug molecules characterized by different chemical architectures (Fig. 4.1). All these drug molecules are weakly acidic in aqueous solutions. Aspirin is more acidic (pKa 3.5) compared to Ibuprofen (pKa 5.38) and Erythromycin (pKa 8.8) [16–18]. To prepare a pure F127 solution, an appropriate amount of F127 is dissolved in deionized and distilled Millipore water and stirred vigorously with a magnetic stirrer. The octanol-water partition coefficients ($\log P_{oct/water}$) [19], which are measures of

Name of drug	$\log P_{oct/water}$	C_t
Ibuprofen	3.5	0.03 wt.%
Aspirin	1.19	0.3 wt.%
Erythromycin	3.06	0.05 wt.%

Table 4.1: The octanol-water partition functions $\log [P_{oct/water}]$ of the three drugs used here and the C_t values obtained from the DLS data are tabulated below.

the drug hydrophobicity, are listed in Table 4.1. This table shows that of the three drug molecules used in this study, Ibuprofen is the most hydrophobic, followed by Erythromycin and Aspirin.

The concentrations of the F127 samples used here are fixed at 5.26 wt%, 2.04 wt% and 1.02 wt%. These concentrations are much higher than the CMCs of the F127 solutions at the temperatures studied in this work. Drug molecules are incorporated in Pluronic F127 micelles by vigorously stirring aqueous mixtures of the drugs and F127 in an ultrasonicator at temperatures between 40°C and 60°C.

4.3 Results and Discussion

Direct visualization of the Pluronic F127 micelles is performed with cryo-SEM. The samples, initially at room temperature (25°C), are cryo-fractured in liquid nitrogen. A representative image of a 5.26 wt% F127 solution is shown in Fig. 4.2(a). The globular structures of F127 micelles, of average sizes 68-70 nm, are clearly visible. When drug molecules are added to Pluronic micellar solutions, they assemble in the hydrophobic core. The cryo-SEM images of F127 micelles encapsulating 0.1 wt% each of Ibuprofen, Aspirin and Erythromycin respectively are shown in Figs. 4.2 (b), (c) and (d), respectively. In each sample, the micelles retain their globular structures. In the concentration range investigated, cylindrical or lamellar aggregates [20, 21] are not observed. The

4. ENCAPSULATION OF DRUGS IN PLURONIC F127 MICELLES: THE EFFECTS OF DRUG HYDROPHOBICITY, SOLUTION TEMPERATURE AND PH

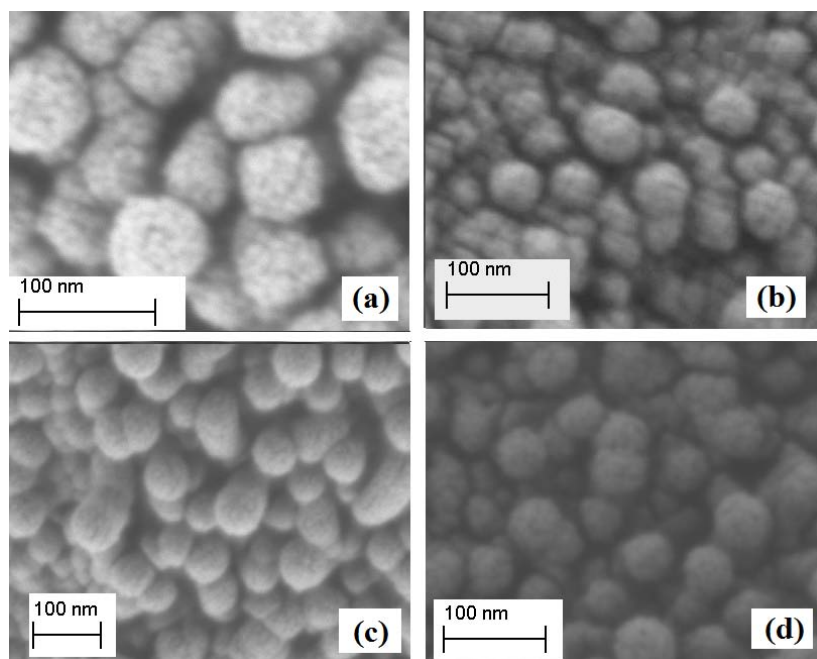


FIGURE 4.2: Cryo-SEM images of 5.26 wt% F127 micelles (a) with no encapsulated drugs, and when (b) 0.1 wt% Ibuprofen, (c) 0.1 wt% Aspirin and (d) 0.1 wt% Erythromycin are incorporated in the micellar cores.

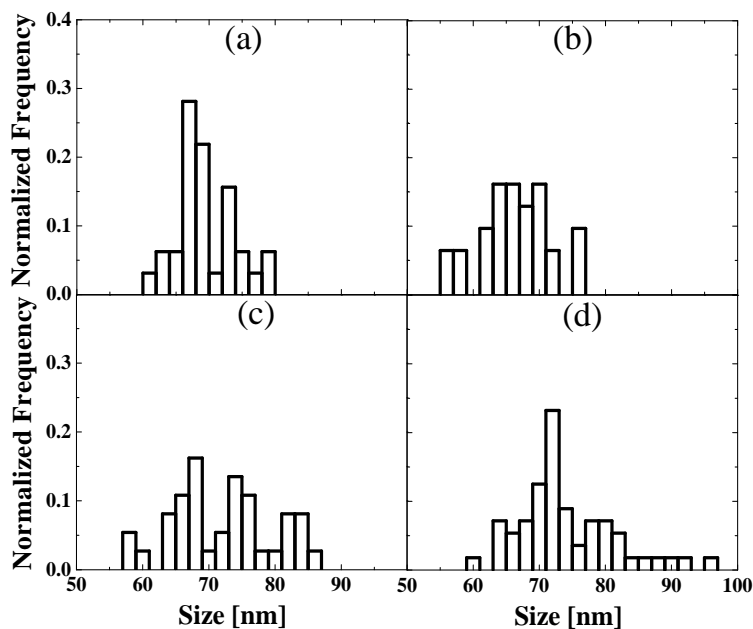


FIGURE 4.3: Size distributions, derived from cryo-SEM images of micelles of 5.26 wt% F127 solutions (a) without drugs, (b) with 0.1 wt.% Ibuprofen, (c) with 0.1 wt.% Aspirin and (d) with 0.1 wt.% Erythromycin.

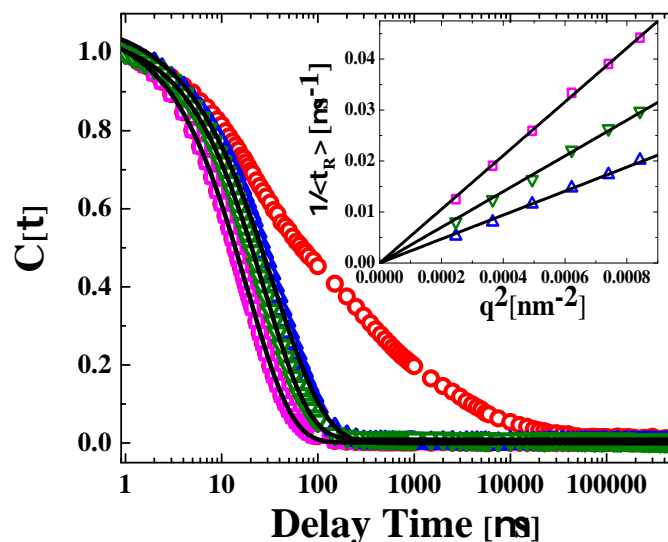


FIGURE 4.4: The normalized intensity autocorrelation functions $C[\tau]$ are plotted for a pure 5.26 wt% F127 sample at 20°C (red circles), 25°C (blue up-triangles), 40°C (green down-triangles) and 60°C (pink squares). The stretched exponential fits to the data at 60°C, 40°C and 25°C are shown by solid lines. In the inset, $1/\langle \tau_R \rangle$ is plotted vs. q^2 for data obtained at 60°C, 40°C and 25°C and linear fits to the data are shown (solid lines).

average sizes of these globular micelles are calculated from these cryo-SEM images. Assuming elliptical shapes of the micelles, one can calculate the average radius R as $R = \sqrt{ab}$ where a and b are, respectively, the lengths of the semi-major and semi-minor axes of the micelles. Size distributions of these drug-encapsulated micelles are plotted in Fig. 4.3.

In contrast to cryo-SEM, DLS is a non-invasive technique and yields sizes and distributions over the entire scattering volume. Systematic DLS measurements are next performed at several temperatures with 5.26 wt% F127 solutions, both with and without drugs. In these measurements, the normalized intensity autocorrelation functions [$C[\tau] = g^{(2)}(\tau) - 1$] are measured at several scattering angles while varying the delay times τ at different temperatures within the range 12°C - 60°C. Fig. 4.4 shows the data at 60°C (squares), 40°C (down-triangles) and 25°C (up-triangles) for 5.26 wt% F127 solutions.

The data acquired at each of these temperatures fit well to stretched exponential functions of the form $C[\tau] \sim \exp(-\tau/\tau_R)^\beta$ (where τ_R is the relaxation time and the stretching exponent $\beta \leq 1$ accounts for the distribution of relaxation times of the scatterers). For every sample, $C[\tau]$ is measured at six different q values and the corresponding τ_R and β are extracted. The mean relaxation time $\langle \tau_R \rangle$ is estimated using the relation $\langle \tau_R \rangle = \tau_R/\beta * \Gamma(1/\beta)$, where Γ is the Euler gamma function. The inset of Fig. 4.4 shows that at all three temperatures, $1/\langle \tau_R \rangle$ varies linearly with q^2 with $1/\langle \tau_R \rangle \rightarrow 0$ as $q \rightarrow 0$, a signature of the diffusive motion of the nearly spherical micelles. If the sample temperature is lowered to 20°C (circles in Fig. 4.4), $C[\tau]$ no longer fits to a stretched exponential form. This indicates the breakup of the spherical micelles into free unimers in solution and indirectly establishes the CMT of the sample to lie between 20°C and 25°C. By systematically inspecting the shape changes in $C[\tau]$ at several temperatures, the CMT of this sample is estimated to be $23^\circ \pm 1^\circ\text{C}$. This estimate matches well with previous results obtained using DSC [22], SLS and fluorescence spectroscopy [23] and is also confirmed by our cryo-SEM images which show that the F127 solution, quenched rapidly from 25°C, is comprised of spherical micelles.

DLS measurements are next performed after incorporating different quantities of drug molecules in 5.26 wt% F127 solutions in the temperature range 12°C - 60°C. It is observed that all the $C[\tau]$ data in this temperature range fit well to stretched exponential functions (Fig. 4.5). For all the data acquired, $1/\langle \tau_R \rangle$ varies linearly with q^2 (inset (a) of Fig. 4.5), suggesting that the samples are in the micellar liquid phase. The CMTs of all the drug-incorporated micellar samples therefore lie below the experimental temperature limit of 12°C. The reduction in the CMTs of the micellar solutions observed here due to drug encapsulation is consistent with previous reports [4, 12]. The hydrophobicity of the PPO cores increases considerably due to the addition of the drug

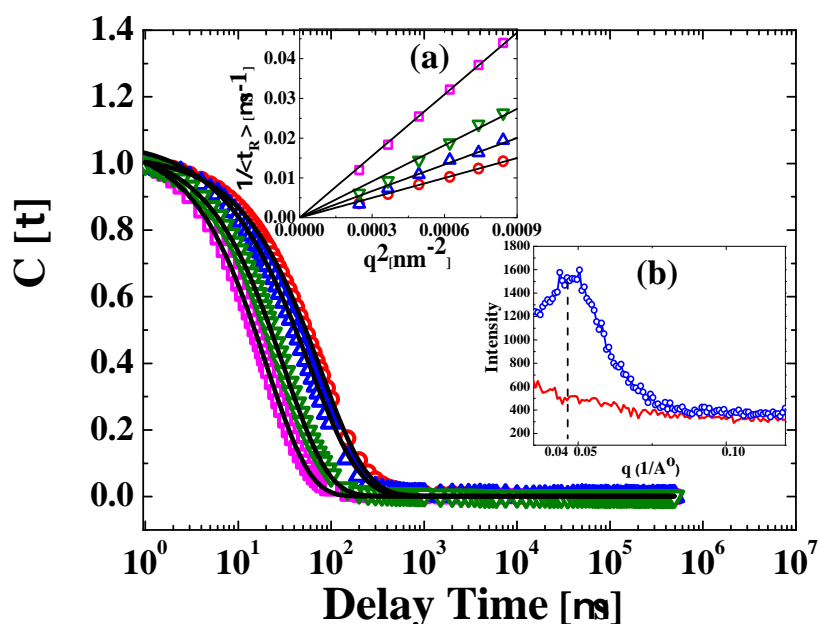


FIGURE 4.5: The normalized intensity autocorrelation functions $C[\tau]$ are plotted for 5.26 wt% F127 solutions with 0.1 wt% Ibuprofen at 20°C (red circles), 25°C (blue up-triangles), 40°C (green down-triangles) and 60°C (pink squares), respectively. The stretched exponential fits are shown by solid lines. The inset (a) shows that $1/\langle \tau_R \rangle$ varies linearly with q^2 for all the samples. (b) SAXS data showing $I(q)$ vs. q for a 5.26 wt% F127 solution incorporating 0.25 wt% Ibuprofen is plotted at 60°C (blue circle-line) and 4°C (red solid line).

molecules. This favors micellar aggregation at lower temperatures, resulting in the observed lowering of the CMT.

The acceleration of the aggregation process with increasing hydrophobicity is also confirmed by our observation that increasing drug hydrophobicity leads to micelle formation at lower threshold concentrations. The threshold concentration C_t for a given drug is calculated by estimating CMTs of the solutions at several drug concentrations. For very low drug concentrations, $C[\tau]$ changes from a stretched exponential to a non-exponential form at around 23°C, the CMT of pure F127 solutions. When drugs are added to the micellar solutions above a threshold concentration C_t , a rather abrupt decrease in the solution CMT is noticed, and the autocorrelation function is always of stretched exponential form in the experimental temperature range of 12°C - 60°C. The C_t

4. ENCAPSULATION OF DRUGS IN PLURONIC F127 MICELLES: THE EFFECTS OF DRUG HYDROPHOBICITY, SOLUTION TEMPERATURE AND PH

values for all three drugs are estimated and listed in Table 4.1. The comparison between the octanol-water partition coefficients ($\log P_{oct/water}$) and C_t for different drugs in Table 1, suggests that increase in the hydrophobicity reduces C_t , thereby favoring the formation of micelles at lower concentrations.

SAXS measurements are also performed to confirm the lowering of the CMT of an Ibuprofen-encapsulated F127 solution above C_t . The SAXS data at 4°C and 60°C are shown in the inset (b) of Fig. 4.5, where the scattered X-ray intensity $I(q)$ is plotted vs. q for 60°C (circle-line) and 4°C (solid line). At 60°C, a peak in $I(q)$ at $q = 0.004$ 1/nm is seen, which indicates the presence of micellar structures with diameters of $2\pi/q = 15.7 \pm 0.1$ nm in solution. At 4°C, the peak completely disappears, confirming the absence of spherical micelles. Combining the X-ray and DLS measurements, it is concluded that the CMT of the Ibuprofen-encapsulated F127 micellar solutions lies somewhere in the range between 4°C and 12°C. This confirms our earlier observation that drug encapsulation stabilizes F127 micelles over a broader temperature range.

For the addition of Aspirin and Erythromycin to 5.26 wt% F127 solutions above their respective C_t s, the $C[\tau]$ vs. τ plots show fits to stretched exponential forms in the temperature range 12°C - 60°C. Such plots are shown in Figs. 4.6(a) - 4.6(d). For every experiment, the relaxation time τ_R is obtained at each q . It is seen that $1/\langle \tau_R \rangle$ varies linearly with q^2 with $1/\langle \tau_R \rangle \rightarrow 0$ as $q \rightarrow 0$ in all cases (insets of Figs. 4.6(a) - 4.6(d)). The same trends are repeated when drugs are incorporated in a more dilute F127 solution. Data for a 2.04 wt% F127 solution is displayed in Figs. 4.6(e) and 4.6(f). The slopes of the linear fits to the $1/\langle \tau_R \rangle$ vs. q^2 data yield the translational diffusion coefficients D . The average hydrodynamic radii R_H of the micelles can be estimated from these D values using Stokes-Einstein relation. From the stretching exponent β , one can calculate the size distribution of the micelles by calculating the

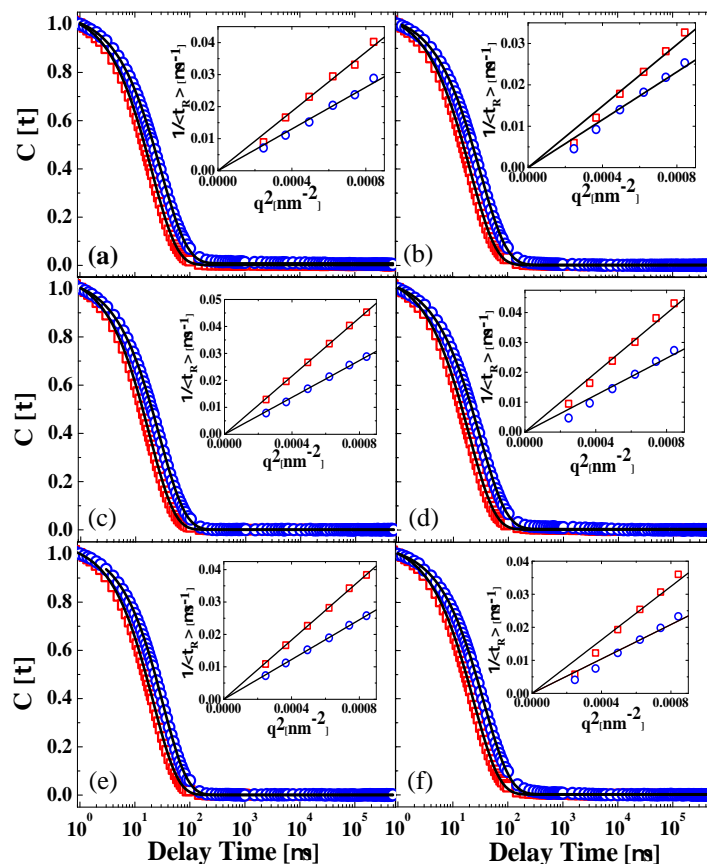


FIGURE 4.6: The normalized intensity autocorrelation functions $C[\tau]$ are plotted at 60°C (red squares) and 40°C (blue circles) for 5.26 wt% F127 solutions after the addition of (a) 0.5 wt.% Aspirin, (b) 0.1 wt.% Aspirin, (c) 0.05 wt.% Erythromycin and (d) 0.1 wt.% Erythromycin. The data for 2.04 wt% F127 solutions with 0.25 wt.% Ibuprofen and 0.1 wt.% Ibuprofen are plotted in (e) and (f) respectively. The stretched exponential fits are shown by solid black lines. In the insets, $1/\langle\tau_R\rangle$ vs. q^2 plots show linear fits (solid line) for all samples.

4. ENCAPSULATION OF DRUGS IN PLURONIC F127 MICELLES: THE EFFECTS OF DRUG HYDROPHOBICITY, SOLUTION TEMPERATURE AND PH

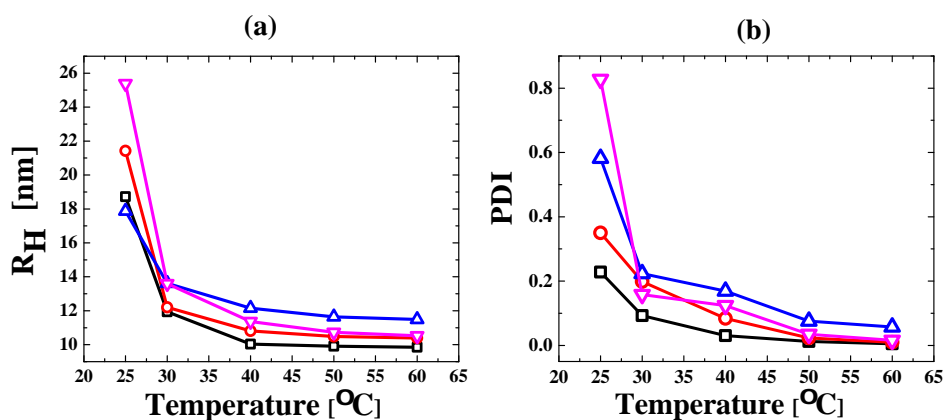


FIGURE 4.7: (a) Variation of R_H with temperature for a 5.26 wt% F127 solution without drugs (black squares) and after the encapsulation of 0.1 wt% Ibuprofen (red circles), 0.1 wt% Aspirin (blue up-triangles) and 0.1 wt% Erythromycin (pink down-triangles). (b) The plot shows polydispersity index (PDI) vs. temperature for 5.26 wt% F127 micelles with no drugs (black squares), 0.1 wt% Ibuprofen (red circles), 0.1 wt% Aspirin (blue up-triangles) and 0.1 wt% Erythromycin (pink down-triangles).

distribution of the relaxation time $\rho(\tau_R)$ using the formula [26]:

$$\rho(\tau_R) = \frac{\tau_R}{\pi t^2} \sum_{k=1}^{\infty} \frac{(-1)^k}{k!} \sin(\pi\beta k) \Gamma(\beta k + 1) \left(\frac{t}{\tau_R}\right)^{\beta k + 1}$$

As the Stokes-Einstein relation is expected to be valid in these dilute samples, the average micellar radius is expected to be proportional to the micellar relaxation time. We therefore calculate the polydispersity index (PDI) of the micellar aggregates from the distribution function of relaxation times $\rho(\tau_R)$ using the formula:

$$\text{PDI} = \left(\frac{\sigma_R}{\langle \tau_R \rangle} \right)$$

where σ_R and $\langle \tau_R \rangle$ are the standard deviation and mean values of $\rho(\tau_R)$. We have estimated σ_R from the calculated values of the full width at half maxima (FWHM) of $\rho(\tau_R)$ and estimated the micellar PDI using the following formula:

$$\text{PDI} = \left(\frac{\text{FWHM}}{\langle \tau_R \rangle} \right)$$

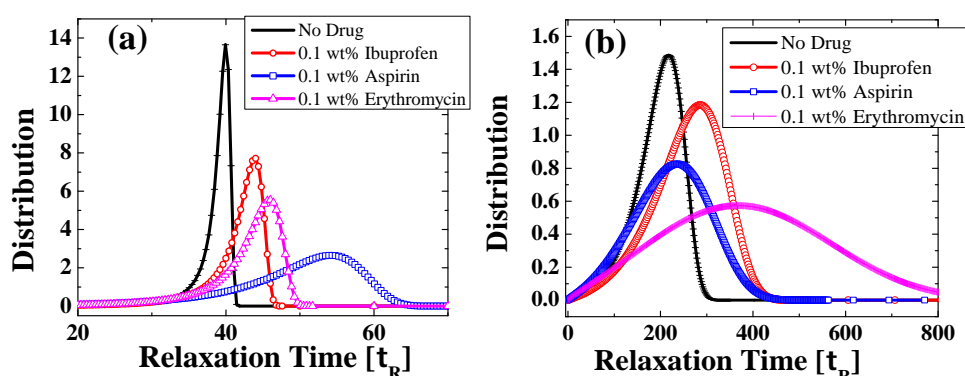


FIGURE 4.8: The plot shows the distributions of relaxation times for F127 micellar solutions with no drugs (black line), 0.1 wt% Ibuprofen (red circle), 0.1 wt% Aspirin (blue square) and 0.1 wt% Erythromycin (pink triangle) at (a) 60°C and (b) 25°C.

In Fig. 4.7(a), the variations of R_H of the micelles in 5.26 wt% F127 solutions, encapsulating 0.1 wt.% Ibuprofen, Aspirin and Erythromycin respectively, are plotted vs. temperature. For all the three drugs, R_H decreases with increase in temperature, with the increase becoming sharper at temperatures below 30°C. Polydispersities also increase substantially when the temperature is lowered and when drugs are incorporated in the micellar cores (Fig. 4.7(b)). Fig. 4.8(a) displays size distributions of the micellar aggregates at 60°C. Aspirin, which is the least hydrophobic drug used, forms the largest and most poly-disperse micelles at this temperature. At 25°C, however, Erythromycin incorporation leads to the formation of the largest and most polydisperse micelles (Fig. 4.8(b)). Greater drug hydrophobicity therefore ensures more compact packing of the drugs within the micellar cores at temperatures $\geq 40^\circ\text{C}$.

The morphologies of the micelles are therefore extremely sensitive to the molecular architectures and hydrophobicities of the inclusions within the micellar cores. The sizes of micelles along with polydispersity index (PDI) at various temperatures, incorporating varying quantities of drug solutes, are plotted in

4. ENCAPSULATION OF DRUGS IN PLURONIC F127 MICELLES: THE EFFECTS OF DRUG HYDROPHOBICITY, SOLUTION TEMPERATURE AND PH

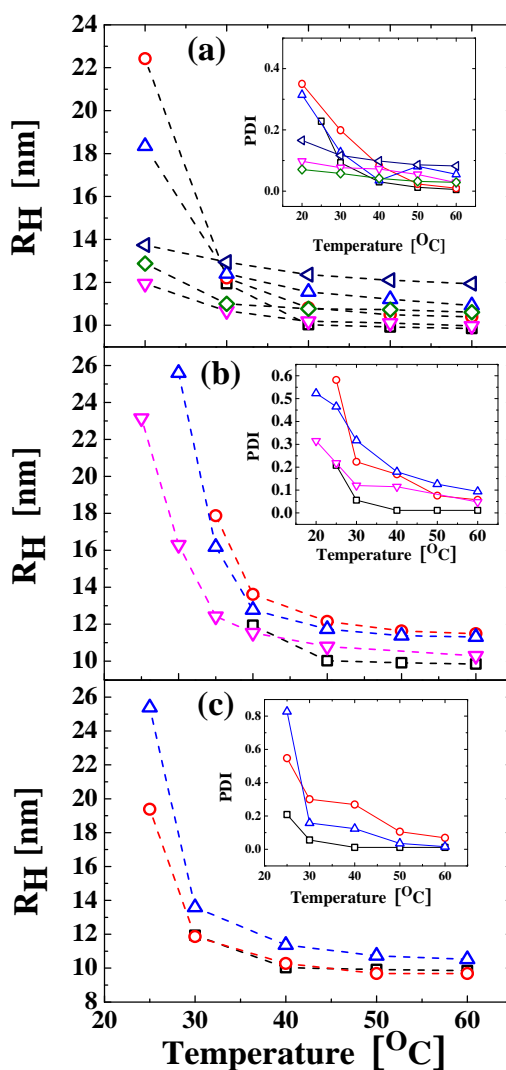


FIGURE 4.9: The mean hydrodynamic radius R_H and polydispersity index (PDI) for 5.26 wt% F127 solutions after the encapsulation of different concentrations of drugs are plotted vs. temperature in the main figures and in the insets respectively. The different symbols correspond to different quantities of added drugs: in : (a) Ibuprofen- 0 wt% (black squares), 0.1 wt% (red circles), 0.25 wt% (blue triangles), 0.5 wt% (pink down-triangles), 0.75 wt% (green diamonds), 1 wt% (violet left-triangles); (b) Aspirin- 0 wt % (black squares), 0.16 wt% (red circles), 0.3 wt% (blue triangles), 0.5 wt% (pink down-triangles), (c) Erythromycin- 0 wt%(black squares), 0.05 wt% (red circles), 0.1 wt% (blue triangles).

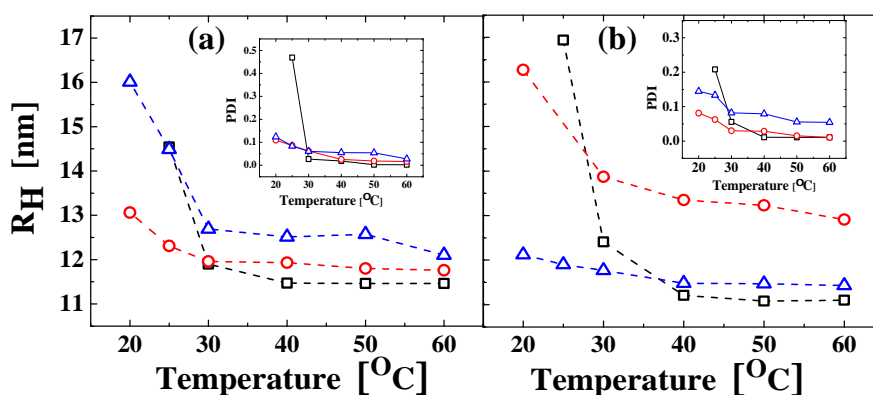


FIGURE 4.10: The mean hydrodynamic radius R_H and polydispersity index (PDI) vs. temperature for (a) 1.02 wt% and (b) 2.04 wt% F127 solutions after the encapsulation of different concentrations of drugs are shown in the main figures and insets respectively. The different symbols correspond to different quantities of added drugs: Ibuprofen- 0 wt% (black squares), 0.1 wt% (red circles), 0.25 wt% (blue triangles).

Fig. 4.9. For all the drugs, both R_H and PDI increase with decrease of temperature. The incorporation of drugs increases the radii of the micelles, in agreement with previous experiments involving the encapsulation of drug molecules in Pluronic block copolymer micelles [10–12]. It is, however, not possible to extract any systematic correlations between average micellar sizes and incorporated drug concentrations due to the very high micellar polydispersities. It is important to note that the small sizes of the drug-encapsulated micelles estimated here indicate that they may be sterilized by a simple filtration process and may be easily delivered to the blood stream through intravenous injection. All the experiments are repeated for the drug encapsulated micellar aggregates in solution, where Pluronic micelles are formed at a lower concentration of F127. In Fig. 4.10, R_H and PDI are plotted vs. temperature for 1.02 wt% and 2.04 wt% F127 solutions after the encapsulation of different concentrations of Ibuprofen. The data for the lower F127 concentrations also display the same trends as 5.26 wt% F127, with both R_H and PDI increasing with decrease in temperature.

To confirm the increased hydration of the micellar core due to decrease in

4. ENCAPSULATION OF DRUGS IN PLURONIC F127 MICELLES: THE EFFECTS OF DRUG HYDROPHOBICITY, SOLUTION TEMPERATURE AND PH

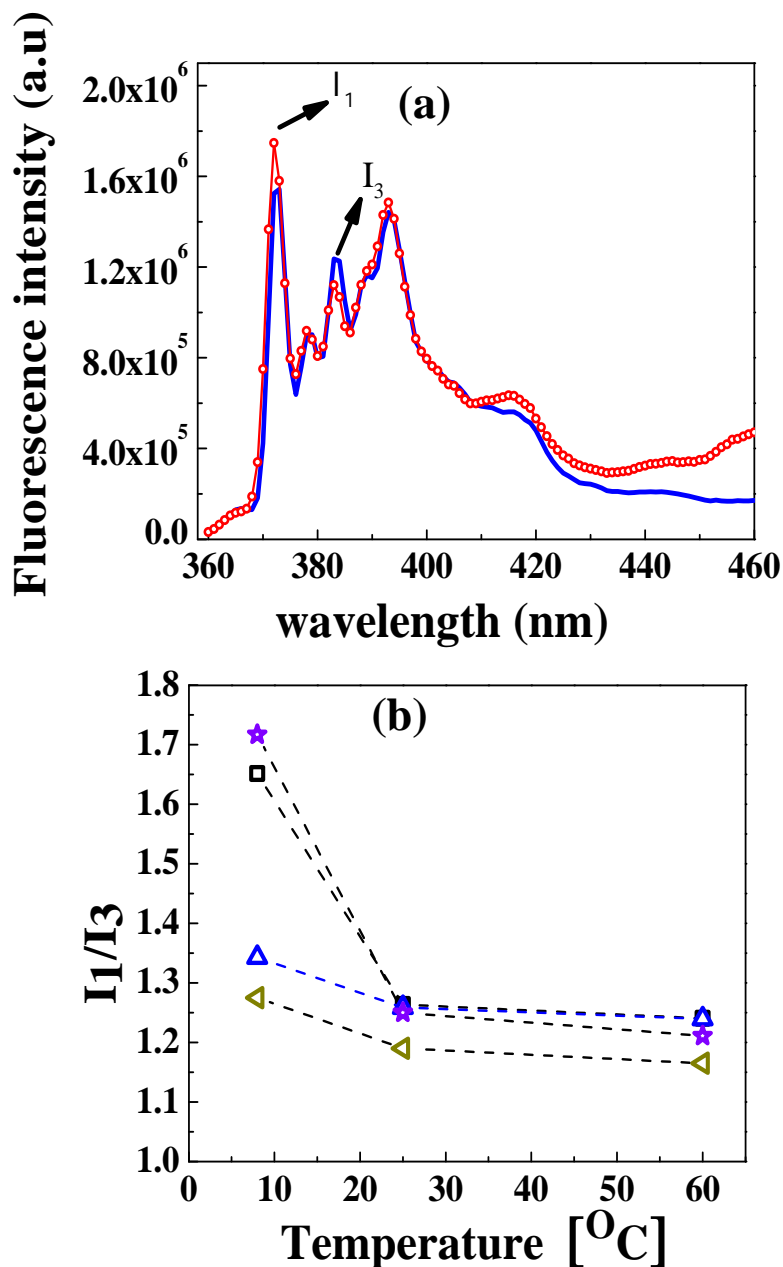


FIGURE 4.11: (a) Pyrene emission spectra for 5.26 wt% F127 solutions at 40°C (blue solid line) and 8°C (red circle-line). The variation of I_1/I_3 vs. temperature when 0 wt% Ibuprofen (black squares), 0.2 wt% Ibuprofen (blue triangles), 0.5 wt% Aspirin (green left-triangles) and 0.05 wt% Erythromycin (violet stars) are incorporated in F127 solutions, is plotted in (b).

solution temperature, fluorescence spectra of the samples are recorded using aromatic pyrene molecules as the fluorescent probe. This method is widely used to study micellization phenomena [25–30]. Pyrene molecules, being hydrophobic, stay encapsulated in the PPO cores of the micelles. The samples are excited at a wavelength of 339 nm with a bandwidth of 1 nm. The emission spectra, recorded at 40°C and 8°C, are shown in Fig. 4.11(a). In both these spectra, the first peak, I_1 , occurs at around 372 nm and the third peak, I_3 , occurs at around 383 nm.

Earlier studies have shown that the intensity ratio between the first and third emission peaks of the pyrene spectrum (I_1/I_3) depends upon the dipole moment of the solvent [29–31]. A significant enhancement in the intensity of the 0-0 vibronic band (which results in the I_1 peak) in the presence of a polar solvent has been reported. The I_3 peak, in contrast, is solvent-insensitive. A transition from a non-polar to a polar environment therefore results in a significant increase in the I_1/I_3 ratio in the pyrene emission spectrum. In Fig. 4.11(b), the ratios I_1/I_3 are plotted vs. temperature for different concentrations of drugs added to F127 solutions. For every sample, the ratio increases with decrease in temperature. This indicates an increase in the aqueous content of the micellar core region at lower temperatures. Increased solvent penetration into the micellar cores should result in a looser packing of drug molecules in the core. In the present case, this also increases the values of R_H at lower temperatures. The increase in R_H with decreasing temperature has already been reported in Figs. 4.7(a) and 4.9. For the samples with CMTs above 12°C (F127 micelles encapsulating 0 wt% Ibuprofen and 0.05 wt% Erythromycin, denoted by black squares and violet stars respectively in Fig. 4.11(b)), I_1/I_3 shows a very high value of around 1.7 at 8°C which indicates that the pyrene molecules are in a fully aqueous environment [31]. The high values of I_1/I_3 seen in our measurements for low drug encapsulation indicate that the pyrene molecules are

4. ENCAPSULATION OF DRUGS IN PLURONIC F127 MICELLES: THE EFFECTS OF DRUG HYDROPHOBICITY, SOLUTION TEMPERATURE AND PH

released into the aqueous environment at 8°C due to the breakup of the micelles into unimers. For the other samples with higher drug encapsulation, the increase in I_1/I_3 at lower temperature is much less, which indicates only a small amount of solvent penetration in the micellar core at these temperatures.

The addition of the weakly acidic Ibuprofen molecules to non-ionic F127 solutions results in a monotonic decrease in the sample pH. For example, the addition of 0.5 wt% Ibuprofen to a 5.26 wt% F127 solution decreases the solution pH from 7.00 to 4.65. Small amounts of NaOH are added to change the solution pH and systematic DLS measurements are next performed. The normalized intensity autocorrelation functions $C[\tau]$, obtained in DLS measurements with 5.26 wt% F127 solutions containing 0.5 wt% Ibuprofen at 40°C for different solution pH values, show fits to stretched exponential functions. The circles in Fig. 4.12(a) represent data at pH = 11.36. When the temperature is decreased to 15°C, the micelles dissociate into free unimers and $C[\tau]$ [squares in Fig. 4.12(a)] does not fit to a stretched exponential form. This is consistent with the high I_1/I_3 ratios obtained in fluorescence measurements on the same sample at 15°C [plotted in the inset of Fig. 4.12(a)]. The inset of Fig. 4.12(b) shows that as solution pH is changed between 4.65 and 11.36, $1/\langle \tau_R \rangle$, extracted from DLS data acquired 40°C, shows a power law dependence on q : $1/\langle \tau_R \rangle \approx q^\alpha$. Here, the exponent α gives information about the micellar dynamics. Fig. 4.12(b) plots the values of α and $1/\langle \tau_R \rangle$ vs. solution pH. At the low pH of 4.65, the power law fit gives $\alpha \approx 2$, suggesting that the system consists of homogeneous, spherical, diffusive structures. This is consistent with the results displayed in Fig. 4.5. With an increase in solution pH to 6.10, α increases to 2.57, indicating the presence of heterogeneous micellar structures in solution. This increase in α is accompanied by a simultaneous decrease in $1/\langle \tau_R \rangle$, which indicates the presence of bigger aggregates. When solution pH is increased to 11.36, a decrease of α to 2.19 and an increase in $1/\langle \tau_R \rangle$ are observed.

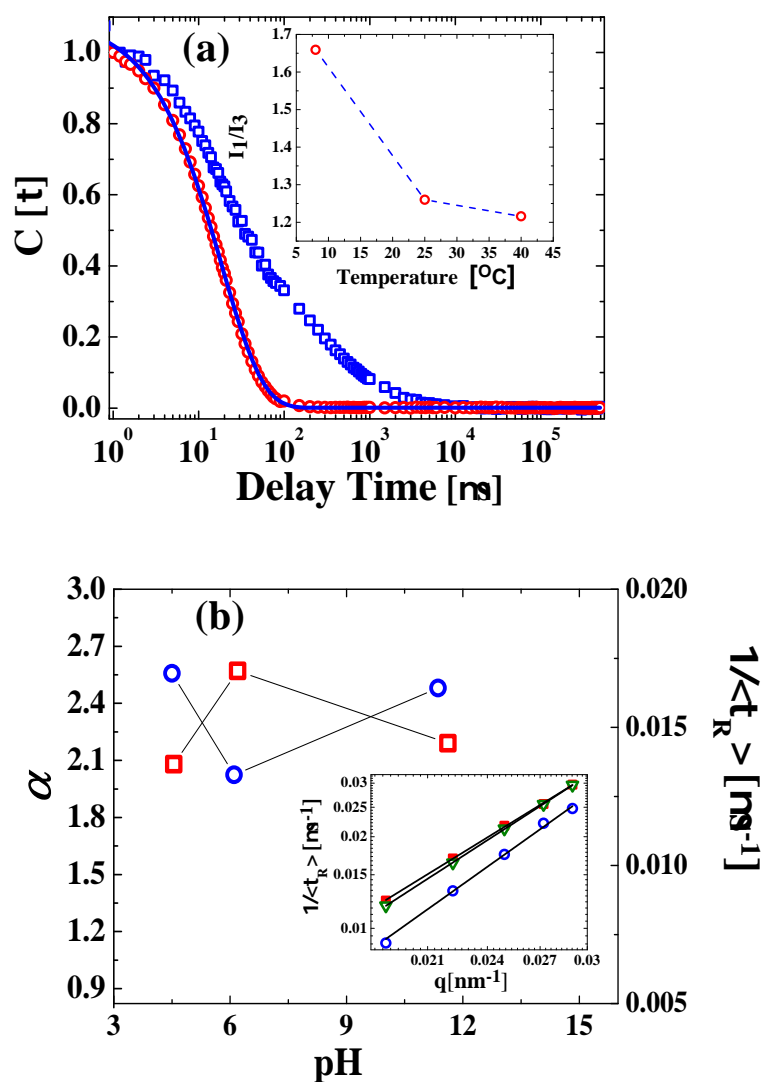


FIGURE 4.12: (a) The normalized intensity autocorrelation functions $C[\tau]$ for 5.26 wt% F127 solutions with 0.5 wt% ibuprofen at 40°C (circles) and 15°C (squares) respectively, when the solution pH is adjusted to 11.36, are shown. I_1/I_3 vs. temperature is plotted in the inset of (a). The values of α (red squares) and $1/\langle\tau_R\rangle$ (blue circles) at $\theta = 90^\circ$ and 40°C are plotted vs. solution pH in (b). Inset of (b) shows the plots of $1/\langle\tau_R\rangle$ vs. q and the corresponding fits to $1/\tau_R \approx q^\alpha$ (solid lines) at 40°C for different pH values: 4.65 (red squares), 6.10 (blue circles), 11.36 (green triangles).

As changing pH should not affect the non-ionic F127 micelles, the observed changes are brought about by the Ibuprofen molecules present in solution. With increase in solution pH, the Ibuprofen molecules in the micellar core are ionized [14, 15]. The repulsive interactions within the core leads to the formation of bigger, more anisotropic micelles at pH = 6.10. When the pH of the system is further increased to 11.36, the Ibuprofen molecules, which are fully ionized, are released from the micellar cores to the aqueous medium due to their enhanced water solubility. The encapsulation of drug molecules is not favored under these conditions and pure F127 micelles coexist in solution with free drug molecules. This results in the observed decrease in α . It is to be noted here that the hydrodynamic radii R_H of the micelles estimated in DLS measurement is 10.4 nm at $T = 40^\circ\text{C}$ at pH = 11.36, almost identical to the value extracted when no drugs are added (Figs. 4.7(a) and 4.9). Furthermore, by observing changes in the shapes of $C[\tau]$ from stretched exponential to non-exponential as temperature is decreased, the CMT of the sample at pH = 11.36 is estimated to be 24°C , the value expected for pure F127 micellar solutions. This observation is similar to the findings of Scherlund *et al.*, who observed that if the the active ingredients (drugs) are mostly in ionized form at a certain pH, the CMT of the sample is almost the same as that of pure F127 micellar systems [4]. The release of drugs at high pH was previously also reported for Flurbiprofen-encapsulated P103 solutions [15].

4.4 Conclusion

In this work, three different drugs, Ibuprofen, Aspirin and Erythromycin, are encapsulated in F127 micelles in aqueous solution. Cryo-SEM imaging shows the presence of globular structures even after drug-encapsulation. The drug molecules, when added above a specific threshold concentration C_t , enhances

the stability of the micellar phase over a broad temperature range. DLS experiments are performed on the drug-encapsulated micellar systems to determine changes in the hydrodynamic radii and micellar polydispersities. The average hydrodynamic radii of the micelles calculated here are seen to increase upon drug incorporation, with the polydispersity being inversely correlated to the drug hydrophobicity at the higher temperatures. The hydrodynamic radii of the micelles increase with decrease in temperature. This is consistent with data presented in [10, 11]. The observed increase in micellar sizes observed when temperature is lowered is accompanied by an increase in the hydration of the micellar core and is verified by pyrene fluorescence spectra measurements. Increasing the temperature excludes the solvent from the micellar core due to enhanced core hydrophobicity and results in more compact micelles.

The drug-encapsulated micelles also show a strong pH dependence. When the solution pH is increased from 4.65 to 6.10, the ionization of the drug molecules leads to the formation of larger micelles. Increasing the pH to 11.36 triggers the release of drug molecules into the solvent.

Drug-incorporated F127 micelles have enormous potential as drug carriers in the area of nanomedicine [9]. However, before these formulations are made available commercially, several clinical and scientific issues regarding toxicity and stability still need to be addressed.

References

- [1] E. V. Batrakova and A. V. Kabanov, *J. Controlled Release* **130**, 98 (2008).
- [2] G. S. Kwon and K. Kataoka, *Adv. Drug Del. Reviews* **16**, 295 (1995).
- [3] Y. Kakizawa and K. Kataoka, *Adv. Drug Del. Reviews*, **54**, 203 (2002).
- [4] M. Scherlund, A. Brodin and M. Malmsten, *Int. J. of Pharmaceutics* **211**, 37 (2000).
- [5] A. V. Kabanov, P. Lemieux, S.; Vinogradova and V. Alakhovb, *Adv. Drug Del. Reviews* **54**, 223 (2002).
- [6] J. Israelachvili, *Proc. Natl. Acad. Sci.* **94**, 8378 (1997).
- [7] K. Dorn, G. Hoerpel and H. Ringsdorf, *Bioactive Polymeric Systems: an overview* (Plenum, New York, 1985).
- [8] V. P. Torchilin, *J. Controlled Release*, **73**, 137 (2001).
- [9] S. M. Moghimi and A. C. Hunter, *Trends in Biotech.* **18**, 412 (2000).
- [10] P. K. Sharma and S. R. Bhatia, *Int. J. Pharmaceutics* **278**, 361 (2004).
- [11] P. K. Sharma, M. J. Reilly, D. N. Jones, P. M. Robinson and S. R. Bhatia, *Colloid Surfaces B: Biointerfaces* **61**, 53 (2008).

-
- [12] B. Foster, T. Cosgrove and Y. Espidel, *Langmuir* **25**, 6760 (2009).
- [13] S. Alexander, T. Cosgrove, S. W. Prescott and T. C. Castle *Langmuir* **27**, 8054 (2011).
- [14] B. Foster, T. Cosgrove and B. Hammouda, *Langmuir*, **25**, 6767 (2009).
- [15] S. Alexander, W. M. de Vos, T. C. Castle, T. Cosgrove and W. Prescott, *Langmuir*, **28**, 6539 (2012).
- [16] A. G. Mitchell and J. F. Broadhead, *Jour. of Pharmaceutical Sci.*, **56**, 1261 (1967).
- [17] U. Domanska, A. Pobudkowska, A. Pelczarska and P. Gierycz, *J. Phys. Chem. B* **113**, 8941 (2009).
- [18] K. Gerzon, R. Monahan, O. Weayer, M. V. Sigal Jr. and P. F. Wiley, *J. Am. Chem. Soc.* **78**, 6412 (1956).
- [19] O. A. H. Jones, N. Voulvoulis and J. N. Lester, *Water Research* **36**, 5013 (2002).
- [20] R. Nagarajan, *Colloids Surf. B* **16**, 55 (1999).
- [21] L. Guo, R. Colby and P. Thiyagarajan, *Phys. B*, **385**, 685 (2006).
- [22] G. Wanka, H. Hoffmann and W. Ulbricht, *Macromol.*, **27**, 4145 (1994).
- [23] M. Bohorquez, C. Koch, T. Trygstad and N. Pandit, *J. Colloid and Interface Science* **216**, 34 (1999).
- [24] C. P. Lindsey and G. D. Patterson, *J. Chem. Phys.*, **73**, 3348 (1980).
- [25] M. Wilhelm, C. L. Zhao, Y. Wang, R. Xu, M. A. Winnik, J. L. Mura, G. Riess and M. D. Croucher **24**, 1033 (1991).
- [26] A. Yekta, J. Duhamel, P. Brochard, H. Adiwidjaja and M. A. Winnik **26**, 1829 (1993).

- [27] I. Astafieva, X. F. Zhong and A. Eisenberg, *Macromol.* **26**, 7339 (1993).
- [28] W. Binana-Limbele and R. Zana, *Macromol.* **20**, 1331 (1987).
- [29] A. Nakajima, *J. Luminescence* **11**, 429 (1976).
- [30] A. Nakajima, *J. Mol. Spect.* **61**, 467 (1976).
- [31] K. Kalyanasundaram and J. K. Thomas, *J. Am. Chem. Soc.* **99**, 2039 (1977).

5

Formation and Rupture of Ca^{2+} Induced Pectin Biopolymer Gels

5.1 Introduction

Pectins are major components of the primary plant cell wall, where they sometimes comprise 30-35% of the cell wall dry weight [1]. Ca^{2+} ions in the plant cell wall form pectin gel structures *via* ionic crosslinking. Ca^{2+} , which plays a crucial role in determining the structural rigidity of the cell wall, is a crucial regulator of growth and development in plants [2]. Low concentrations of Ca^{2+} result in cell walls that are more flexible and therefore easily ruptured, while high concentrations of Ca^{2+} increase the rigidity the wall, making it less plastic [3]. To understand cell wall behavior, it is important to understand the formation and rupture of pectin gels. Furthermore, knowledge of the mechanical properties of pectin gels has practical implications in the food industry,

5. FORMATION AND RUPTURE OF Ca^{2+} INDUCED PECTIN BIOPOLYMER GELS

mainly in the production of jams, preservatives *etc.* [4]. Ion-induced hydrogels are also used for many applications related to pharmaceuticals and for tissue engineering, glucose transport, cell encapsulation, drug delivery *etc.* [5–8]. The various applications of pectin gels, therefore, necessitate a detailed study of their formation and mechanical stability under different conditions.

The mechanical properties of these ion induced hydrogels can be improved by the addition of block copolymers in bioengineering applications [9]. Calcium-ion induced gelation of LM pectin depends upon various parameters like pectin concentration, salt concentration, the degree of methylation of pectin molecules, the pH and temperature of the solution. The effects of these parameters on the gelation process of pectin solutions have been studied by rheological methods [10–17], dynamic light scattering (DLS) [18, 19], nuclear magnetic resonance (NMR) [20] and circular dichroism [21, 22]. Conductometric and potentiometric studies show that decreasing the degree of methylation of pectin molecules and the ionic strength of the solution can increase the affinity of pectin molecules towards Ca^{2+} ions. This results in a decrease in the amount of calcium chloride required to obtain a sol-gel transition [10, 23]. The sol-gel transition in solutions of pectin and other biopolymer molecules can also be triggered by irradiating the samples with ultraviolet radiation [24]. Durand *et al.* reported the gelation times of pectin solutions for various pectin concentrations and stoichiometric ratios of salt and pectin and estimated sol-gel diagrams for calcium-pectin systems for a range of calcium levels, solution temperatures and pectin concentrations [12]. Lootens *et al.* showed that the lowering of the solution pH weakens the Ca^{2+} induced gel formation process [15]. DLS measurements exhibit an increase in the characteristic relaxation times of pectin solutions when the concentration of Ca^{2+} in solution is increased [18].

In this work, the microscopic dynamics of gelling LM pectin solutions are investigated by measuring intensity autocorrelation functions in DLS measurements. The relaxation timescales of the samples, which are extracted from

the decays of the autocorrelation functions obtained from the samples before gelation, are compared with their bulk viscosities. Next, the effects of applied stresses on pectin gels of various strengths are studied and the critical stresses required to break the gel networks are estimated using rheological measurements. The dependence of the critical stress on the pectin gel strength is investigated systematically by changing the CaCl_2 concentration. The results are explained in terms of the fractal nature of the pectin gel structure using a scaling theory that was first introduced by Shih *et. al.* to describe the elastic properties of colloidal gels [25]. It should be noted that while the colloidal gels investigated in this work [25] were formed by increasing the volume fraction of boehmite alumina particles of Catapal and Dispal respectively, our work studies the process of ion-mediated gelation of pectin solutions that is triggered by increasing the CaCl_2 concentration in solution. Analysis of our experimental data shows a strong power-law dependence of the elasticity of individual pectin flocs on the added salt concentration. Our data suggests that when pectin and salt concentrations are both increased, the number of aggregates increases simultaneously with the density of crosslinks and that the inter-aggregate links are stronger than the intra-aggregate links.

5.2 Sample preparation

Pectin, a 20-34% esterified potassium salt extracted from citrus fruit and calcium chloride anhydrous (molecular weight 111 g/mol) are purchased from Sigma-Aldrich and used as received without further purification. Stock solutions of calcium chloride of appropriate concentrations are prepared. Pure pectin solutions are prepared by dissolving appropriate amounts of pectin in deionized and distilled Millipore water and by stirring the mixture vigorously with a magnetic stirrer. Stock solutions of CaCl_2 of known concentrations are mixed with pure pectin solutions to prepare gel samples of several strengths.

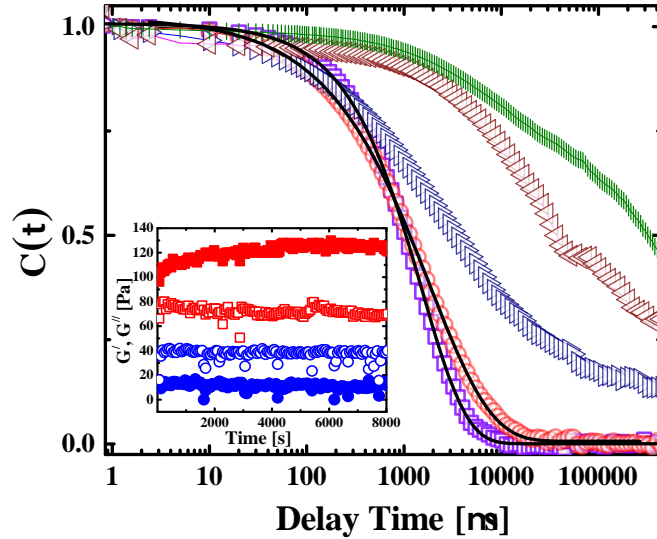


FIGURE 5.1: Plots of the normalized autocorrelation functions $C(\tau)$ vs. delay time τ at scattering angle $\theta = 90^\circ$ for 2.5 g/L pectin solutions at 25°C with different CaCl_2 concentrations: 0 mM (violet squares), 2 mM (red circles), 6 mM (blue right triangles), 8 mM (brown left triangles), 10 mM (green vertical lines). The stretched exponential fits to the data for 0 mM and 2 mM CaCl_2 concentrations are shown by solid black lines. In the inset, the time evolutions of the storage moduli G' (solid symbols) and the loss moduli G'' (hollow symbols), after the addition of 2 mM CaCl_2 (blue circles) and 6 mM CaCl_2 (red squares) to 2.5 g/L pectin solution at 25°C , are plotted.

The mixtures are stirred overnight before loading the samples for the experiments. All experiments are performed at 25°C .

5.3 Results and Discussions

5.3.1 Gel Formation:

Systematic DLS studies are performed with aqueous solutions of pectin of concentration 2.5 g/L with different concentrations of added CaCl_2 salt. Fig. 5.1 shows the plots of the normalized intensity-intensity autocorrelation functions

$C(\tau)$ vs. delay times τ for different CaCl_2 concentrations. It is observed that for pectin solutions with low or no salt, the $C(\tau)$ plots show complete decays. To estimate the distributions of relaxation rates, the correlation decays are fitted to stretched exponential functions

$$C(\tau) \sim \exp(-\Gamma_R \tau)^\beta \quad (5.1)$$

where Γ_R , the relaxation rate, is the inverse of a relaxation time τ_R and $\beta \leq 1$ is the stretching exponent. The mean relaxation time $\langle \tau_R \rangle$ for a particular scattering angle is estimated using the following relation [26]

$$\langle \tau_R \rangle = \tau_R / \beta * \Gamma(1/\beta) \quad (5.2)$$

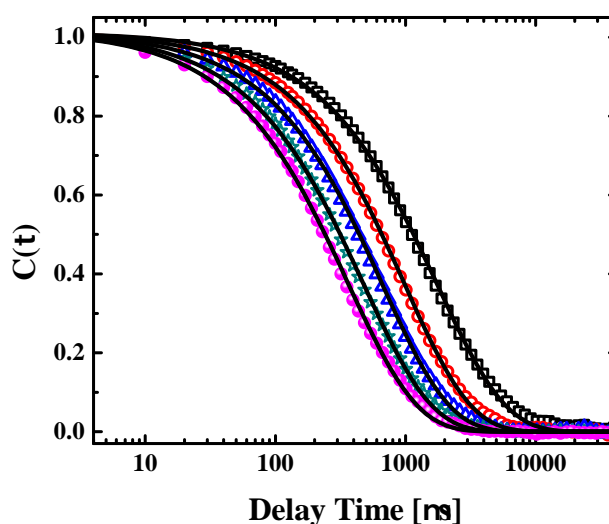


FIGURE 5.2: Plots of the normalized autocorrelation functions $C(\tau)$ vs. delay times τ for 2.5 g/L pectin solutions at 25°C containing 1 mM CaCl_2 for different scattering angles: 60° (black squares), 75° (red circles), 90° (blue up-triangles), 105° (green stars) and 120° (magenta solid circles). The stretched exponential fits to the data are shown by solid black lines.

5. FORMATION AND RUPTURE OF Ca^{2+} INDUCED PECTIN BIOPOLYMER GELS

where $\Gamma(1/\beta)$ is the Euler gamma function [26].

As the CaCl_2 concentration, and hence the gel strength, is increased, a systematic slowdown in the decay times of the correlation functions is observed, with the correlation plots eventually showing incomplete decays at the highest salt concentrations. The observed transition of the sample to a regime of non-ergodic dynamics beyond a threshold salt concentration marks the onset of the gelation process [27]. The concentration of CaCl_2 , above which an incomplete decay in $C(\tau)$ is observed in the present experiments, is assigned as the critical concentration ' C_{cr} ' of CaCl_2 salts required for the gelation of pectin solutions. By studying the measured autocorrelation decays, C_{cr} is estimated to lie between 3.5-4 mM for the 2.5 g/L pectin solutions. Gel formation, due to an increase in CaCl_2 concentration above C_{cr} , is confirmed by plotting the time evolutions of the rheological moduli. It is seen from the inset of Fig. 5.1 that when the CaCl_2 concentration (2 mM data represented by circles) lies below C_{cr} , the sample shows predominantly viscous response to small oscillatory strains at the angular frequency that has been probed here (1 rad/sec), with the loss modulus G'' always higher than the storage modulus G' . When the CaCl_2 concentration is above C_{cr} (6 mM data represented by squares), $G' \gg G''$ from the start of the measurement. The structure of the sample with 6 mM salt is, therefore, far more rigid than the one with 2 mM salt, with gelation being initiated immediately after the addition of salt in this case.

Changes in the wave vector dependence of the sample dynamics due to the addition of CaCl_2 are explored by studying the fits to the stretched exponential correlation decays (Eqn. 5.1) at different scattering angles. $C(\tau)$ vs. τ data for several scattering wavevectors q is shown in Fig. 5.2. In the inset of Fig. 5.3, the inverse of the mean relaxation times $\langle \tau_R \rangle$, extracted from the stretched exponential fits of $C(\tau)$ for samples with CaCl_2 concentrations below

C_{cr} , are plotted vs. q . This data is fit to the relation

$$1/\langle \tau_R \rangle \approx q^\alpha \quad (5.3)$$

The power law exponents α (squares), extracted from fits to Eqn. 5.3, and the stretching exponents β (solid circles), obtained from fits to Eqn. 5.1, are plotted in Fig. 5.3 for different CaCl_2 concentrations. At low CaCl_2 concentrations, $\alpha \approx 2$ and $\beta \approx 0.9$. This indicates the presence of pectin flocs of approximately equal sizes diffusing freely in the solution. With increase in CaCl_2 concentration, α shows a gradual increase from 2. This points to an increase in the spatial inhomogeneity of the system. It is observed that the polydispersity in

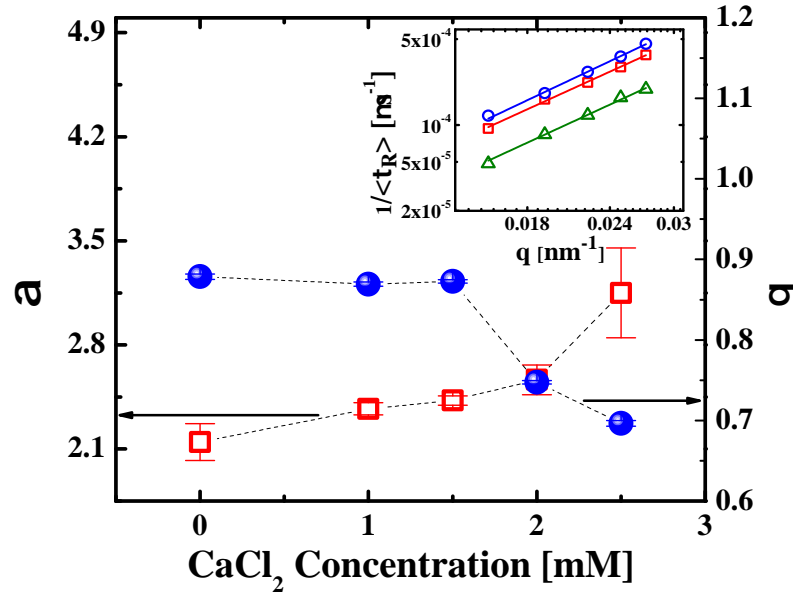


FIGURE 5.3: Plots of the power law exponents α (extracted from the fits of the mean relaxation time $\langle \tau_R \rangle$ to Eqn. 5.3 and represented by \square) and the stretched exponents β (\bullet) (extracted from fits of $C(\tau)$ vs. τ to Eqn. 5.1 and represented by solid circles), vs. CaCl_2 concentration at 25°C for 2.5 g/L pectin solutions. The inset shows the plots of $1/\langle \tau_R \rangle$ vs. q for different CaCl_2 concentrations : 0 mM (blue circles), 1 mM (red squares), 2 mM (green triangles) and the corresponding fits to Eqn. 5.3 (fits are represented by solid lines).

5. FORMATION AND RUPTURE OF Ca^{2+} INDUCED PECTIN BIOPOLYMER GELS

the floc sizes increases simultaneously with the increase in α as CaCl_2 concentration is increased, with β dropping to values much lower than 1 for the highest CaCl_2 concentrations used in this work. A stronger-than-diffusive q -dependence of the estimated relaxation time and $\beta < 1$ with increasing pectin and divalent salt concentrations have been observed in LM-pectin solutions in earlier reports [18, 19]. Furthermore, it has been verified that the relation $\alpha = \frac{2}{\beta}$ seen in these earlier reports holds in the salt concentration range 0-2.5 mM investigated in this work.

The mean relaxation times $\langle \tau_R \rangle$ of pectin gels (represented by squares)

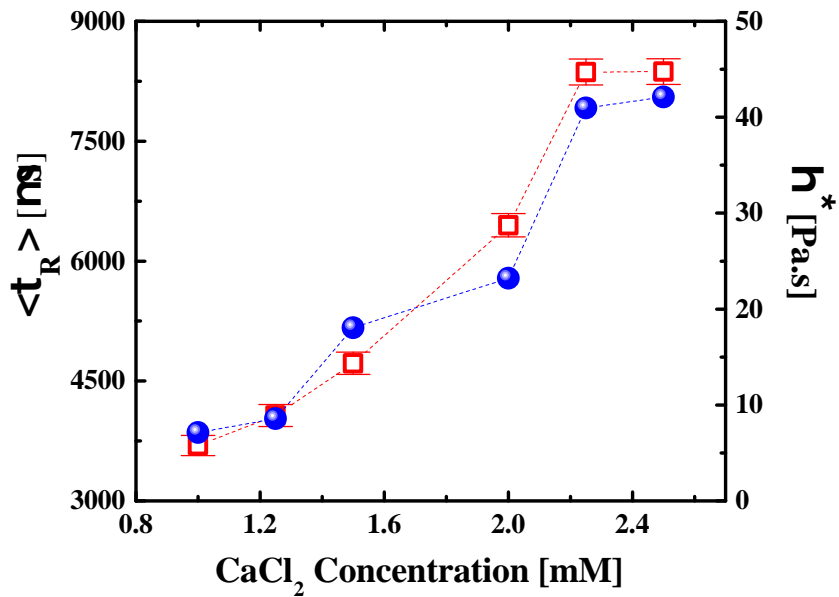


FIGURE 5.4: Plot of the mean relaxation time $\langle \tau_R \rangle$ (\square) and complex viscosity η^* (\bullet) vs. CaCl_2 concentration for gelling pectin solutions (concentration of pectin is kept fixed at 2.5 g/L) at 25°C.

show a monotonic increase when plotted vs. CaCl_2 concentration (Fig. 5.4). The pectin floc sizes therefore increase with increasing salt, causing the system to become increasingly heterogeneous and resulting in the observed dynamical slowdown. Clearly, as the CaCl_2 concentration is increased, the increased availability of Ca^{2+} ions in biopolymer pectin solutions increases the

cross-link density between pectin molecules, thereby accelerating the formation of polydisperse pectin flocs. A further increase in the concentration of CaCl_2 towards the critical value C_{cr} initiates the formation of links between the pectin flocs, with a percolating gel network being formed at CaCl_2 concentrations greater than C_{cr} . Due to an increase in the number of links with increasing CaCl_2 concentration, this dynamical slowing down is accompanied by an increase of the complex viscosity η^* . This is shown in Fig. 5.4 (circles). The

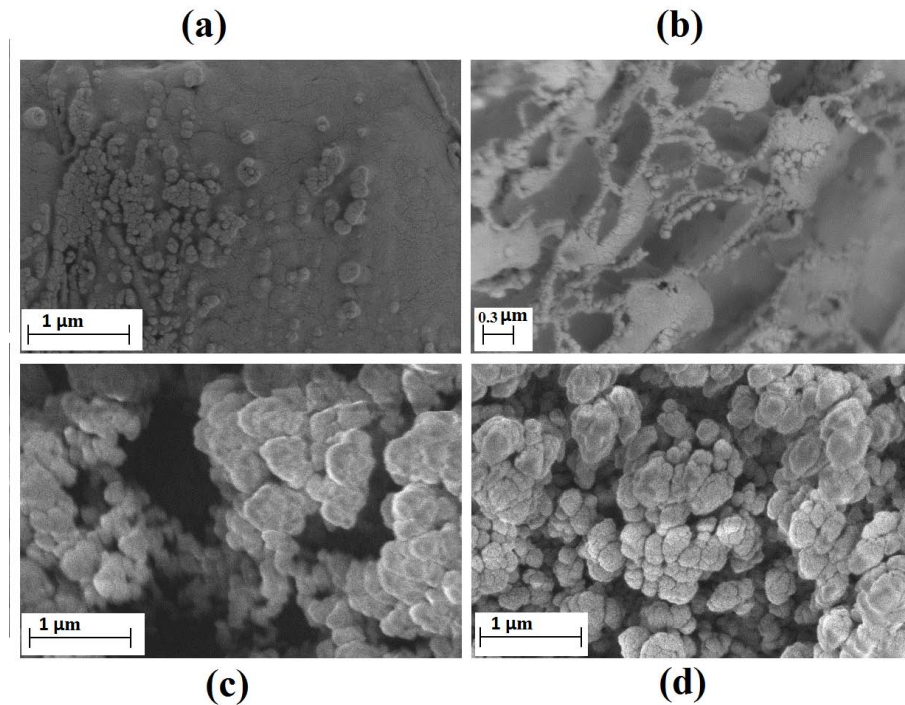


FIGURE 5.5: Cryo-SEM images for 2.5 g/L pectin with different CaCl_2 concentrations: (a) 1 mM, (b) 3.5 mM, (c) 6 mM and (d) 10 mM.

complex viscosity η^* is defined as $\eta^* = \frac{(G'^2 + G''^2)^{1/2}}{\omega}$, where G' and G'' are the elastic and viscous moduli respectively, measured at an angular frequency $\omega = 1$ rad/s and at a strain amplitude $\gamma = 0.5\%$ [28].

The existence of flocs in pectin solutions and the formation of links between flocculated structures at higher salt concentrations is confirmed from cryo-SEM images displayed in Fig. 5.5. In Fig. 5.5(a), which shows an image of a pectin sample with CaCl_2 concentration below C_{cr} , small, polydisperse

5. FORMATION AND RUPTURE OF Ca^{2+} INDUCED PECTIN BIOPOLYMER GELS

and un-interconnected pectin flocs are observed. Near the critical concentration C_{cr} (an image of a sample in which 3.5 mM CaCl_2 added to 2.5 g/L pectin solutions is shown in Fig. 5.5(b)), an increase in the average floc size and a development of inter-floc links are observed. The formation of links (CaCl_2 bridges) between pectin molecules results in gelation and the observed divergence of relaxation time scales seen in Fig. 5.1. Cryo-SEM images of pectin samples containing CaCl_2 at even higher concentrations (6 mM and 10 mM data are plotted in Fig. 5.5(c) and 5.5(d) respectively) show the presence of bigger flocs and a remarkable increase in the density of interlinks. It is to be noted here that while the sizes of the pectin flocs do not increase substantially in the salt concentration regime $C \gg C_{cr}$, the density of interlinks increases sharply with increasing CaCl_2 concentration.

The SEM images presented here provide direct evidence of the growth of flocs with increasing CaCl_2 concentration, followed by the percolation of the flocs to form gel networks, and are in agreement with the DLS data presented earlier. As pectin gels are formed due to the development of interlinks between flocs of different sizes, static light scattering (SLS) measurements are performed to confirm the fractal nature of the pectin gels. In these measurements, the scattered intensity $I(q)$ is plotted vs. wave vector q for pectin solutions containing CaCl_2 at concentrations that lie above the critical gelation threshold C_{cr} . The fractal structure of the pectin gel results in power law decays of $I(q)$ with q according to the following relation [29]

$$I(q) \approx q^{-D} \quad (5.4)$$

where D is the fractal dimension of the gel. $I(q)$ vs. q data has been recorded for 2.5 g/L pectin solutions containing CaCl_2 in the concentration range 5-10 mM. The data for the pectin gel containing 6 mM CaCl_2 is plotted in the inset of Fig. 5.6. The exponent of the power-law fit to the decay (solid line in the

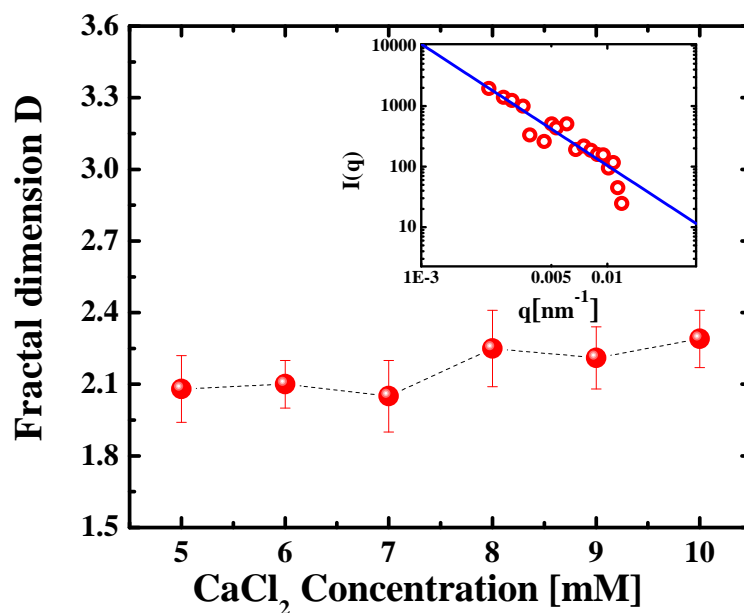


FIGURE 5.6: Fractal dimensions D of the pectin gels are plotted vs. CaCl_2 concentration for 2.5 g/L pectin solutions containing CaCl_2 at concentrations greater than C_{cr} . In the inset, $I(q)$ vs. q plot and the corresponding fit to Eqn. 5.4 (solid line) for a 2.5 g/L pectin solution containing 6 mM CaCl_2 at 25°C, are plotted.

inset) gives the fractal dimension D of the gel. The fractal dimensions, obtained from power-law decay fits for the entire salt concentration range above C_{cr} investigated here, are plotted in Fig. 5.6. D is seen to always lie between 1.9 and 2.4, suggesting that size-polydisperse pectin gel flocs are formed by a process of three-dimensional reaction-limited aggregation (RLA) [30] in this CaCl_2 concentration range. Unlike in globular protein gels, where the aggregation process changes from reaction-limited to diffusion-limited with increase in ionic concentration [31], the approximately constant values of D reported here indicates that the interaction mechanism triggering the gelation of pectin does not change within the experimental range of CaCl_2 concentrations investigated here. This is in sharp contrast to the ion-mediated gelation of globular proteins, where the probability of collisions between protein molecules and the subsequent formation of interlinks increase rapidly at higher ionic strengths due to

5. FORMATION AND RUPTURE OF Ca^{2+} INDUCED PECTIN BIOPOLYMER GELS

the increased shielding of surface charges on the protein molecules.

5.3.2 Gel Rupture:

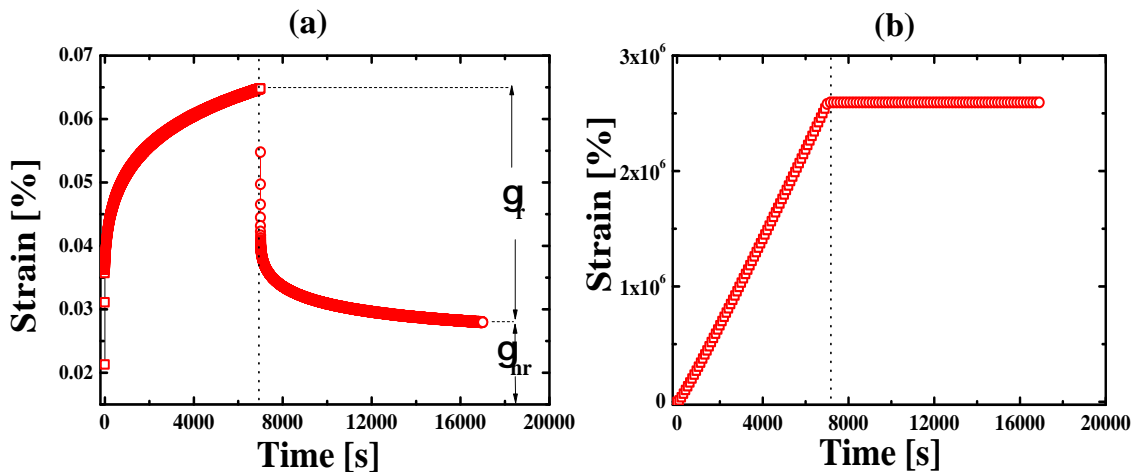


FIGURE 5.7: Strain evolution during creep and recovery tests for 2.5 g/L pectin gel containing 6 mM CaCl_2 at 25°C. Data for applied stresses 0.4 Pa and 2 Pa are plotted in (a) and (b) respectively. The vertical dotted line denotes the time when the stress is set to zero.

To complement the data on pectin gel formation due to the addition of CaCl_2 , rheological experiments are performed to study the rupture of these gels following the application of shear stresses. Creep and recovery tests are performed to investigate the response of the cross-linked pectin flocs to externally-imposed shear stresses. It is observed that the rheological response of pectin gels is very strongly dependent upon the amplitude of the applied stress. In Fig. 5.7(a), the development of strain for a pectin gel network, when a low constant stress ($\sigma = 0.4$ Pa) is applied for 7200 seconds to a 2.5 g/L pectin gel with 6 mM CaCl_2 , is plotted. It is seen in Fig. 5.7(a) that the sample deforms almost immediately after the application of the stress. After an initial instantaneous deformation, the strain continues to develop slowly with

time and reaches a value of γ_M after 7200 seconds. When the applied stress is removed from the sample, it is observed that most of the strain recovers almost immediately. This is followed by a slow and continuous process of strain recovery, with the strain eventually reaching a plateau value γ_{nr} . Here, γ_{nr} is a measure of the irreversible or permanent strain incorporated in the sample during these creep experiments. The recoverable strain γ_r in these experiments is calculated as $\gamma_r = (\gamma_M - \gamma_{nr})$. When the applied stress is above a critical value, the deformation increases linearly during the time period of stress application. This is shown in Fig. 5.7(b). When the applied stress is removed, the strain does not recover at all. This signals the rupture of the Ca^{2+} induced pectin gel networks at these high stresses.

The ratios of the recoverable and non-recoverable strains (γ_r/γ_{nr}) estimated in these experiments quantify the responses of the gel networks to applied

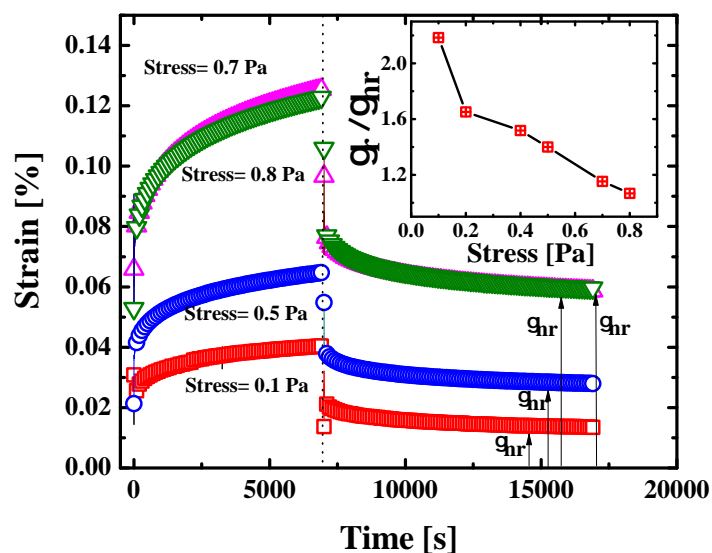


FIGURE 5.8: Plots of strain-evolutions during creep and recovery tests for 2.5 g/L pectin gels containing 6 mM CaCl_2 at different applied stresses: 0.1 Pa (red squares), 0.5 Pa (blue circles), 0.7 Pa (green down-triangles) and 0.8 Pa (magenta up-triangles). The vertical dotted line denotes the time when the stress is set to zero. In the inset, the plot of γ_r/γ_{nr} vs. applied stress for 2.5 g/L pectin gel containing 6 mM CaCl_2 is shown.

5. FORMATION AND RUPTURE OF Ca^{2+} INDUCED PECTIN BIOPOLYMER GELS

stresses. Creep and recovery plots for different applied stresses are shown in Fig. 5.8, and the ratio γ_r/γ_{nr} is calculated for each experiment. It is observed in the inset of Fig. 5.8 that γ_r/γ_{nr} decreases with increase in the applied stress. The gel network therefore weakens with increase in applied stress, with a permanent strain being built into the gel structure. This eventually leads to the rupture of the gel network, resulting in the behavior observed in Fig. 5.7(b). The applied stress, above which the creep behavior of the type shown in Fig. 5.7(a) changes to a fluid-like response as seen in Fig. 5.7(b), is assigned as a critical stress (σ_{critical}) required for completely rupturing the gel network. The existence of a critical stress is a common feature of jammed soft materials and is related to the strength of the junctions between the clusters [32]. The value of σ_{critical} for a 2.5 g/L pectin gel with 6 mM CaCl_2 is estimated to be approximately 0.81 Pa. The relevant plots are shown in Fig. 5.9.

Next, the values of σ_{critical} are estimated from creep and recovery mea-

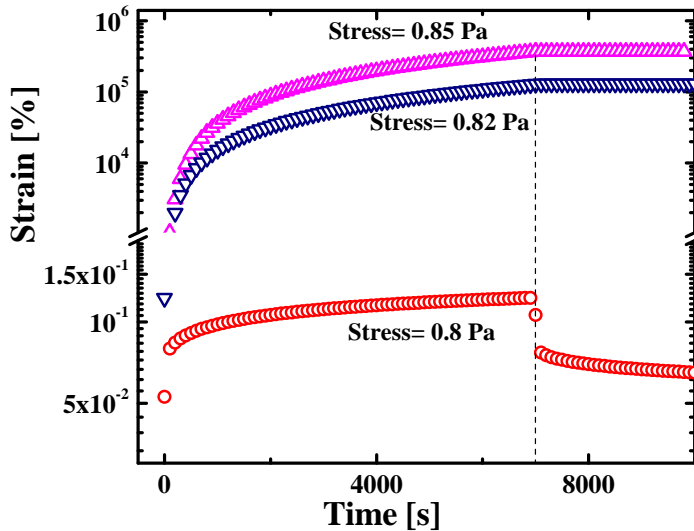


FIGURE 5.9: The critical stress σ_{critical} is estimated by plotting the strain variation during creep and recovery tests for 2.5 g/L pectin gel samples containing 6 mM CaCl_2 due to the application of different stresses: a) 0.8 Pa (red circles), b) 0.82 Pa (navy down-triangles) and c) 0.85 Pa (magenta up-triangles). This indicates that $\sigma_{\text{critical}} \sim 0.81$ Pa. The vertical dotted line denotes the time when the stress is set to zero.

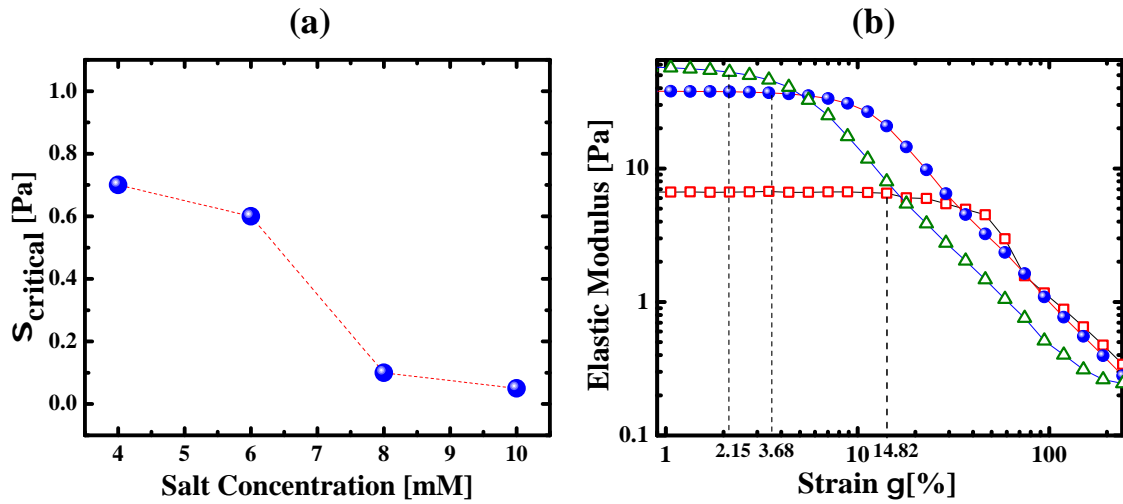


FIGURE 5.10: (a) Plot of critical stress (σ_{critical}) (denoted by \bullet) vs. CaCl_2 concentration for 2.5 g/L pectin solutions with added salt. (b) Plot of G' vs. oscillatory strain amplitude γ (angular frequency ω fixed at 1 rad/s) for 2.5 g/L pectin solutions with CaCl_2 concentrations of 5mM (red squares), 8mM (blue circles) and 10mM (green triangles) is shown. The start of non-linearity in each case is shown by vertical dotted lines.

measurements for 2.5 g/L pectin solutions containing several different CaCl_2 concentrations. This is plotted in Fig. 5.10(a). It is observed that σ_{critical} decreases monotonically with added CaCl_2 concentration. To understand the effects of CaCl_2 on gel elasticity and the observed decrease in σ_{critical} , amplitude sweep experiments are performed for 2.5 g/L pectin gels with different concentrations of added CaCl_2 . In these experiments, the amplitude of the applied oscillatory strain γ is increased logarithmically from 0.1% to 100%, keeping the angular frequency ω constant at 1 rad/second at room temperature. In Fig. 5.10(b), the elastic modulus G' is plotted vs. γ for 2.5 g/L pectin solutions containing different amounts of CaCl_2 . For the lowest γ values, the elastic modulus show a linear regime with $G' \approx G'_0$. This is followed by a strongly non-linear response with increasing γ , where G' decreases rapidly from G'_0 . The loss modulus G'' , measured simultaneously with G' , is plotted vs. γ in Fig. 5.11 for 2.5 g/L pectin solutions containing different amounts of CaCl_2 . The loss modulus shows a

5. FORMATION AND RUPTURE OF Ca^{2+} INDUCED PECTIN BIOPOLYMER GELS

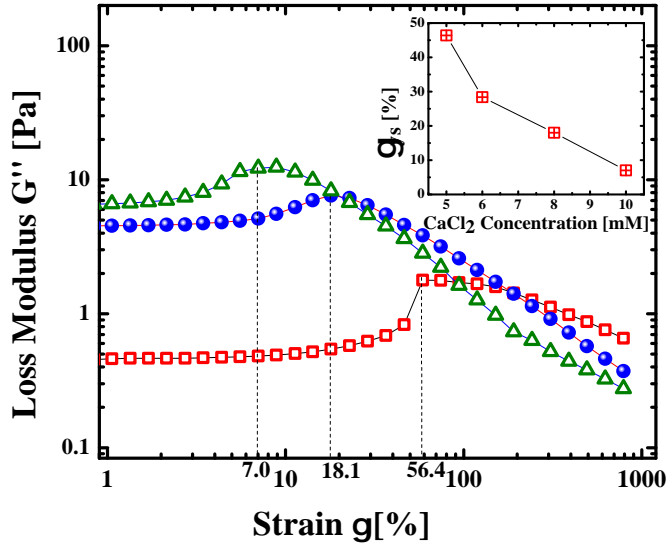


FIGURE 5.11: Plots of the loss modulus G'' vs. strain amplitude γ for 2.5 g/L pectin solutions with CaCl_2 concentrations of 5mM (red squares), 8mM (blue circles) and 10mM (green triangles). The yield strains (γ_{ys}), which are the strains corresponding to peaks in G'' , are shown by vertical dotted lines. In the inset, a plot of yield strain γ_{ys} for 2.5 g/L pectin solutions is shown vs. CaCl_2 concentration.

peak at a certain strain γ_{ys} . γ_{ys} is a measure of the yield strain, above which G' and G'' both show approximately power-law decreases.

The limit of linear rheological response (or the limit of linearity), γ_0 , which marks the start of non-linearity in the response of the gel network to applied shear strains, is defined as the strain amplitude above which the elastic modulus G' decreases more than 5% from its maximum value of G'_0 in amplitude sweep measurements (Fig. 5.10(b)). If G'_0 is plotted vs. increasing CaCl_2 concentration C , a power law increase ($G'_0 \sim C^k$) is observed in G'_0 (squares in Fig. 5.12). In the proposed egg-box model of pectin chain junctions [33], Ca^{2+} ions form cross-linking bridges between two adjacent non-methylated galacturonic units of two pectin chains. The number of cross-links, N_c , increases with increase in CaCl_2 concentration for a constant pectin concentration due to the increased availability of Ca^{2+} ions. Following the argument of Lootens *et al.* [15], if the elastic modulus G' depends only on the system entropy, $G' \propto \nu$, where

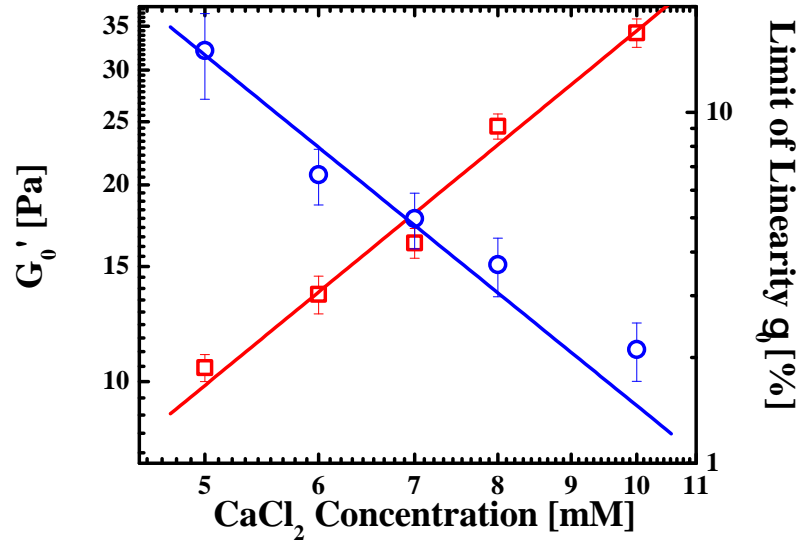


FIGURE 5.12: Plots of the linear elastic modulus G'_0 (□) and the limit of linearity γ_0 (○) vs. CaCl_2 concentration for 2.5 g/L pectin solutions with added salt. The corresponding power law fits ($G'_0 \sim C^K$ and $\gamma_0 \sim C^{-L}$ with $K=1.78$ and $L=2.90$) to the data are shown by solid lines.

ν is the molar concentration of the elastically active network chains (EANC). For pectin gels with added calcium ions, $\nu = 2N_c - C_p/M_n$ [15, 34, 35], where C_p and M_n are, respectively, the concentration and the number average molar masses of the pectin chains. Increasing the CaCl_2 concentration, keeping the pectin concentration fixed, increases the value of ν due to an increase in N_c . This results in the observed increase of the elastic modulus G' of pectin gels with increasing CaCl_2 concentration. It is observed in Fig. 5.12 that while G'_0 increases with added CaCl_2 concentrations, the non-linearity in G' starts to appear at lower strains in samples with higher added CaCl_2 concentrations (circles in Fig. 5.12). This is also shown by vertical dotted lines in Fig. 5.10(b).

The decrease in γ_0 with CaCl_2 concentration can be fitted to a power law of the form $\gamma_0 \sim C^{-L}$. The start of a non-linear elastic response in a cross-linked gel indicates the onset of plastic rearrangements in the network. As a lower critical stress is also observed with higher added CaCl_2 concentration (Fig.

5. FORMATION AND RUPTURE OF Ca^{2+} INDUCED PECTIN BIOPOLYMER GELS

5.10(a)), it is concluded that the onset of non-linear behavior and the subsequent rupture of the gel network are accelerated significantly by an increase in CaCl_2 concentration. The yield strains, γ_{ys} , extracted from the peak positions of the plots of G'' , are also observed to decrease with the added CaCl_2 concentration C . This data is plotted in the inset of Fig. 5.11.

The simultaneous lowering of σ_{critical} and γ_o for highly elastic pectin gels gives important information about the nature of the links that form between the pectin flocs. To explain the simultaneous power-law decrease of the limit of linearity and the power law increase in G'_0 of elastic pectin gels with increasing salt concentration, a scaling approach proposed by Shih *et al.* for fractal colloidal gel in the strong link regime [25] is followed here. It must be noted here that fractal concepts have previously been employed to analyze rheological data for biopolymer pectin gels [36], protein gel networks [31, 37] and colloidal gels [25, 38]. In lysozyme protein gels, for example, the inverse strain-dependence of the upper limit of the linear viscoelastic region is attributed to the strong link behavior of protein gels [39]. In all these previous studies, gelation was induced by changing the volume fractions of the gel-forming macromolecules. In this work, in contrast, gelation is triggered not by an increase in the volume fraction of pectin, but by an increased availability of Ca^{2+} ions which enhances the formation of crosslinking bridges between pectin chains.

It is observed in Fig. 5.4 that the mean relaxation time $\langle \tau_R \rangle$ increases with increase in CaCl_2 concentration. This arises due to an increase in floc sizes before gelation. The increase in floc sizes with increasing salt concentration is also verified from cryo-SEM images (Fig. 5.5). For a reaction-limited fractal structure, simulation studies show that the radius of a cluster or floc, ξ , increases with cluster mass S according to a power law [40]. As the number of pectin chains increases inside a floc due to the increased formation of ion-induced crosslinks, it is reasonable to assume that the cluster mass S increases with salt concentration C . The floc size ξ can therefore be expected to

show the following power-law relation with CaCl_2 concentration

$$\xi \sim C^M \quad (5.5)$$

where C is the concentration of CaCl_2 and M is a power law exponent. As floc sizes grow due to an increase in CaCl_2 concentration, the flocs start to behave like weak springs [41], with the links within a floc becoming weaker due to a growth in floc sizes. For the pectin gels studied here, the links between the flocs (inter-floc links) can be characterized by higher elastic constants compared to the links within the individual flocs (intra-floc links). In this regime, when the applied stress is above a critical value, the links within the individual flocs can be assumed to break more easily than those between flocs. This is called the ‘strong-link’ regime [25]. If K_ξ is the individual elastic constant of a floc of size ξ , then the macroscopic elastic constant G'_0 for a system of size L can be written as $G'_0 \sim [\frac{L}{\xi}]^{d-2} K_\xi$, where d is the dimension of the system [25]. For a 3-dimensional system, G'_0 can be written as:

$$G'_0 \sim (K_\xi/\xi) \quad (5.6)$$

The macroscopic elastic constant G'_0 therefore increases with the increase in individual floc elasticities but decreases with the increase in floc sizes. For a macroscopic deformation ΔL , the deformation of an individual floc is $(\Delta L)_\xi = (\frac{\Delta L}{L})\xi$. The force on a floc is therefore $F_\xi = K_\xi(\Delta L)_\xi = K_\xi(\frac{\Delta L}{L})\xi$. In the ‘strong-link’ regime, the intra-floc links will break when the force on a floc is above a critical constant value. The limit of linearity γ_0 in this regime can be written as [25]

$$\gamma_0 = \frac{\Delta L}{L} \sim (K_\xi \xi)^{-1} \quad (5.7)$$

From Fig. 5.12, it is observed that $G'_0 \sim C^K$ and $\gamma_0 \sim C^{-L}$. These power law

5. FORMATION AND RUPTURE OF Ca^{2+} INDUCED PECTIN BIOPOLYMER GELS

relations are used along with Eqns. 5.6 and 5.7 to conclude that the individual floc elasticity K_ξ also follows a power law with CaCl_2 concentration:

$$K_\xi \sim C^N \quad (5.8)$$

Here, $\frac{K+L}{2} = N$. Increase in the individual floc elasticity K_ξ with C is clearly due to an increase in cross-linking density within a floc. As $\xi \sim C^M$ and $K_\xi \sim C^N$, Eqns. 5.6 and 5.7 can be written as $G'_0 \sim C^{N-M}$ and $\gamma_0 \sim C^{-(N+M)}$. From the experimental data of Fig. 5.12 for 2.5 g/L pectin solutions with added salt, $N-M = 1.78$ and $N+M = 2.90$, which implies $M = 0.56$ and $N = 2.34$. This indicates that in a probable scenario wherein both ξ and K_ξ exhibit power-law variations with CaCl_2 concentration, $\xi \sim C^{0.56}$ and $K_\xi \sim C^{2.34}$ for Ca^{2+} induced 2.5 g/L pectin gel. The floc size ξ is therefore weakly dependent on C . The individual floc elasticity K_ξ , in contrast, shows a much stronger dependence on C . These results are in agreement with the cryo-SEM images of 5.5(c) and 5.5(d), where the individual floc sizes do not appear to change significantly with C when $C > C_{\text{cr}}$, while the density of crosslinks clearly increases. A stronger dependence of the elastic modulus on individual floc elasticity, rather than the floc size, was also observed in the reaction limited aggregation regime of globular protein gels [31].

Finally, all the experiments reported earlier are repeated for aqueous pectin solutions of a higher concentration (5 g/L) to investigate the dependence of the power law exponents on pectin concentration. In Fig. 5.13, the elastic modulus G' is plotted vs. γ for 5 g/L pectin solutions containing different amounts of CaCl_2 . This plot is used to extract the macroscopic elastic constant G'_0 and the limit of linearity γ_0 for 5 g/L pectin solutions containing different amounts of CaCl_2 . When the extracted values of G'_0 and γ_0 are plotted, power-law behaviors of both the macroscopic elastic constant G'_0 and the limit of linearity γ_0 are observed with increasing salt concentration. This data

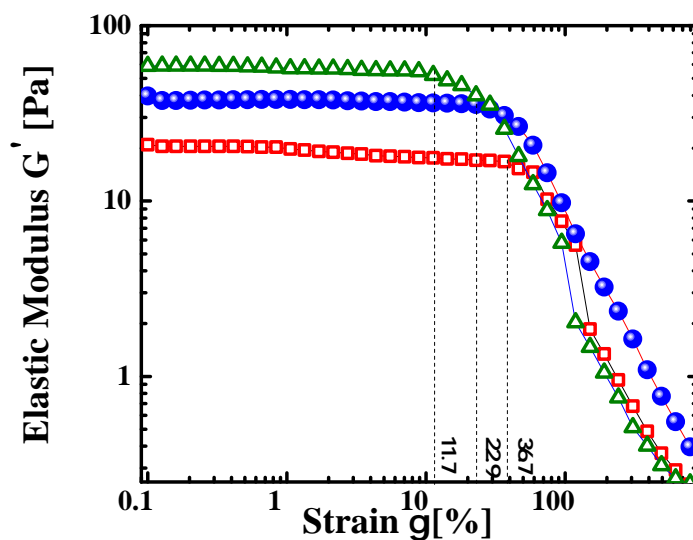


FIGURE 5.13: Plots of G' vs. strain amplitude γ for 5 g/L pectin solutions with different CaCl_2 concentrations: 6mM (red squares), 8mM (blue circles) and 10mM (green triangles). The start of non-linearity is shown by vertical dotted lines.

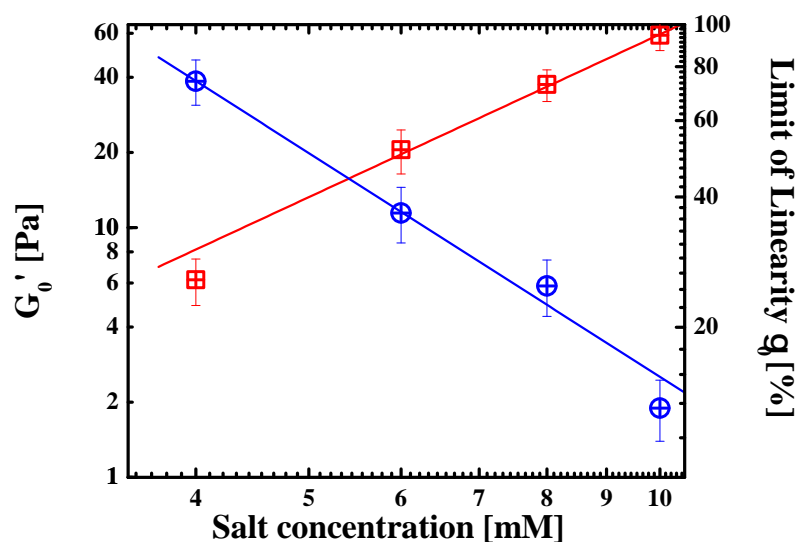


FIGURE 5.14: Plots of G'_0 (\square) and γ_0 (\circ) vs. CaCl_2 concentration for 5 g/L pectin solutions with added salt. The corresponding power law fits ($G'_0 \sim C^K$ and $\gamma_0 \sim C^{-L}$ with $K=1.81$ and $L=3.23$) to the data are shown by solid lines.

5. FORMATION AND RUPTURE OF Ca^{2+} INDUCED PECTIN BIOPOLYMER GELS

is shown in Fig. 5.14. For 5 g/L pectin gels, ξ and K_ξ are described by the following relations: $\xi \sim C^{0.71}$ and $K_\xi \sim C^{2.52}$. Interestingly, even for this higher pectin concentration, it is observed that while ξ is only weakly dependent on C , K_ξ shows a much stronger dependence, corroborating our earlier observation that individual floc elasticities have a strong dependence on salt concentration.

For the 2.5 g/L pectin sample with 5 mM salt (squares in Fig. 5.10(b)), $G'_o \approx 7$ Pa. Increasing both pectin and salt concentration by a factor of 2 (data for the 5 g/L pectin sample containing 10 mM salt, plotted in Fig. 5.13, is denoted by triangles) increases the value of G'_o to approximately 60 Pa. As the dependences of ξ and K_ξ on C do not change significantly with pectin concentration, the large increase in G'_o can be explained by considering a simultaneous increase in the number of pectin flocs and in the density of inter-floc links when the pectin concentration is increased.

5.4 Conclusions

Pectin is an important ingredient of plant cell walls, where ion-mediated pectin gels are known to contribute to the cell wall rigidity. Pectin is also often used in gel form in the areas of food science and pharmaceuticals. These factors make a study of the mechanical properties of pectin gels extremely important. In this work, the gelation of pectin with increasing CaCl_2 concentrations and the rupture of the gel networks due to the imposition of shear stresses are studied systematically. Dynamic light scattering experiments are performed to study the formation of ion-induced pectin gel networks at different CaCl_2 concentrations. It is seen that the relaxation dynamics of the system shows a gradual slowdown with increase in CaCl_2 concentration due to the formation of larger pectin flocs. This increase is accompanied by an increase in complex viscosity, with the samples eventually entering a non-ergodic state that is characterized

by incomplete decays of the measured autocorrelation functions. The polydispersity of the flocs and the system inhomogeneity are seen to increase with CaCl_2 concentration before the onset of gelation. Cryo-SEM images are used to verify these results qualitatively, while SLS studies confirm that the formation of pectin gels is governed by a 3-D reaction-limited aggregation process. Next, systematic rheological studies are performed to understand the rupture of pectin gels. It is seen that when a constant stress is applied to pectin gels, the gel structures weaken due to the development of permanent strains and eventually break when the applied stress is above a critical value that decreases with salt (CaCl_2) concentration. Furthermore, the rheological studies reveal that increasing CaCl_2 concentration increases the elasticity of the gel, but decreases the limit of linearity of the strain response of the samples. This feature, together with the observation that the elastic moduli of the gels show a power-law increase with salt concentration, is used to establish that pectin gels can be categorized to lie in a 'strong link' regime in which inter-floc links are much stronger than intra-floc links. The existence of the strong link regime in pectin gels supports our observations that smaller critical stresses are required to break gel networks formed with larger CaCl_2 concentrations. In contrast to earlier reports where gelation was induced by increasing the volume fraction of the gel-forming molecule, our work investigates the process of ion-mediated gelation keeping the pectin concentration fixed.

References

- [1] J. Pelloux, C. Rusterucci and E. J. Mellerowicz, *TRENDS in Plant Science*, **12**, 267 (2007).
- [2] R. G. W. Jones and O.R. Lunt, *Bot. Rev.*, **33**, 407 (1967).
- [3] P. K. Helper, *The Plant Cell*, **17**, 2142 (2005).
- [4] C. D. May, *Carbohydrate Polymers*, **12**, 79 (1990).
- [5] P. Sriamornsak, *Chemistry of Pectin and Its Pharmaceutical Uses : A Review*; *Silpakorn University International Journal*, 206 (2003).
- [6] S. R. Bhatia, S. F. Khattak, Su. C. Roberts, *Current Opinion in Colloid & Interface Sc.*, **10**, 45 (2005).
- [7] M. E. McEntee, S. K. Bhatia, L. Tao, S. C. Roberts and S. R. Bhatia, *J. Applied Polymer Sc.*, **107**, 2956 (2008).
- [8] A. Banerjee, M. Arha, S. Choudhary, R. S. Ashton, S. R. Bhatia, D. V. Schaffer and R. S. Kane, *Biomaterials*, **30**, 4695 (2009).
- [9] J. C. White, E. M. Saffer and S. R. Bhatia, *Biomacromol.*, **14**, 4456 (2013).

-
- [10] C. Garnier, M.A.V. Axelos, J.-F. Thibault, *Carbohydrate Research*, **256**, 71 (1994).
- [11] S. Yoo, M. L. Fishman, A. T. Hotchkiss Jr. and H. G. Lee, *Food Hydrocolloids*, **20**, 62 (2006).
- [12] D. Durand, C. Bertrand, A.H. Clark and A. Lips, *Int. J. Biol. Macromol.*, **12**, 14 (1990).
- [13] A.H. Clark and S.B. Ross-Murphy, *Adv. Polym. Sci.*, **83**, 192 (1987).
- [14] M.A.V. Axelos and M. Kolb, *Phys. Rev. Letter*, **64**, 1457 (1990).
- [15] D. Lootens, F. Capel, D. Durand, T. Nicolai, P. Boulenger and V. Langendorff, *Food Hydrocolloids*, **17**, 237 (2003).
- [16] S. M. Cardosa, M. A. Coimbra and J.A Lopes da Silva, *Food Hydrocolloids*, **17**, 801 (2003).
- [17] I. Fraeye, E. Doungra, T. Duvetter, P. Moldenaers, A. V. Loey and M. Hendrickx, *Food Hydrocolloids*, **23**, 2069 (2009).
- [18] J. Narayanan, V. W. Deotare, R. Bandyopadhyay and A. K. Sood, *J. Coll. and Interface Sc.*, **245**, 267 (2002).
- [19] A. Kjoniksen, M. Hiorth, B. Nystrom, *European Polymer Journal*, **40(11)**, 2427 (2004).
- [20] M. Dobies, S. Kusmia and S. Jurga, *Acta Physica Polonica A*, **108**, 33 (2005).
- [21] E. R. Morris, D. A. Powell, M. J. Gidley and D. A. Rees, *J. Molecular Biology*, **155**, 507 (1982).
- [22] D. Thom, G. T. Grant, E. R. Morris and D. A. Rees, *Carbohydrate Research*, **100**, 29 (1982).

-
- [23] C. Garnier, , M. A. V. Axelos, J.-F. Thibault, Carbohydrate Research, **240**, 219 (1993).
- [24] V. Javvaji, A. G. Baradwaj, G. F. Payne and S. R. Raghavan, Langmuir, **27**, 12591 (2011).
- [25] W. H. Shih, W. Y. Shih, S. I. Kim, J. Lin and I. A. Aksay, Phys. Rev. A, **42**, 4772 (1990).
- [26] C. P. Lindsey and G. D. Patterson, J. Chem. Phys., **73**, 3348 (1980).
- [27] W. van Megen and P. N. Pusey, Phys. rev. A, **43**, 5429 (1991).
- [28] C. W. Macosko, Rheology: Principles, Measurements and Application, (Wiley-VCH, New York, 1994).
- [29] M. Y. Lin, H. M. Lindsay, D. A. Weitz, R. C. Ball, R. Klein and P. Meakin, Proc. R. Soc. Lond. A, **423**, 71 (1989).
- [30] R. C. Ball, D. A. Weitz, T. A. Witten and F. Leyvraz, Phy. Rev. Lett., **58**, 274 (1987).
- [31] S. Ikeda, E. A. Foegeding and T. Hagiwara, Langmuir, **15**, 8584 (1999).
- [32] J. R. Stokes and W. J. Frith, Soft Matter, **4**, 1133 (2008).
- [33] I. Braccini and S. Perez, Biomacromol., **2**, 1089 (2001).
- [34] A. H. Clark, K. T. Evans and D. B. Farrer, Int. J. Biological Macromol., **15**, 125 (1994).
- [35] A. H. Clark and D. B. Farrer, Food Hydrocolloids, **10**, 31 (1996).
- [36] D. Bonn, H. Kellay, M. Prochnow, K. Ben-Djemaa and J. Meunier, Science, **280**, 265 (1998).
- [37] M. Verheul, S. P. F. M. Roefs, J. Mellema and K. G. de Kruif, Langmuir, **14**, 2263 (1998).

- [38] H. Wu and M. Morbidelli, *Langmuir*, **17**, 1030 (2001).
- [39] M. A. da Silva and E. P.G. Areas, *J. Coll. and Interface Sc.*, **289**, 394 (2005).
- [40] P. Meakin, and F. Family, *Phy. Rev. A*, **36**, 5498 (1987).
- [41] Y. Kantor and I. Webbman, *Phy. Rev. Lett.*, **52**, 1891 (1984).

6

Chaotic Rheological Response in the Shear Banding Region of Cornstarch Suspensions

6.1 Introduction

The mesoscopic structures of different soft matter systems can be affected by shear flow. Above a critical applied shear rate or shear stress, shear flow may become unstable due to the nonmonotonic dependence of shear stress σ on shear rate $\dot{\gamma}$. Due to the coupling between structure and flow, many complex fluids may separate into bands of widely different viscosities under these rheological conditions. This phenomenon, where macroscopic bands with different shear rates or shear stresses coexist in the sample, is known as shear banding [1–3]. The shear banding effect is observed in wormlike micellar systems [4–6], lamellar systems [7], polymer solutions [8], liquid crystal systems [9, 10] and

many other soft matter systems. Along with rheological measurements, the existence of inhomogeneous structures in shear-banded flows is investigated using birefringence studies [5, 11–13], turbidity and light scattering measurements [14, 15], small angle x-ray scattering (SAXS) measurements [9, 16], small angle neutron scattering (SANS) measurements [6, 11, 17], nuclear magnetic resonance (NMR) measurements [18], heterodyne dynamic light scattering measurements (DLS) [19, 20] and particle imaging velocimetry [21].

The presence of shear banding is usually associated with complex rheological features. One such feature is the occurrence of chaotic rheological responses in the shear banding regime, which is known as “rheochaos” [22–26]. The phenomenon of rheochaos is generally attributed to the presence of spatial and temporal inhomogeneities in the shear banding system. Fielding *et al.* describe a theoretical model for systems showing shear bands. Their model shows that a coupling between flow and microstructure in the shear banding region can result in possible chaotic dynamics [27]. Complex dynamics characterizing rheochaos in the shear banding region are observed in wormlike micellar solutions [22–24], lamellar phases in surfactant solutions [19], polymer solutions [8] *etc.*

Recently non-Newtonian flow behaviors of concentrated cornstarch suspensions, which show both shear thinning and shear thickening, have attracted huge interest. Fall *et al.* have performed rheological measurements along with MRI imaging of cornstarch suspensions to understand the mechanism of shear thickening in the system [28, 29]. They identify the shear thickening phenomenon as a re-entrant jamming transition. They describe the mechanism of shear thickening as a dilation effect in a confined geometry. It is believed that dilation in a confined volume results in the formation of shear induced hydroclusters, which cannot flow due to space constraints. The resultant jamming transition therefore gives rise to the observed shear thickening behavior. The theoretical work of Cates *et al.* [30] on dilatancy and jamming discusses

the discontinuous shear thickening phenomenon in colloidal suspension by invoking two parameters: ‘glassiness’ and ‘jammability’. According to these authors, such samples ultimately show yielding behavior at sufficiently high shear stresses. One can expect that the shear thickening behavior of cornstarch suspensions, described by Fall *et al.*, should be followed by a yielding response.

In this work, we study the rheological responses of cornstarch suspensions at high shear rates in a regime that follows the previously observed shear thickening region. Using rheo-optical techniques, we observe that the suspension, which initially shows a regime that can be identified as shear banding, ultimately shows an yielding behavior. The extent of the shear banding regime of cornstarch suspensions is found to depend on cornstarch concentrations and sample volumes. The shear banding region is accompanied by the presence of fluctuations in the stress response to applied shear rates, which can be related to rheochaos.

6.2 Sample Preparation

To prepare a cornstarch suspension, an appropriate amount of cesium chloride (CsCl) is added to double distilled Millipore water to prepare a 55 wt% CsCl solution. CsCl has a molecular weight of 111 g/mol. The density of the prepared CsCl solution matches with that of cornstarch, which makes the cornstarch suspensions stable. Appropriate amounts of cornstarch are added slowly to the CsCl solution and the samples are ultrasonicated at room temperature. Both CsCl and cornstarch powder are purchased from Sigma Aldrich and used as received. For all the experiments, the temperature is kept constant at 25°C.

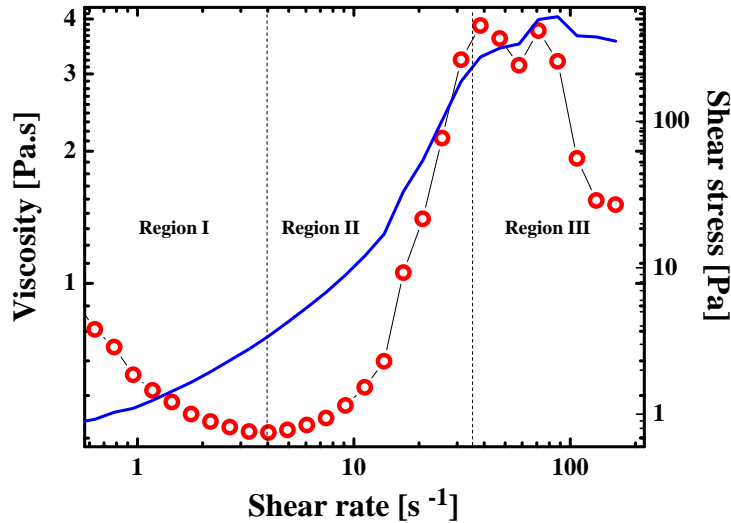


FIGURE 6.1: Plot of viscosity (\circ) and shear stress (solid line) vs. shear rate for a 40% w/w cornstarch suspension in a parallel plate geometry with 1 mm plate gap at $T = 25^{\circ}\text{C}$. The plot shows three different shear regions: (a) region I (shear thinning), (b) region II (shear thickening) and (c) region III (shear banding followed by yielding).

6.3 Results and Discussions

Fig. 6.1 shows the typical flow behavior of a highly concentrated cornstarch suspension. Cornstarch suspensions show three different regions of contrasting flow behaviors depending upon the magnitude of the applied shear rate. At low shear rates, cornstarch suspensions show a shear thinning region (region I), where the viscosity decreases with applied shear rate. This region is followed by one in which the viscosity increases abruptly (region II). It must be noted that discontinuous shear thickening transitions (such as in region II) have been observed in previous studies [28, 29]. A confined system under shear, which has a tendency to dilate, may undergo a jamming transition in a process that may be identified as shear thickening. If the applied shear rate is further increased (above 35 s^{-1}) (region III), an unstable region in the viscosity plot and a nearly plateau region in shear stress plot are observed, which is ultimately followed by an yielding region, characterized by a sudden decrease

in viscosity.

To confirm the nature of the plateau region in the flow curve, small angle light scattering (SALS) measurements are performed simultaneously with rheological measurements. We acquire 300 images for each shear rate and calculate the intensity variance ΔI using the following formula:

$$\Delta I = (1 - (\langle I(n) \rangle / I(n)))^2 \quad (6.1)$$

where $I(n)$ is the intensity of n th image and $\langle I(n) \rangle$ is the average intensity over all 300 images at a fixed shear rate. The plot of intensity variance (circles) in different rheological regimes of the flow curve is shown in Fig 6.2. Intensity variance (circles) is found to increase by more than a decade in the plateau region of the flow curve of region III, when compared to that in the shear thinning and thickening regions (regions I and II). Previous MRI measurements

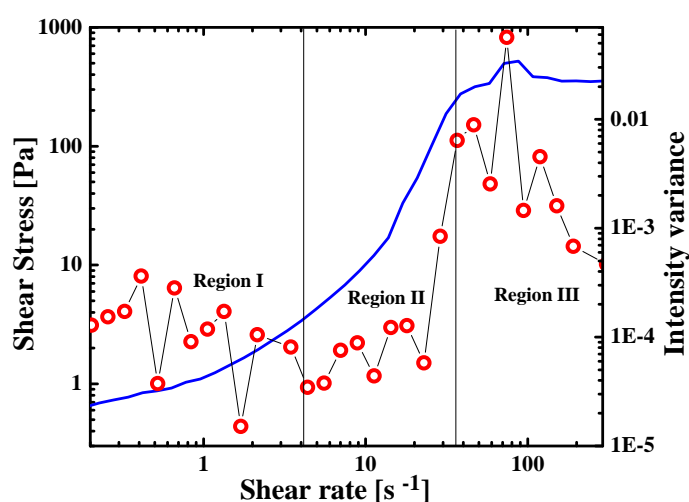


FIGURE 6.2: Plot of shear stress (solid line) and intensity variance (\circ) vs. shear rate for a 40% w/w cornstarch suspension in a parallel plate geometry with 1 mm plate gap.

show that the sample is homogeneous in the shear thinning and shear thickening regions [28]. In agreement with the previous studies, we see here that the intensity does not vary appreciably in these two regions during flow. This results in the very low observed values of intensity variances in Fig. 6.2 in the shear thinning and thickening regions. In region III, due to the coexistence of bands of different viscosities, the samples are heterogeneous. Therefore, images from different viscosity regions are captured during flow in the SALS measurements. The high viscosity regime results in dark images, while the low viscosity region results in bright images. The intensities of the images therefore fluctuate largely due to the existence of bands, resulting in the higher values of intensity variance observed here. The high intensity variations reported in Fig. 6.2 therefore confirms the presence of inhomogeneous banded structures in the sample. The plateau region of region III can therefore be identified as a shear banding region. This region is followed by the yielding region, where the intensity variance decreases significantly as the system settles down to a relatively uniform state at very high shear rates. We note here that the plateau region in the flow curve has previously been associated with the shear banding region [5, 17, 31].

Due to dilation in the shear thickening region, cornstarch particles aggregate to form hydroclusters [29]. The sizes of the hydroclusters increase with shear and can span the sample. The close contacts between the clusters can result in a jamming transition and the observed shear thickening behavior [29, 32]. With increasing shear rate, these hydroclusters fracture to form granules with typical sizes in the range of ten to hundreds of microns. The presence of granules makes the sample inhomogeneous, resulting in distinct mesoscopic bands of different viscosities in the shear banding regime. Eventually, higher shear stresses transform the granules to flowable droplets [30] resulting in the yielding transition.

The contrasting rheological regimes described above are highly dependent

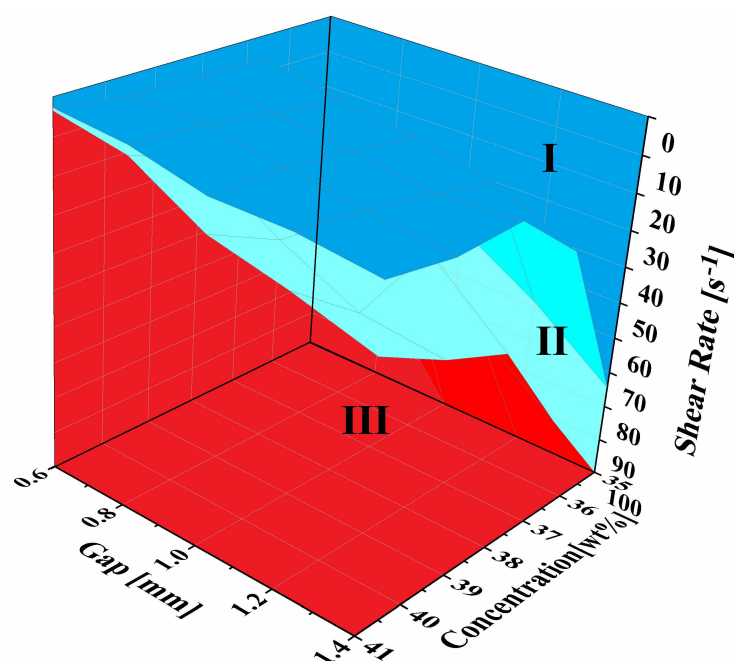


FIGURE 6.3: 3D phase diagram of cornstarch suspensions in shear rate - cornstarch concentration - gap size planes consisting shear thinning (I), shear thickening (II) and shear banding followed by yielding (III) regions. The samples are sheared in parallel plate geometry.

on the concentration of the cornstarch suspensions and the sample volumes. From the shear rate vs. viscosity plots for cornstarch suspensions of different concentrations and for different gap sizes in parallel plate geometry, the critical shear rates above which shear thickening and shear banding occur are calculated for all samples. These critical shear rate values are used to construct a 3D phase diagram in the shear rate - cornstarch concentration - gap size planes. This phase diagram is shown in Fig. 6.3, where extents of different shear regimes (shear thinning (region I), shear thickening (region II) and shear banding followed by yielding (region III)) are indicated. Shear thickening and shear banding are observed at lower shear rates for higher concentrations. When the plate gap is decreased, the shear thickening phenomenon becomes more abrupt at lower shear rates, thereby extending the regime of shear banding. The decrease of critical shear rate for shear thickening with decrease in plate gap has been observed before [28, 29]. When cornstarch concentration

6. CHAOTIC RHEOLOGICAL RESPONSE IN THE SHEAR BANDING REGION OF CORNSTARCH SUSPENSIONS

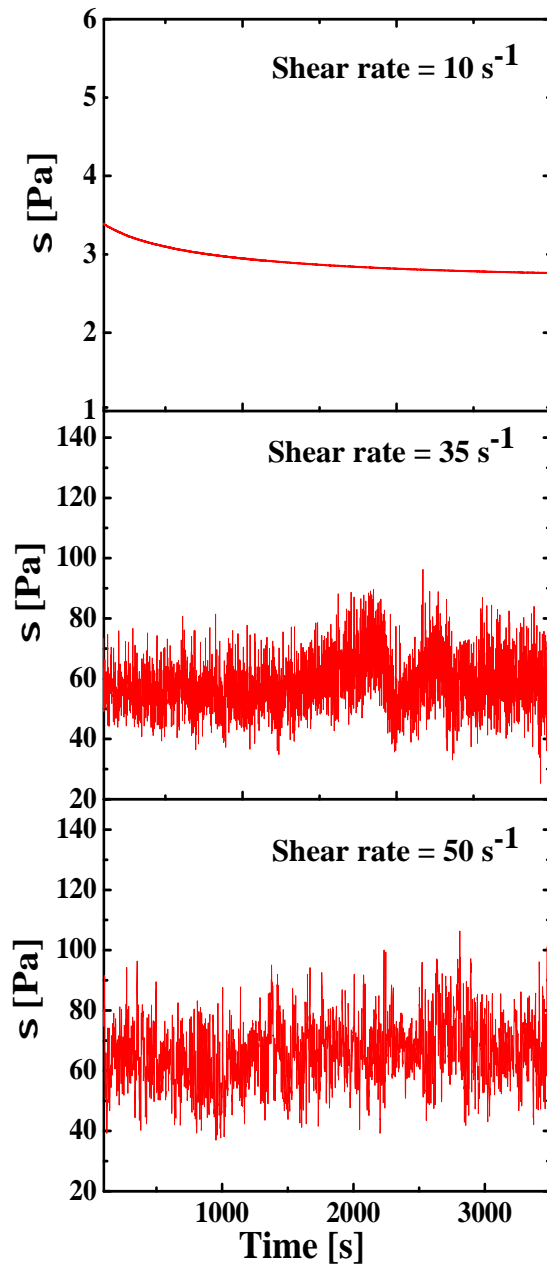


FIGURE 6.4: Plot of stress fluctuation data for a 40% w/w cornstarch suspension sheared in a parallel plate geometry with 1 mm plate gap at different shear rates: (a) 10 s^{-1} , (b) 35 s^{-1} and (b) 50 s^{-1} . The data becomes increasingly time dependent with increase in shear rate.

is decreased and the gap size is increased, the critical shear rate for shear banding regime increases to higher shear rates, sometimes beyond our experimental limit. Higher concentrations of cornstarch suspensions and increased confinement of the sample causes the hydroclusters to fracture into granules and flowable droplets at lower shear rates. This results in extended regions of shear banding and yielding in the phase diagram under these conditions.

To understand the nature of the shear banding regime, stress relaxation measurements are performed by imposing step shear rates of different magnitudes to the samples. The data is shown in Fig. 6.4. For low shear rates, $\dot{\gamma} = 10 \text{ s}^{-1}$, corresponding to the onset of the shear thickening regime (region II) in Fig. 6.1, the stress relaxes monotonically to a steady state value. For higher shear rates $\dot{\gamma} = 35 \text{ s}^{-1}$ and 50 s^{-1} lying in the shear banding regime (region III), the stress does not relax to a steady state and, instead, shows huge fluctuations throughout the duration of observation.

Following previous studies on a variety of other samples [22], we analyze the stress fluctuation data for the sample lying in region III to estimate whether the observed fluctuations are deterministic in nature or are stochastic noise. One of the methods to establish the presence of chaos is the calculation of a correlation dimension ν , a dynamical invariant that quantifies the fractal dimension of the attractor. The attractor is a low dimensional subset of the phase space of a dynamical system to which the initial phase space converges asymptotically with the advancement of time. The time series of the acquired stress fluctuation data can be written as $\sigma_i = \sigma(i\Delta t)$ with $i = 1$ to 8000 spaced at a regular interval $\Delta t = 1 \text{ s}$. From the time series data, we construct an m dimensional vector $X_j = (\sigma_j, \sigma_{j+L}, \sigma_{j+2L}, \dots, \sigma_{j+(m-1)L})$ with $j = 1$ to $N-(m-1)L$, where m is the embedding dimension and L is the delay time [33]. The vector X_j defines a trajectory in an m dimensional phase space in such a way that the original time series can be described by the following dynamics $F: X_j \rightarrow X_{j+1}$. The delay time L is calculated from the time at which the correlation function of

6. CHAOTIC RHEOLOGICAL RESPONSE IN THE SHEAR BANDING REGION OF CORNSTARCH SUSPENSIONS

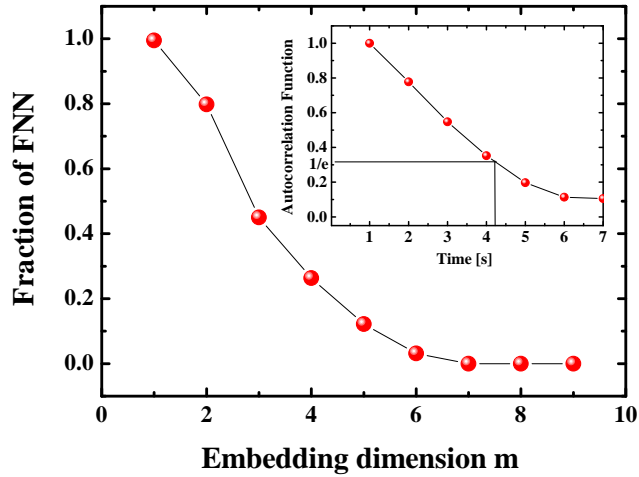


FIGURE 6.5: A plot of the fraction of false nearest neighbors (FNN) vs. embedding dimension m for the stress fluctuation data of a 40% w/w cornstarch suspension sheared in a parallel plate geometry with 1 mm plate gap at a shear rate 50 s^{-1} , where the sample lies in shear banding regime (region III). The fraction of FNN falls to zero at $m=8$. In the inset, the plot of correlation function vs time is shown. The correlation function decays to $1/e$ of its initial value at approximately 5 s, giving delay time $L=5$ s.

the time series decays to $1/e$ of its initial value (inset of Fig. 6.5). According to the algorithm of Kennel *et al.*, the embedding dimension m can be calculated by estimating the number of false nearest neighbors in the neighborhood of the data point (Fig. 6.5) [34]. False nearest neighbor points are those points that appear to be the nearest neighbors of the data point because the embedding dimension is too small to unfold the attractor [34]. At an optimum embedding dimension m_0 , the fraction of the false nearest neighbors decreases approximately to 0. From Fig. 6.5, m_0 for the stress fluctuation data for a 40% w/w cornstarch suspension sheared at a constant shear rate 50 s^{-1} , where the suspension lies in the shear banding regime (region III), is estimated to be 8. Next, we calculate the correlation integral $C(R)$ for the same data as a function of distance R in an m dimensional phase space. $C(R)$ gives the number of point pairs separated by a distance less than R and is calculated using the

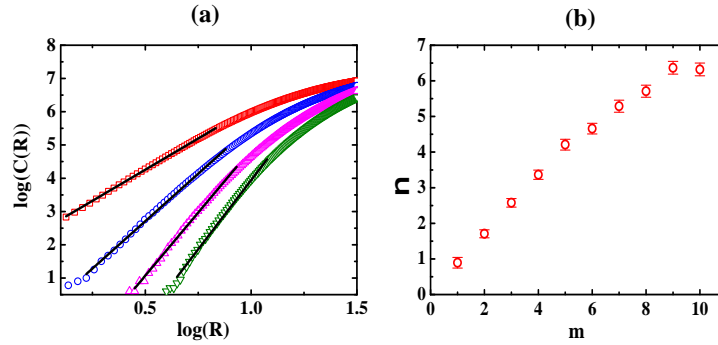


FIGURE 6.6: (a) The plots of $\log(C(R))$ vs. $\log(R)$ are shown for the stress fluctuation data of a 40% w/w cornstarch suspension lying in shear banding regime (region III), sheared in a parallel plate geometry with a 1 mm plate gap, at shear rate 50 s^{-1} for different embedding dimensions: $m=2$ (red squares), $m=4$ (blue circles), $m=6$ (pink uptriangles) and $m=8$ (green downtriangles). The black solid lines show the linear fits to the data. From the slopes of the linear fits, the correlation dimensions ν are calculated for different embedding dimensions and plotted in (b). The value of ν is found to increase with increasing m and eventually saturates at m_0 . The saturation value of ν is the correlation dimension ν_0 .

following formula:

$$C(R) = \frac{1}{N^2} \sum_{j,i+1}^N H(R - |X_j - X_i|)$$

where H is the Heaviside function and $|X_j - X_i|$ is the distance between the i th and j th points in the m dimensional phase space. For low values of R , the correlation integral $C(R) \sim R^\nu$ [33]. We have plotted $\log(C(R))$ vs. $\log(R)$ in Fig. 6.6(a) for different embedding dimensions. From the slopes of these plots at low R , the correlation dimensions ν are calculated and plotted for different embedding dimensions in Fig. 6.6(b). For a large enough embedding dimension $m (=m_0)$, ν saturates to ν_0 and is independent of m . ν_0 is the fractal dimension of the attractor. Fig. 6.6 (b) shows the plot of ν vs. embedding dimension m for the stress fluctuation data at shear rate 50 s^{-1} . It is seen that ν increases to a saturation value of approximately 6.3 for the embedding dimensions $m \geq 8$. Therefore, for a shear rate 50 s^{-1} , $\nu_0 = 6.3$ and $m_0 = 8$. If a time series is generated due to deterministic chaos rather than random noise, it follows the relation $\nu_0 \leq m_0$ [33]. For the shear rate 50 s^{-1} , the stress fluctuation

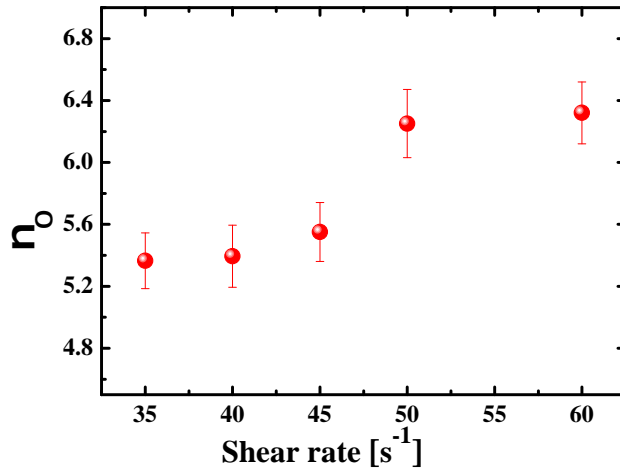


FIGURE 6.7: The plot of correlation dimension v_0 vs. imposed shear rates for the stress fluctuation data of 40% w/w cornstarch suspensions lying in shear banding regime (region III), sheared in a parallel plate geometry with 1 mm plate gap at $T=25^\circ\text{C}$.

data fulfills this criterion and the observed dynamics therefore arises due to deterministic chaos. We acquire more stress fluctuation data in region III and repeat the above analysis for all the data sets. We observe chaotic behavior in the stress response at all shear rates lying in the shear banding regime. If v_0 is plotted vs. applied shear rate for the shear banding regime (region III) of 40% w/w cornstarch suspensions, we observe a monotonic increase in v_0 . The data is plotted in Fig. 6.7. The criterion $v_0 \leq m_0$ has been verified in all cases.

One of the most important features of deterministic chaotic data is the existence of a positive Lyapunov exponent. Positive values of Lyapunov exponents suggest that the Euclidean distance between two neighboring data points diverges exponentially with time. In this work, the Lyapunov exponent is calculated using the TISEAN (Time Series Analysis) software package [35]. This software package uses the method proposed by Rosenstein *et al.* to calculate the maximum Lyapunov exponent [36]. In this calculation, the Euclidean distance $d_{ij}(K)$ between two vectors in an m dimensional space for K iterations is calculated using the formula $d_{ij}(K) = \left| \vec{X}_i - \vec{X}_j \right|$ [37]. In Fig. 6.8,

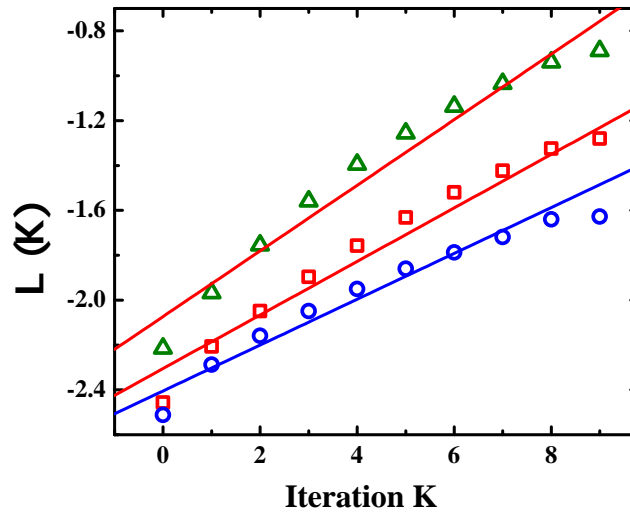


FIGURE 6.8: The plot of $L(K)$ vs. iteration K for the stress fluctuation data acquired from 40% w/w cornstarch suspensions lying in the shear banding regime (region III), sheared in parallel plate geometry with 1 mm plate gap at different applied shear rates: 35 s^{-1} (\circ), 40 s^{-1} (\square) and 50 s^{-1} (\triangle). Linear fits with slopes s to the plots are shown by solid lines.

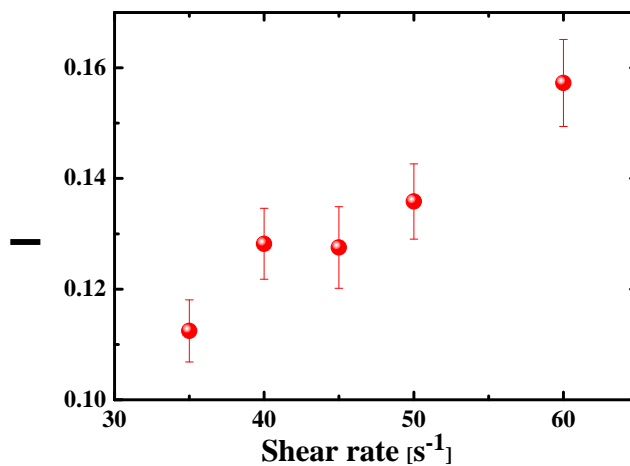


FIGURE 6.9: The plot of Lyapunov exponent λ vs. imposed shear rate for the stress fluctuation data acquired from 40% w/w cornstarch suspensions lying in the shear banding regime (region III), sheared in parallel plate geometry with 1 mm plate gap.

6. CHAOTIC RHEOLOGICAL RESPONSE IN THE SHEAR BANDING REGION OF CORNSTARCH SUSPENSIONS

$\Lambda = \langle \ln(d_{ij}(K))/d_{ij}(0) \rangle$ is plotted for stress fluctuation data acquired from 40% w/w cornstarch suspensions sheared at three different shear rates as a function of K . Linear fits to the data are performed (solid lines in Fig. 6.8), and the Lyapunov exponents λ are derived from the slopes s of these linear fits using the relation $\lambda = s/\Delta t \ln 2$. We observe positive Lyapunov exponents for all the shear rates lying within the range $35 \text{ s}^{-1} - 60 \text{ s}^{-1}$ for 40% w/w cornstarch suspensions. This confirms that the stress fluctuation data, when the suspensions are in the shear banding regime, indeed show deterministic chaos. The Lyapunov exponent values are plotted vs. applied shear rates in Fig. 6.9 for 40% w/w cornstarch suspensions. Similar to the behavior of the correlation dimension ν_0 , the Lyapunov exponent is seen to increase with increase in shear rates. This suggests an enhancement in the chaotic response at higher shear rates.

Similar analyses are repeated on the stress fluctuation data acquired from

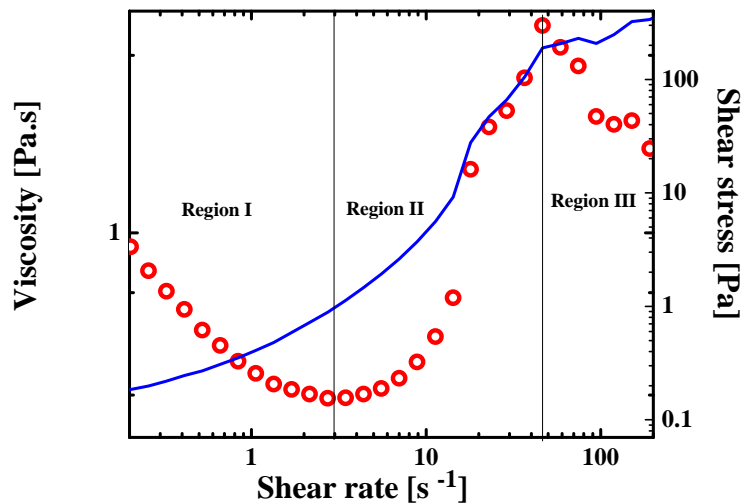


FIGURE 6.10: Plot of viscosity (\circ) and shear stress (solid line) vs. shear rate for a 39% w/w cornstarch suspension in a parallel plate geometry with 1 mm plate gap at $T = 25^\circ\text{C}$. The plot shows three different shear regions: (a) region I (shear thinning), (b) region II (shear thickening) and (c) region III (shear banding followed by yielding).

shear banding regimes of cornstarch suspensions of different concentrations,

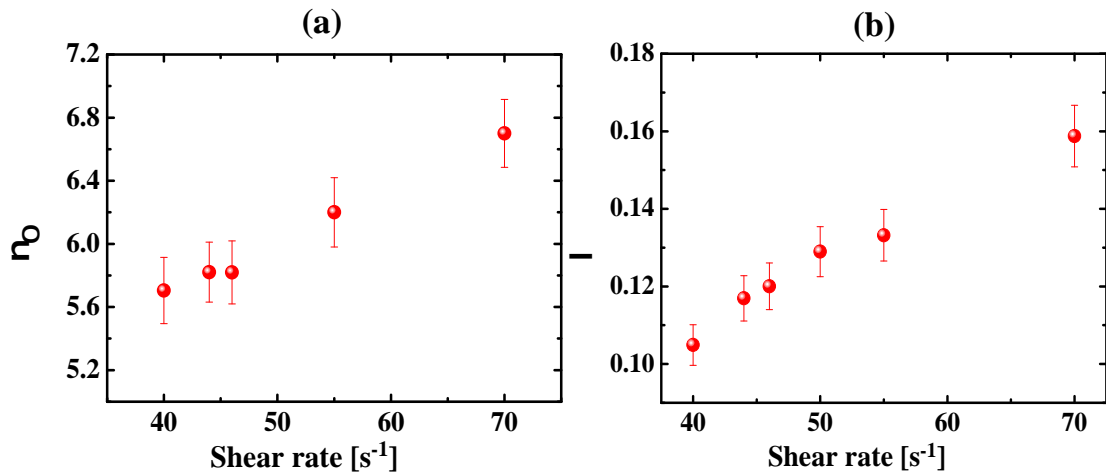


FIGURE 6.11: The plot of (a) correlation dimension v_0 and (b) Lyapunov exponent λ vs. imposed shear rate for the stress fluctuation data acquired from 39% w/w cornstarch suspensions lying in shear banding regime (region III), sheared in parallel plate geometry with 1 mm plate gap.

sheared at different gaps of parallel plate geometry. Fig 6.10 shows the plots of shear stress and viscosity vs. shear rate for a 39% w/w cornstarch suspension in a parallel plate geometry with 1 mm plate gap. This plot shows a shear banding regime (region III) at imposed shear rate $\dot{\gamma} \geq 40 \text{ s}^{-1}$. Stress relaxation data acquired after imposing shear rates lying in region III of this sample are found to be highly time dependent. This is reminiscent of the observed rheological chaos discussed earlier. Using the previously discussed methods, the values of the correlation dimensions v_0 and the Lyapunov exponents λ are extracted for the stress fluctuation data acquired from the shear banding region of the 39% w/w sample. Fig 6.11 shows the plots of correlation dimensions v_0 and Lyapunov exponents λ , extracted from the stress fluctuation data for 39% w/w cornstarch suspensions, with the variation of applied shear rate in the shear banding regime. These plots show that both correlation dimension v_0 and Lyapunov exponent λ increase with increasing shear rate, which is identical to the 40% w/w cornstarch data.

6.4 Conclusion

We use simultaneous rheological and SALS measurements to investigate the shear banding regime of cornstarch suspensions. These measurements confirm the existence of band structures in the shear banding regime. This regime is associated with a stress plateau in flow curve [5, 17, 31]. A phase diagram in shear rate - cornstarch concentration - gap size planes shows that both increasing cornstarch concentration and decreasing sample volume favor the occurrence of shear banding regime at lower shear rates. Rheological experiments show huge stress fluctuations at imposed shear rates for the sample lying the shear banding regime. Non linear time series analysis on the stress fluctuation data indicates the presence of rheological chaos, which is a common feature of the dynamics of shear banding.

As already suggested by Fall et al. [28, 29], shear thickening of the cornstarch suspensions studied here is triggered by a jamming of cornstarch particles to form large, immobile aggregates. Increasing the shear rates further leads to the break up of these aggregates, with 'aggregate-rich' areas coexisting with 'aggregate-poor' areas. This picture is consistent with the formation of shear bands [3, 27]. Stick-slip between these bands can give rise to the chaotic rheological responses observed here. As the shear rate is increased even further, the aggregates begin to flow. The homogeneity of the medium is thereby restored. This regime comprising flowable aggregates [30] is identified as yielding regime.

References

- [1] S. Manneville, *Rheol. Acta*, **47**, 301 (2008).
- [2] P. D. Olmsted, *Rheol. Acta*, **47**, 283 (2008).
- [3] S. M. Fielding, *Soft Matter*, **3**, 1262 (2007)
- [4] H. Rehage and H. Hoffmann, *Mol. Phys.*, **74**, 933 (1991).
- [5] J.-F Berret, G. Porte, and J.P. Decruppe, *Phys. Rev. E*, **55**, 1668 (1997).
- [6] V. Schmitt, F. Lequeux, A. Pousse and D. Roux, *Langmuir*, **10**, 955 (1994).
- [7] D. Bonn, J. Meunier, O. Greffier, A. Alkahwaji and H. Kellay, *Phys. Rev. E*, **58**, 2115 (1998).
- [8] L. Hilliou and D. Vlassopoulos, *Ind. Eng. Chem. Res.*, **41**, 6246 (2002).
- [9] P. Panizza, P. Archambault, and D. Roux, *J. Phys. II France*, **5**, 303 (1995).
- [10] C. Pujolle-Robic and L. Noirez, *Nature*, **409**, 167 (2001).
- [11] E. Cappelaere, J.-F Berret, J.-P. Decruppe, R. Cressely, and P. Lindner, *Phys. Rev. E*, **56**, 1869 (1997).

-
- [12] E. Cappelaere, R. Cressely, and J.-P. Decruppe, *Colloids Surfaces A*, **104**, 353 (1995).
- [13] J.-P. Decruppe, R. Cressely, R. Makhloufi, and E. Cappelaere, *Colloid Polym. Sci.*, **273**, 346 (1995).
- [14] P. Boltenhagen, Y. Hu, E. F. Matthys, and D. J. Pine, *Europhys. Lett.*, **38**, 389 (1997).
- [15] P. Boltenhagen, Y. Hu, E. F. Matthys, and D. J. Pine, *Phys. Rev. Lett.*, **79**, 2359 (1997).
- [16] L. Ramos, F. Molino, and G. Porte, *Langmuir*, **16**, 5846 (2000).
- [17] J.-F. Berret, D. C. Roux, and P. Lindner, *Eur. Phys. J. B*, **5**, 67 (1998).
- [18] P. T. Callaghan, *Rheol. Acta*, **47**, 243 (2008).
- [19] J. B. Salmon, S. Manneville and A. Colin, *Phys. Rev. E*, **68**, 051503 (2003).
- [20] J. B. Salmon, A. Colin, S. Manneville and F. Molino, *Phys. Rev. Lett.*, **90**, 228303 (2003).
- [21] Y. T. Hu and A. Lips, *J. Rheol.*, **49**, 1001 (2005).
- [22] R. Bandyopadhyay, G. Basappa and A. Sood, *Phys. Rev. Lett.*, **84**, 2022 (2000).
- [23] R. Bandyopadhyay and A. Sood, *Europhys. Lett.*, **56**, 447 (2001).
- [24] R. Ganapathy and A. Sood, *Phys. Rev. Lett.*, **96**, 108301 (2006).
- [25] Y. T. Hu, P. Boltenhagen and D. J. Pine, *J. Rheol.*, **42**, 1185 (1998).
- [26] P. Pimenta and E. E. Pashkovski, *Langmuir*, **22**, 3980 (2006).
- [27] M. Fielding and P. D. Olmsted, *Phys. Rev. Lett.*, **92**, 084502 (2004).

- [28] A. Fall, N. Huang, F. Bertrand, G. Ovarlez, and Daniel Bonn, Phys. Rev. Lett., **100**, 018301 (2008).
- [29] A. Fall, F. Bertrand, G. Ovarlez, and Daniel Bonn; J. Rheol., **56**, 575 (2012).
- [30] M. E. Cates, M. D. Haw and C. B. Holmes, J. Phys.: Condens. Matter, **17**, S2517 (2005).
- [31] H. Rehage and H. Hoffmann, Mol. Phys., **74**, 933 (1991).
- [32] N. J. Wagner and J. F. Brady, Physics Today, **62**, 27 (2009).
- [33] P. Grassberger and I. Procaccia, Phys. Rev. Lett., **50**, 346-349 (1983).
- [34] M. B. Kennel, R. Brown and H. D. I. Abarbanel, Phys. Rev. A, **45**, 3403 (1992).
- [35] The TISEAN package is written by R. Hegger, H. Kantz and T. Schreiber. (downloaded from <http://www.mpipks-dresden.mpg.de/tisean>).
- [36] M. T. Rosenstein, J. J. Collins, C. J. De Luca, Physica D, **65**, 117 (1993).
- [37] J. Gao and Z. Zheng, Phys. Rev. E, **49**, 3807 (1994).

7

Summary and Future Directions

The purpose of this chapter is to summarize the main results reported in this thesis and to briefly discuss the scope for future work. This thesis focuses on the jamming transition of micellar solutions and the applications of these micelles in dilute solutions as candidates for drug delivery. The formation and rupture of biopolymer gel networks and the non-linear rheology of concentrated cornstarch suspensions are also investigated. For these studies, rheological techniques are applied to investigate the macroscopic behaviors of the systems, while the microscopic dynamics are predominantly investigated by dynamic light scattering measurements.

In Chapter 1, we review the theoretical background required for an understanding of the work described in this thesis. This includes a discussion of intermolecular interactions in soft matter systems and the various physical properties of our systems of interest, *viz.* micelle forming triblock copolymer systems, biopolymer gels and colloidal suspensions. This discussion is followed by an introduction of the techniques of rheometry, dynamic light scattering and nonlinear time-series analysis that have been employed in this thesis work.

The detailed descriptions of the experimental methods used in this thesis are presented in Chapter 2. This chapter describes the rheological and dynamic light scattering techniques used in our studies. Other experimental techniques such as cryogenic scanning electron microscopy (Cryo-SEM) imaging, fluorescence spectroscopy and small angle X-ray scattering (SAXS), which has been used to investigate the different systems probed here, are also described here. The chapter ends with a description of some standard techniques of nonlinear dynamics that have been used to analyze rheological data presented in Chapter 6.

In Chapter 3, we report the jamming behavior of Pluronic F127 micelles and the jamming-unjamming transition of these micellar systems in the presence of the anionic surfactant SDS. Pluronic F127 is a triblock PEO-PPO-PEO copolymer which exhibits amphiphilic nature at high temperatures. Above a critical concentration and temperature, Pluronic molecules self-aggregate to form spherical micelles in aqueous solution with a hydrophobic PPO core, surrounded by a hydrophilic PEO corona. This micellization process is very sensitive to the presence of additives and temperature. At high concentrations, F127 micelles close pack to form a jammed solution that shows soft glassy rheology. The addition of an anionic surfactant to this solution results in a decrease in the elasticity and viscosity of the solution by several decades. This is due to the formation of anisotropic and size polydisperse mixed micelles that change the packing behavior and results in the unjamming of the micellar aggregates. Formation of Pluronic-SDS mixed micelles is expected to be affected by pH and the salt content of the solution. A detailed study of the effects of pH and salt concentration on the jamming-unjamming transition of Pluronic micellar solutions in the presence of the anionic surfactant SDS needs to be performed to obtain a better understanding of the packing of the micellar aggregates under different conditions.

Pluronic micelles have emerged as a potential agent for targeted drug delivery. Chapter 4 discusses the encapsulation of different drug molecules (Ibuprofen, Aspirin, Erythromycin) in Pluronic micelles and the dependence of the encapsulation process on temperature, pH and drug hydrophobicity. Our studies show that the micellization temperature decreases with the addition of drug molecules above a critical concentration C_t . This C_t value also decreases with the increase in drug hydrophobicity. The mean hydrodynamic radii and polydispersities of the micelles are found to increase with decrease in temperature and in the presence of the drug molecules. The hydration of the micellar core at lower temperatures is verified using fluorescence measurements. Experiments performed after increasing solution pH indicate the ionization of the drugs incorporated in the micellar cores. This causes rupture of the micelles and the release of the drugs into the solution. The effects of drug encapsulation on Pluronic micelles and the critical concentration C_t for different drug molecules should also depend upon the PPO/PEO ratios of Pluronic molecules. Similar experiments on drug encapsulation by micelles formed by Pluronic molecules of different PPO/PEO ratios need to be performed. Small angle neutron scattering (SANS) experiments on drug encapsulated Pluronic micellar systems will provide quantitative information about the encapsulated drug molecules in these micelles. This will provide further insight into the correlation between the quantum of encapsulated drugs in the micelles and the change in CMT of the micellar solutions under different conditions.

In Chapter 5, the formation and rupture of Ca^{2+} induced pectin biopolymer gels have been studied. It is seen that the relaxation dynamics of the system shows a gradual slowdown with increase in CaCl_2 concentration due to the formation of large pectin flocs. The polydispersity of the flocs and the system inhomogeneity are seen to increase with CaCl_2 concentration before the onset of gelation. A further increase in the concentration of CaCl_2 initiates the formation of links between the pectin flocs, which results in a percolating gel

network at CaCl_2 concentrations greater than C_{cr} . Rheological studies of gel breakage show that the critical stress required to break the gel network decreases with increase in CaCl_2 concentration. Further rheological experiments reveal that increasing CaCl_2 concentration increases the elasticity of the gel, but decreases the limit of linearity of the strain response of the samples. Using a scaling analysis, it is shown that ion-mediated pectin gels can be categorized to lie in the 'strong link' regime, where interfloc links are stronger than intrafloc links. To complement this work, the study of the dynamics of pectin gels after gelation need to be performed. For this investigation, DLS experiments performed over much longer delay times, along with diffusive wave spectroscopy (DWS) measurements, may be employed. Such DLS and DWS experiments on pectin gels may also be performed while simultaneously shearing the pectin gel in a shear cell. Such studies will help to address the issue of the correlation between the mechanical properties and microscopic dynamics of bipolymer pectin gel solutions.

Cornstarch suspensions are known for their complex mechanical response. Chapter 6 presents rheological measurements on concentrated cornstarch suspensions. The flow curve measurements on cornstarch suspensions show a shear thinning region, followed by a shear thickening and a shear banding region with increasing shear rate. The extents of the different regions of cornstarch suspensions depend upon the concentration and sample volume. Small angle light scattering experiments, which are simultaneously performed with rheology, show huge intensity fluctuations in the shear banding region. Non linear time series analysis of the stress fluctuation data acquired from sheared cornstarch samples lying in the shear banding region indicates the presence of rheological chaos. The route to rheochaos in the shear banding region of cornstarch suspensions remains to be explored. For this investigation, SALS and stress fluctuation data have to be acquired and analyzed. The power spectra of fluctuations near the critical shear rate where the thickening to banding

transition occurs have to be investigated.